



**TRANSMITTANCE, SCINTILLATION AND BER ANALYSIS IN
UNDERWATER OPTICAL WIRELESS COMMUNICATION SYSTEMS**

AYSAN KESKİN

SEPTEMBER 2020

**TRANSMITTANCE, SCINTILLATION AND BER ANALYSIS IN
UNDERWATER OPTICAL WIRELESS COMMUNICATION SYSTEMS**

**A THESIS SUBMITTED TO
THE GRADUATE SCHOOL OF NATURAL AND APPLIED
SCIENCES OF
ÇANKAYA UNIVERSITY**

**BY
AYSAN KESKİN**


**IN PARTIAL FULFILLMENT OF THE REQUIREMENTS FOR THE
DEGREE OF
DOCTOR OF PHILOSOPHY
IN
THE DEPARTMENT OF
ELECTRONIC AND COMMUNICATION ENGINEERING**

SEPTEMBER 2020

STATEMENT OF NON-PLAGIARISM PAGE

I hereby declare that all information in this document have been obtained and presented in accordance with academic rules and ethical conduct. I also declare that, as required by these rules and conduct, I have fully cited and referenced all material and results that are not original to this work.

Name, Last Name : Aysan Keskin

Signature : 

Date : 25.09.2020

ABSTRACT

TRANSMITTANCE, SCINTILLATION AND BER ANALYSIS IN UNDERWATER OPTICAL WIRELESS COMMUNICATION SYSTEMS

KESKİN, Aysan

Ph.D., Department of Electronic and Communication Engineering

Supervisor: Prof. Dr. Yahya K. BAYKAL

September 2020, 127 pages

Underwater Wireless Optical Communication (UWOC) has been more popular in recent years due to the need for high data rate transmission in underwater communication. In this thesis, UWOC system is considered to improve its performance by analyzing the effects of different beam types on the system in turbulent underwater medium. More specifically, the influences of oceanic turbulence on the link performance of UWOC such as the transmittance, beam spread, scintillation and BER are examined thoroughly for different optical sources beams. PCFT, cosine Gaussian, partially coherent cosine-Gaussian, cosine-hyperbolic Gaussian and partially coherent cosine-hyperbolic Gaussian beams are used as the source to benchmark the performance of the system. To investigate the oceanic turbulence effect on the UWOC system, the power spectrum of the ocean is assumed to be homogeneous and isotropic. Additionally, the extended Huygens Fresnel principle is employed to analyze the average transmittance. In particular, on-axis and off-axis average transmittance is examined for the PCFT, cosine-Gaussian, cosine-hyperbolic Gaussian, and their partially coherent cases as well. With the help of Carter's definition, beam spread is observed for the PCFT beam. The scintillation

calculation is also benefited from the extended Huygens Fresnel principle. Apart from these, oceanic turbulence effects on BER, which is another performance criterion, in the UWOC link was also studied. Calculations were carried out by using the MATLAB program. All the system performance phenomena are examined against the important parameters of oceanic turbulence, such as the rate of dissipation of mean square temperature, ratio of the temperature and salinity contributions to the refractive index spectrum and the rate of dissipation of kinetic energy for the unit mass of fluid. Moreover, with these analyses, the degree of coherence and off-axis parameters are also studied. With this thesis, we aim at selecting suitable beams for the underwater turbulent environment and to examine the performance of UWOC links in different aspects under various excitations.

Keywords: Underwater Wireless Optical Communication, Oceanic Turbulence, Average Transmittance, Beam Spread, Scintillation, Bit Error Rate, Partially Coherent Flat-Topped Beam, Partially Coherent Cosine-Gaussian Beam, Coherent Cosine-Gaussian Beam, Partially Coherent Cosine-Hyperbolic Gaussian Beam, Coherent Cosine-Hyperbolic Gaussian Beam.

ÖZ

SUALTI ORTAMINDA KABLOSUZ OPTİK HABERLEŞME SİSTEMLERİNDE GEÇİRGENLİK, PARILDAMA VE BİT HATA ORANI İNCELEMESİ

KESKİN, Aysan

Doktora, Elektronik ve Haberleşme Mühendisliği Anabilim Dalı

Tez Yöneticisi: Prof. Dr. Yahya K. BAYKAL

Eylül 2020, 127 sayfa

Son yıllarda, yüksek hızlı veri iletiminin gereksinimleri nedeniyle sualtı kablosuz optik haberleşme sistemleri daha popüler olmuştur. Bu tezde, farklı ışık huzmelerinin ve performans kıstas ölçütlerinin sistem üzerine etkilerini inceleyerek, sualtı türbülansında kablosuz optik haberleşme performansının geliştirilmesi ele alındı. Geçirgenlik, ışın yayılması, parıldama, bit hata oranı gibi sualtı kablosuz optik haberleşme sistem performans ölçütleri üzerine okyanus türbülansının etkisi incelendi. Sistem performansını karşılaştırmak için kısmi eş fazlı düz tepeli, kosinüs Gauss, kısmi eş fazlı kosinüs Gauss, kosinüs hiperbolik Gauss ve kısmi eş fazlı kosinüs hiperbolik Gauss ışık huzmeleri kaynak olarak kullanıldı. Okyanus türbülansının sualtı kablosuz optik haberleşme sistemine etkisini incelemek için suyun güç spektrumu homojen ve izotropik olarak kabul edildi. Ortalama geçirgenliği analiz etmek için genişletilmiş Huygens Fresnel prensibi kullanıldı. Kısmi eş fazlı düz tepeli, kosinüs Gauss, kosinüs hiperbolik Gauss ve bunların kısmi eş fazlı formundaki ışık huzmeleri için eksen üzeri ve eksen dışı geçirgenlik

incelendi. Carter tanımı yardımıyla kısmi eş fazlı düz tepeli ışık huzmesi için ışın yayılması gözlemlendi. Parıldama hesaplamaları için yine genişletilmiş Huygens Fresnel prensibinden yararlanıldı. Bunların dışında, okyanus türbülansının sualtı kablosuz optik haberleşme sistemlerinin önemli kriterlerden olan bit hata oranı üzerine etkisi gözlemlendi. Hesaplamalar MATLAB programı kullanılarak elde edildi. Bütün sistem performans ölçütlerine karşılık ortalama kare sıcaklık dağılım oranı, sıcaklık ve tuzluluk katkılarının kırılma indisi spektrumuna oranı, birim sıvı kütlesi için kinetik enerjinin dağılım hızı gibi önemli okyanus türbülansı parametreleri bu tez çalışmasında incelendi. Dahası eş fazlılık derecesi ve eksen dışı parametresi bu tezde gözlemlendi. Bu tez ile sualtı türbülanslı ortam için uygun huzmelerin seçilmesi hedeflenmiş ve çeşitli uyarımlar altında UWOC linklerinin performansları farklı yönlerden incelenmiştir.

Anahtar Kelimeler: Sualtı Kablosuz Optik Haberleşme, Okyanus Türbülansı, Ortalama Geçirgenlik, Işın Yayılımı, Parıldama, Bit Hata Oranı, Kısmi Eş Fazlı Düz Tepeli Işık Huzmesi, Kısmi Eş Fazlı Kosinüs Gauss Işık Huzmesi, Kosinüs Gauss Işık Huzmesi, Kısmi Eş Fazlı Hiperbolik Kosinüs Gauss Işık Huzmesi, Kosinüs Gauss Işık Huzmesi.

I would like to dedicate this thesis to my precious Ali İsmet Öztürk, whose presence adds a new meaning to my life, who always keep me strong with his endless love and selfless support.



ACKNOWLEDGEMENTS

I would like to express my sincere gratitude to my supervisor, Yahya Kemal Baykal, for his guidance that gives new directions to my academic career, for his patience and for his continuous support. He has been truly an idol for me, as a great scientist, as a great mentor, as a kind and caring person.

In addition, I would like to express my special thanks to my committee members, Serap Altay Arpali and Çağlar Arpali, for their valuable supervisions and contributions. As well, I thank a lot to Muhsin Caner Gökçe who is not just one of the juries but also my instructor and my friend. I have learned a lot from his experience and guidance, and it has always been a pleasure for me to work with him.

Moreover, I present my special thanks to the special NASA engineer, Özgür Tümüklü, who has always been my greatest foul-weather friend, motivator, and power supplier.

I also thank my young friend and supporter, Mehmet Duhan Işıksalan whom I sincerely believe will be successful at what he is doing.

Additionally, I want to thank the dearest Fuli for her never-ending love and beautiful energy that make me work all night long.

Lastly, I want to express my gratitude to my family who has always been my greatest supporter all through my life with their greatest love and devotion. I am also grateful to my brother, my dearest friend for his never-ending support. Without my family, I am aware that I would be far away from reaching my goals. I am very lucky to have that precious family.

TABLE OF CONTENTS

STATEMENT OF NON-PLAGIARISM PAGE	iii
ABSTRACT	iv
ÖZ	vi
ACKNOWLEDGEMENTS	ix
TABLE OF CONTENTS	x
LIST OF FIGURES	xiii
LIST OF TABLES	xx
LIST OF ABBREVIATIONS	xxi
LIST OF SYMBOLS	xxii
CHAPTERS:	
1. INTRODUCTION	1
1.1 Background	1
1.2 Objectives	8
1.3 Thesis Outline.....	9
2. LASER BEAM PROPAGATION IN OCEANIC TURBULENCE	10
2.1 Oceanic Turbulence.....	10
2.2 Beam Types	12
2.1.1 Gaussian Beam Wave	12
2.2.2 Multi Beams.....	13
2.2.2.1 Flat-Topped Beam Wave	14
2.2.2.2 Cosine-Gaussian Beam Wave	15
2.2.2.3 Cosine-Hyperbolic Gaussian Beam Wave	15

2.3	Extended Huygens Fresnel Principle.....	16
2.4	Average Intensity at Receiver plane for General Beam Types in Underwater	17
2.4.1	Average Intensity for Gaussian Beam	24
2.4.2	Average Intensity for Flat-Topped Beam	25
2.4.3	Average Intensity for Cosine-Gaussian Beam.....	26
2.4.4	Average Intensity for Cosine-Hyperbolic Gaussian Beam.....	27
3.	AVERAGE TRANSMITTANCE IN UNDERWATER MEDIUM.....	28
3.1	Methodology	28
3.2	Results for Average Transmittance of Partially Coherent Gaussian Beam in Underwater Medium.....	30
3.3	Results for Average Transmittance of Partially Coherent Flat-Topped Beam in Underwater Medium.....	33
3.4	Results for Off-axis Average Transmittance of Partially Coherent Flat-Topped Beam in Underwater Medium	38
3.5	Results for the Average Transmittance of Cosine Gaussian Beam in Underwater Medium.....	44
3.6	Results for Off-axis Average Transmittance of Partially Coherent Cosine Gaussian Beam in Underwater Medium.....	48
3.7	Results for the Average Transmittance of Cosine Hyperbolic Gaussian Beam in Underwater Medium.....	51
3.8	Results for Off-axis Average Transmittance of Partially Coherent Cosine Hyperbolic Gaussian Beam in Underwater Medium.....	55
3.9	Conclusion.....	58
4.	BEAM SPREAD.....	61
4.1	Methodology for Beam Spread of Partially Coherent Flat-Topped Beam in Underwater Medium.....	61
4.2	Results for Beam Spread of a Partially Coherent Flat-Topped Beam in Underwater Medium.....	65

4.3 Conclusion.....	71
5. INTENSITY SCINTILLATION.....	73
5.1 Methodology of Scintillation Index	73
5.2 Results for Scintillation of Cosine-Gaussian beam in Underwater	84
5.3 Results for Scintillation of Cosine-Hyperbolic Gaussian beam in Underwater.....	90
5.4 Comparison of Cosine Gaussian Beam and Cosine-Hyperbolic Gaussian Beam Scintillation in Underwater Medium	95
6. BIT ERROR RATE (BER)	97
6.1 Methodology of Bit Error Rate.....	97
6.2 Results for BER of Cosine Gaussian Beam	97
6.3 Results for BER of Cosine-Hyperbolic Gaussian Beam	100
6.4 Comparison of Cosine & Cosine-Hyperbolic Gaussian Beams BER Performance.....	103
7. CONCLUSION.....	105
REFERENCES.....	109
APPENDICES	126

LIST OF FIGURES

FIGURES

Figure 1 Intensity profile of Gaussian beam wave. (a) 2D beam profile, (b) 3D beam profile.	13
Figure 2 Intensity profile of flat-topped beam wave. (a) 2D beam profile, (b) 3D beam profile.	14
Figure 3 Intensity profile of cosine-Gaussian beam wave. (a) 2D beam profile, (b) 3D beam profile.....	15
Figure 4 Intensity profile of cosine-hyperbolic Gaussian beam wave. (a) 2D beam profile, (b) 3D beam profile.	16
Figure 5 Average transmittance of partially coherent Gaussian beam versus propagation distance L for different partial coherence degrees ρ_s	31
Figure 6 Average transmittance of partially coherent Gaussian beam versus propagation distance L for different ratio of temperature and salinity contributions to the refractive index spectrum ω	31
Figure 7 Average transmittance of partially coherent Gaussian beam versus propagation distance L for different rate of dissipation of mean square temperature χ_T	32
Figure 8 Average transmittance of partially coherent Gaussian beam versus propagation distance L for different rate of dissipation of kinetic energy for unit mass of fluid ε	33
Figure 9 The average transmittance of partially coherent flat-topped beam versus propagation distance L for different various numbers of beams composing the flat-topped beam N	34
Figure 10 The average transmittance of partially coherent flat-topped beam versus propagation distance L for different partial coherence values ρ_s	34

Figure 11	The average transmittance of the partially coherent flat-topped beam versus partial coherence level ρ_s for different numbers of beams composing the flat-topped beam N	35
Figure 12	The average transmittance of partially coherent flat-topped beam versus the ratio of temperature and salinity contributions to the refractive index spectrum ω for different partially coherence values ρ_s	36
Figure 13	The average transmittance of partially coherent flat-topped beam versus the rate of dissipation of mean square temperature χ_T for different partially coherence values ρ_s	37
Figure 14	The average transmittance of partially coherent flat-topped beam versus the rate dissipation of kinetic energy per unit mass of fluid ε for different partially coherence values ρ_s	37
Figure 15	The average transmittance of the partially coherence flat topped beam versus the rate of dissipation of kinetic energy per unit mass of fluid ε for various numbers of beams composing the flat-topped beam N	39
Figure 16	The average transmittance of partially coherence flat-topped beam versus the rate of dissipation of kinetic energy per unit mass of fluid ε for different source size values α_s	39
Figure 17	The average transmittance of partially coherent flat topped beam versus the rate of dissipation of mean square temperature χ_T for various numbers of beams composing the flat-topped beam N and off-axis parameter r_x	40
Figure 18	The average transmittance of partially coherent flat-topped beam versus the rate of dissipation of mean square temperature χ_T for various degrees of partial coherence ρ_s	41
Figure 19	The average transmittance of partially coherent flat-topped beam versus the ratio of temperature and salinity contributions ω for various degrees of partial coherence ρ_s	41

Figure 20	The average transmittance of partially coherent flat-topped beam versus the ratio of temperature and salinity contributions ω for different source sizes α_s .	42
Figure 21	The average transmittance of partially coherent flat-topped beam versus off-axis parameter r_x for various numbers of beams composing the flat-topped beam N .	43
Figure 22	The average transmittance of partially coherent flat-topped beam versus propagation distance L for different wavelength values λ .	43
Figure 23	Average transmittance of cos-Gaussian beam versus the rate of dissipation of kinetic energy per unit mass of fluid ε for different displacement parameters V .	45
Figure 24	Average transmittance of cos-Gaussian beam versus the rate of dissipation of kinetic energy per unit mass of fluid ε for different source size α_s values.	45
Figure 25	Average transmittance of cos-Gaussian beam versus the ratio of temperature and salinity contributions ω for different displacement parameter V .	46
Figure 26	Average transmittance of cos-Gaussian beam versus the ratio of temperature and salinity contributions ω for different source size α_s .	47
Figure 27	Average transmittance of cos-Gaussian beam versus the rate of dissipation of mean square temperature χ_T for different displacement parameter V .	47
Figure 28	Average transmittance of cos-Gaussian beam versus the rate of dissipation of mean square temperature χ_T for different source size α_s .	48
Figure 29	Off-axis average transmittance of partially coherent cos-Gaussian beam versus ε , for different off-axis parameters r_x .	49
Figure 30	Off-axis average transmittance of partially coherent cos-Gaussian beam versus χ_T , for different displacement parameters V_r .	50
Figure 31	Off-axis average transmittance of partially coherent cos-Gaussian versus ω , for various degrees of partially coherence ρ_s .	51

Figure 32 Average transmittance of cosh-Gaussian beam versus the rate of dissipation of kinetic energy per unit mass of fluid ε for different displacement parameters V	52
Figure 33 Average transmittance of cosh-Gaussian beam versus the rate of dissipation of kinetic energy per unit mass of fluid ε for different source size, α_s values.....	52
Figure 34 Average transmittance of cosh-Gaussian beam versus the ratio of temperature and salinity contributions ω for different displacement parameter V	53
Figure 35 Average transmittance of cosh-Gaussian beam versus the ratio of temperature and salinity contributions ω for different source size α_s ..	54
Figure 36 Average transmittance of cosh-Gaussian beam versus the rate of dissipation of mean square temperature χ_T for different displacement parameters V	55
Figure 37 Average transmittance of cosh-Gaussian beam versus the rate of dissipation of mean square temperature χ_T for different source sizes α_s .	55
Figure 38 Off-axis average transmittance of partially coherent cosh-Gaussian versus ε , for different off-axis parameters r_x	56
Figure 39 Off-axis average transmittance of partially coherent cosh-Gaussian versus χ_T , for different displacement parameters.	57
Figure 40 Off-axis average transmittance of partially coherent cosh-Gaussian versus ω , for various degrees of partially coherence ρ_s	57
Figure 41 On-axis average transmittance versus propagation distance L , for different beam types.....	60
Figure 42 Off-axis average transmittance versus propagation distance L , for different beam types.....	60
Figure 43 The beam spread due to oceanic turbulence versus the rate of dissipation of mean square temperature χ_T for various number of beams composing the flat-topped beam N	66

Figure 44	The beam spread due to oceanic turbulence versus the rate of dissipation of mean square temperature χ_T for various degree of partial coherence ρ_s .	66
Figure 45	The beam spread due to oceanic turbulence versus the rate of dissipation of mean square temperature χ_T for different source size α_s values.	67
Figure 46	The beam spread due to oceanic turbulence versus the rate of dissipation of kinetic energy per unit mass of fluid ε for various degree of partial coherence ρ_s .	68
Figure 47	The beam spread due to oceanic turbulence versus the rate of dissipation of kinetic energy per unit mass of fluid ε for different source size α_s .	68
Figure 48	The beam spread due to oceanic turbulence versus the ratio of temperature and salinity contributions ω for various degree of partial coherence ρ_s .	69
Figure 49	The beam size in r_x direction at the receiver plane versus the rate of dissipation of kinetic energy per unit mass of fluid ε for various number of beams composing the flat-topped beam N	70
Figure 50	The beam size in r_x direction at the receiver plane versus the ratio of temperature and salinity contributions ω for various number of beams composing the flat-topped beam N	70
Figure 51	The beam size in r_x direction at the receiver plane versus the ratio of temperature and salinity contributions ω for different source size values α_s .	71
Figure 52	Scintillation index of cos-Gaussian beam versus the source size α_s for different ε .	85
Figure 53	Scintillation index of cos-Gaussian beam versus the source size α_s for different ω .	86
Figure 54	Scintillation index of cos-Gaussian beam versus the source size α_s for different V_r .	86
Figure 55	Scintillation index of cos-Gaussian beam versus the rate of dissipation of kinetic energy per unit mass of fluid ε for different V_r .	87

Figure 56 Scintillation index of cos-Gaussian beam versus the rate of dissipation of kinetic energy per unit mass of fluid ε for different ω	88
Figure 57 Scintillation index of cos-Gaussian beam versus the propagation distance L for different wavelengths λ	88
Figure 58 Scintillation index of cos-Gaussian beam versus the rate of dissipation of mean square temperature χ_T for different ε	89
Figure 59 Scintillation index of cos-Gaussian beam versus the rate of dissipation of mean square temperature χ_T for different ω	90
Figure 60 Scintillation index of cosh-Gaussian beam versus the source size α_s for different L	91
Figure 61 Scintillation index of cosh-Gaussian beam versus the source size α_s for different V	92
Figure 62 Scintillation index of cosh-Gaussian beam versus the source size α_s for different ω	92
Figure 63 Scintillation index of cosh-Gaussian beam versus the source size α_s for different ε	93
Figure 64 Scintillation index of cosh-Gaussian beam versus the rate of dissipation of kinetic energy per unit mass of fluid ε for different V	94
Figure 65 Scintillation index of cosh-Gaussian beam versus the rate of dissipation of kinetic energy per unit mass of fluid ε for different wavelengths.	94
Figure 66 Comparison of the scintillation index of cos-Gaussian and cosh-Gaussian beam versus the source size α_s for different L	95
Figure 67 BER of cosine-Gaussian beam versus SNR in oceanic turbulence for various rates of dissipation of kinetic energy values.....	98
Figure 68 BER of cosine-Gaussian beam versus SNR in oceanic turbulence for various displacement parameters.	99
Figure 69 BER of cosine-Gaussian beam versus SNR in oceanic turbulence for various ratios of temperature and salinity contribution.....	99
Figure 70 BER of cosine-Gaussian beam versus SNR in oceanic turbulence for various rates of dissipation of mean square temperature.	100

Figure 71 BER of cosine-hyperbolic Gaussian beam versus SNR in oceanic turbulence for various rates of dissipation of kinetic energy values.	101
Figure 72 BER of cosine-hyperbolic Gaussian beam versus SNR in oceanic turbulence for various rates of dissipation of kinetic energy values.	101
Figure 73 BER of cosine-hyperbolic Gaussian beam versus SNR in oceanic turbulence for various displacement parameters.	102
Figure 74 BER of cosine-hyperbolic Gaussian beam versus SNR in oceanic turbulence for various ratios of temperature and salinity contribution.	102
Figure 75 BER of cosine-hyperbolic Gaussian beam versus SNR in oceanic turbulence for various rates of dissipation of mean square temperature.	103
Figure 76 BER versus SNR in oceanic turbulence for comparison of the cosine and cosine-hyperbolic Gaussian beams.	104

LIST OF TABLES

Table 1 Obtained results from figures.	107
--	-----



LIST OF ABBREVIATIONS

AUV	Autonomous Underwater Vehicle
BER	Bit Error Rate
BPSK	Binary Phase Shift Keying
CGCSM	Cosine-Gaussian-Correlated Schell Model
DCO	Direct Current biased Optical
DPSK	Differential Phase Shift Keying
FTVH	Flat-Topped Vortex Hollow
GSM	Gaussian Schell Model
LDPC	Low-Density Parity-Check
LED	Light Emitting Diode
MGSM	Multi-Gaussian Schell Model
NUC	Non-Uniformly Correlated
OFDM	Orthogonal Frequency Division Multiplexing
OOK	On-Off Keying
OWC	Optical Wireless Communication
PCFT	Partially Coherent Flat-Topped
PPM	Pulse Position Modulated
PSK	Phase Shift Keying
RGB	Red, Green and Blue
ROV	Remotely Operated Vehicle
SNR	Signal to Noise Ratio
TEM	Transverse Electro-Magnetic
UWOC	Underwater Wireless Optical Communication

LIST OF SYMBOLS

C_n^2	Index-of-refraction structure constant in atmosphere
$\Phi(\kappa)$	The power spectrum model of turbulence
θ	The eddy momentum transfer coefficient
κ	Scalar spatial frequency
η	Kolmogorov inner scale
ℓ_0	Inner scale of turbulence
L_0	Outer scale of turbulence
ε	Rate of dissipation of kinetic energy per unit mass of fluid
X_T	Rate of dissipation of mean-squared temperature
ω	Ratio of temperature to salinity contributions to the refractive index spectrum
$U_0(\mathbf{s}, 0)$	Laser beam profile at source plane
α_s	Laser source size
a_0	Amplitude of the laser field
k	Wave number
λ	Wavelength
\mathbf{s}	Source transverse coordinate
\mathbf{r}	Receiver transverse coordinate
F_0	Radius of curvature
$u_{inc}(s_x, s_y, z = 0)$	The incident field at the source plane
z	Propagation axis
A_l	Amplitude of each beam composing the multi-beam
V_l	Complex displacement parameters

N	The number of beams composing the multi beam
L	Link distance
$u(\mathbf{r}, L)$	Received optical field
$\psi(\mathbf{s}, \mathbf{r})$	The random part of the complex phase of a spherical wave
$\langle \rangle$	Ensemble average over the random medium statistics
$\langle I(\mathbf{r}, z = L) \rangle$	Average intensity at the receiver
$\rho_{0_{-uw}}^2$	Coherence length of the underwater medium
ρ_s	Degree of source coherence level
$\langle \tau_t \rangle$	Average transmittance normalized by the received intensity without turbulence
$\langle \tau_s \rangle$	Average transmittance normalized by the intensity at the source plane
σ_x	Effective beam spot
$\Delta\sigma_{xL}$	Beam spread
$\sigma_{xL_{-uw}}(z = L)$	Beam size in r_x direction at receiver plane after beam propagates in oceanic turbulent medium
$\sigma_{xL_{-fs}}(z = L)$	Beam size in r_x direction at receiver plane after beam propagates in free space
m^2	Scintillation index
$I(\mathbf{r}, L)$	Instantaneous intensity at the receiver
$\Gamma_4^m(\mathbf{s}_1, \mathbf{s}_2, \mathbf{s}_3, \mathbf{s}_4, \mathbf{r})$	Fourth order spherical-wave coherence function of the medium
B_z	Log amplitude correlation function
D_ψ	Wave structure function
$D_{\chi S}$	Log-amplitude and phase structure function
σ_χ^2	Log amplitude variance
$\rho_{\chi S}$	Coherence length of log amplitude and phase

$\langle I^2(\mathbf{p}, L) \rangle$	Average of the square of the intensity
$p_I(\cdot)$	Probability density function
$erfc(\cdot)$	Complementary error function



CHAPTER 1

INTRODUCTION

1.1 Background

Although UWOC is not a new research field, it has become popular in recent years due to the fact that growing human activities in the ocean and the need for high data rate transmission are gradually increasing. In particular, the applications such as military, oceanography research, marine topography mapping, pollution monitoring, oil research, marine fishing industry, sensor networks and observatories, security harbor inspections, unmanned vehicles or devices, AUV communications and ROV require high bandwidth and high information transfer capacity [1-5]. The wireless communication system that is frequently used in recent underwater applications is based on acoustic communication system. With the aid of acoustic communication, long-distance (up to kilometers) communication is possible with low energy consumption [2,6]. However, the delay is substantial in the acoustic systems and it can be problematic in communication systems such as video transfer requiring high data transmission [7-11], and real-time applications. The most obvious disadvantages of acoustic communication systems are low bandwidth, high latency, high transmission losses [1-3,12-14]. The data rate for short distances in acoustic communication can be up to 500 kilobits per second. However, various underwater vehicles and sensor networks may need tens of megabits per second data rate. Fiber and copper cables can be used in fixed and large devices in order to reach data rates around megabit per second. However, wired systems not only require high engineering and maintenance but also cause installation difficulties [1]. For this reason, the most dominant solution for the requirement of high data rate is UWOC due to its characteristics such as large-data transfer, higher bandwidth, and low

latency [15-19]. UWOC provides an opportunity to tackle the problems that exist in acoustics, but due to the nature of the aquatic environment and the optical wave becomes highly attenuated in underwater, thus cannot travel very far. As a result, UWOC can be an effective solution for short distances.

The energy of the optical wave sent from underwater decreases significantly towards the receiver. The most important reasons for this reduction are mainly absorption and scattering depending on water types, and turbulence [1,3,19-22]. Generally speaking, absorption and scattering result from seawater constituents such as dissolved salt, chlorophyll, suspended particles and water molecules. The characteristics of the water vary depending upon the constitutive molecules of water, the dissolved substances, the geographical location, the distance from the shore, the depth, and so on. In the literature, water is classified into four main types. Namely, pure seawater, clear ocean water, coastal ocean water, and turbid harbor water [1,23-27]. The important parameter in pure seawater is absorption. The most prominent source of absorption is salt particles and the appropriate wavelength is the visible spectrum (i.e. 400-700nm) [1,3,6]. Clear ocean water has a higher concentration of dissolved particles and scattering starts to be a problem. While scattering is more effective at low wavelengths, absorption in pure seawater is the deterministic factor. In other words, while absorption causes attenuation in the clear ocean, it causes scattering attenuation when approaching the land due to the presence of organic matter. Therefore, the appropriate wavelength changes from blue (about 470 nm) to green (about 550 nm) as it is closer to the land. The signal with least attenuation through the propagation is at this wavelength range. While absorption is the main factor for pure seawater and clear ocean water, the absorption effect decreases as it approaches the land since organic matter and suspended particles cause scattering. Therefore, the suitable wavelength changes from blue-green to green-yellow [1,3,6]. In coastal ocean water, the problems associate both scattering and absorption as it consists of a large number of mineral components and planktonic matters. It should be noted that turbid harbor water has the highest concentration of dissolved matters [1,23].

Turbulence is one of the factors that significantly affect UWOC link performance [28]. Fluctuations in temperature, salinity, and density of ocean water cause changes in the refractive index of the ocean medium. This creates oceanic turbulence [1,3,29-30]. One of the most important studies in the field of oceanic turbulence was carried out by Nikishov and Nikishov. They defined the “contribution of salinity and temperature fluctuations to the refractive index spectrum in the ocean” [31]. Oceanic turbulence and its power spectrum will be discussed in detail with theoretical consideration in Section 2.1. In particular, one of the main effects of turbulence on second-order field moments is the average intensity [32-33].

In literature, many studies such as the normalized intensity, average intensity and the average transmittance have been conducted to examine the effect of turbulence. The average intensity was calculated by using the Rytov method and the extended Huygens-Fresnel principle [34]. Normalized intensity of beams such as FTVH [35], the Gaussian Schell model vortex [36], the radial phase-locked partially coherent standard Hermite-Gaussian [37], the partially coherent Lorentz [38-39], Lorentz beam [40] and partially coherent model beams [29] were analyzed in turbulent underwater medium. The average intensity of beams such as radial phase-locked multi-Gaussian Shell-model [41], random electromagnetic multi-Gaussian Schell-model vortex beam [42], partially coherent anomalous hollow vortex beam [43-44], Lorentz Gaussian [45], phase locked partially coherent radial flat-topped array laser [46], radially polarized twisted Gaussian-Schell model [47], four-petal Gaussian model [48] and MxN Gaussian array [49], rotating elliptical Gaussian [50] beams were examined in oceanic turbulence. The average intensity and beam quality of optical coherence lattices were analyzed in oceanic turbulence [51-52]. On-axis average intensity of the hollow Gaussian beam is analytically obtained [53]. Additionally, propagation of optical coherence lattices was examined in [54]. Intensity has been studied for many different beams for atmospheric turbulence. In particular, some of these are the average intensity of flattened Gaussian [55], and sinusoidal beams, cosine Gaussian and cosine-hyperbolic Gaussian beams [56-57].

Also, a partially coherent flat-topped beam has been experimentally produced and its intensity and coherence degree have been studied [58].

Another factor that examines the turbulence effect is the average transmittance [59,60]. Off-axis average transmittance of the partially coherent flat-topped beam [61], the transmittance of cos Gaussian and cosh-Gaussian beams [62], the transmittance of a finite-energy frozen beam [63], and the transmittance of the vortex modes carried by Mathieu-Gaussian beam [64] recently analyzed for the underwater environment. For the multi-Gaussian beam, the effect of anisotropy on oceanic turbulence was investigated [65]. Moreover, the average transmittance is calculated for focused collimated laser beams [66]. The flat-topped beam transmittance has been studied for anisotropic underwater turbulence [67]. Of course, there are many transmittance studies in atmospheric turbulence [68-70] as well. Annular beam, partially coherent cosine and cosine-hyperbolic beams [71] and partially coherent sources [72] were investigated in atmospheric turbulence.

Another difficulty in underwater communication performance is the intensity fluctuation (scintillation), which is the most important fourth-order statistical quantity of a wave [32,73-74]. For clear ocean, absorption and scattering cause less attenuation in light propagation than scintillation [75-76]. Optical turbulence occurs due to the difference in refractive indices. This causes fluctuation in the intensity as the light moves in a turbulent environment. Hence, it is a good alternative to examine scintillation to study the effects of turbulence. Note that scintillation will be examined in detail in Chapter 5.

There are many scintillation studies in the literature for both the atmosphere and the underwater environment. Scintillation calculations have been carried out for many different beam types in the underwater environment. Some of these are optical plane and spherical wave [77], Gaussian [78] and partially coherent Gaussian [79],

multimode laser beams [80], higher-order mode laser beam [81-83], cross-beam [84], partially coherent flat-topped laser beam [85], and phase-locked partially coherent flat-topped array laser beam [86]. In addition, scintillation was investigated for multiple-input single-output optical link [87] and LED source [88]. Eddy diffusivity ratio [3,89-90], anisotropy [91], and the effects of system parameters [28] on scintillation are among the studies conducted. Partially coherent beam scintillations were studied for weak oceanic turbulence [92], and plane and spherical wave scintillations were also investigated for strong oceanic turbulence [93-94]. Just recently, adaptive optics correlations of scintillations of Hermite-Gaussian modes have been published for oceanic turbulence [95]. To observe the effects of bubbles [96] and RGB laser [97], scintillations are examined. There are experimental studies for scintillation. It was observed that NUC increases scintillation when comparing NUC, GSM, and MGSM beams [98]. The other study is related to modeling a vehicle motion-induced turbulence. The relationship between propeller-induced turbulence and scintillation is investigated and it was observed that optical communication is clearly affected by the propeller-induced turbulence [99].

Intensity fluctuation in atmospheric turbulence is also commonly studied. Some of these are partially coherent off-axis Gaussian [100], flat-topped [101-104], cos Gaussian, and cosh-Gaussian [105-106], annular [107], super Lorentz Gaussian laser [108] beams are scintillation studies in atmospheric turbulent medium. Partially coherent multiple Gaussian [109], partially coherent general beam [110], higher-order laser beams [111] scintillation analyzes for atmospheric turbulence are also available in the literature. Additionally, the receiver aperture averaging effect on intensity fluctuations is investigated in a turbulent atmosphere [112].

Another topic commonly studied in the oceanic turbulence environment is the beam wander [53,113-118] and the beam spreading [41,118-120]. Partially coherent Hermite Gaussian beams [115,121], Gaussian array beams [122], Lorentz-Gauss vortex beam [123] are beam types whose spreading are calculated in underwater

turbulence. Angular spreading of the general type partially coherent beam was observed in the anisotropic oceanic turbulence [124]. Induced laser beam spread [125], and spreading of partially coherent beams [126], and spot size and divergence [127] were analyzed in atmospheric turbulence.

Similar to the scintillation index, the bit error rate (BER) is also one of the parameters that determine the performance of wireless optical communication links. BER was calculated for the Gaussian beam [128], focused Gaussian beam [129], asymmetrical Gaussian beam [130], asymmetrical optical beams [131], multi-mode beams [132], and phase-locked partially coherent flat-topped array laser beam [86] in the underwater. In addition, the effect of eddy diffusivity and anisotropy on BER in oceanic turbulence was investigated [90]. BER of PPM OWC link is formulated [133], performance of it was analyzed [134] and M-ary PPM is evaluated by [135-137]. Intensity modulation performance is examined using BPSK in weak oceanic turbulence [138-139], using M-ary PSK in strong oceanic turbulence [140-141], using PPM in anisotropic oceanic turbulence [142]. BER performance is investigated by using various modulation techniques such as OOK [137], DCO-OFDM [143], LDPC [144], DPSK [145], and Monte Carlo simulation [137,146]. System performance of UWOC is employed with using multi-pulse pulse position modulation in Ref. [147]. There are many BER performances investigations in turbulent ocean. Some of them are given by Ref. [148-151]. Some BER studies performed in the atmosphere are given in [106,152-153].

Another study that contributes greatly to underwater turbulence studies focuses on the equation that gives the equivalent of the atmospheric turbulence coefficient C_n^2 for oceanic turbulence [154]. The structure parameter of anisotropic atmospheric turbulence is expressed by oceanic anisotropic factors and the oceanic turbulence parameters in Ref. [155]. Apart from these, structure functions [156], field correlation [157], intensity correlation [158], propagation factors of the partially coherent model beam [159], propagation of the Bessel-Gaussian beam [160], the

propagation properties of partially coherent radially and azimuthally polarized rotating elliptical Gaussian beam [161], propagation properties of a twisted rectangular multi-Gaussian Schell model beam [162], and propagation behavior of partially coherent divergent Gaussian beams [163] were studied in underwater. Propagation characteristics of radially polarized beams [164] and propagation properties of a controllable rotating elliptical Gaussian coherence lattice [165] are investigated. Propagation of different partially coherent beam types is analyzed in the turbulent ocean [166-170]. Additionally, the effect of oceanic turbulence on the spectral density and the spectral degree of coherence of CGCSM beams [171], the effect of anisotropy on the radius curvature of general type partially coherent beam [172] are investigated in the ocean.

The evolution properties of partially coherent flat-topped vortex hollow beam [166] and radial phase locked partially coherent Lorentz-Gauss array beam [173], properties of multi-Gaussian Schell model beams [174], statistical characteristics of a twisted anisotropic Gaussian Schell-model beam [175] are investigated. A phase locked-partially coherent radial flat-topped array laser beam is analyzed about the behavior of propagation [167]. The wave structure function of plane and spherical waves are examined in oceanic turbulence [176]. For strong oceanic turbulence, aperture averaging [177], for weak to strong oceanic turbulence ultra-short pulses propagation [178] are examined. The polarization degree for PCFT beam in oceanic turbulent medium was analyzed [179]. Spectral changes in stochastic light beam in turbulent ocean is employed by Ref. [180]. Propagation of PCFT beam was also studied experimentally [181]. Another study in oceanic turbulence is the statistical properties of stochastic beam propagation [182]. Relations between the oceanic turbulence parameters and characteristics of Gaussian array beams are analyzed in Ref. [183]. SNR due to oceanic turbulence [184-186], and average capacity [187] were investigated for UWOC link.

Characteristics of bubble [188], quasi-omni-directional transmitter [189] for underwater turbulence were observed experimentally. Moreover, absorption and scattering effects on transmission [21] and centroid drift of laser beam propagation were analyzed experimentally [190].

Degree of coherence is another important second order field moment to observe the turbulence effects [32-33]. Most of the beam types used in intensity, transmittance, and scintillation studies we mentioned above are partially coherent beams and the degree of coherence effect has been investigated. Partially coherent beams are mostly used in the studies in the literature because, in practical applications, the sources are partially coherent. We also examined the partially coherent cases of the beam types we used in our study, and we observed that partially coherent beams were less affected by turbulence than coherent beams in our studies [61,191]. Complex degree of coherence [192] and optical beam propagation [193] of partially coherent beam source, and turbulence-induced degradation properties of partially coherent flat-topped beams [194] are some of the important works in atmospheric turbulence. Scintillation [19,195] and degree of spatial coherence [196] examinations were conducted in experimental studies to examine the underwater turbulence effect.

1.2 Objectives

This thesis aims not only to increase the performance of the UWOC system but also to contribute to the literature by examining the behavior of different beam types in a turbulent underwater environment. Average transmittance and beam spread together with other phenomena such as scintillation index and BER determine the performance of optical wireless communication links. In particular, these links increase their popularity of diver to diver, diver to a submarine, submarine to a diver and underwater sensor networks, underwater vehicle communication systems and a performance improvement is needed. In order to conduct this performance research, we examined three different beam types and their partially coherent states. Because of their practical applications, sources are usually used partially coherent and

partially coherent sources are more realistic than fully coherent and fully incoherent resources. Besides, as we have observed in other studies as well as in our studies, partially coherent sources are less affected by turbulence and suffer less distortion. In this thesis work, our aim is also to contribute to the selection of the appropriate beam type for the turbulent environment in underwater application by investigating the oceanic turbulence effects on the coherent and partially coherent states of flat-topped, cosine Gaussian and cosine hyperbolic Gaussian beams according to different entities, such as average transmittance, beam spread, scintillation and BER.

1.3 Thesis Outline

In Chapter 2, the concept of laser beam propagation is explained in detail. Especially oceanic turbulence formulation and turbulence parameters are described. The beam types used for producing from the general multi-beam formula are explained as well. More specifically, general multi-beam and flat-topped, cos-Gauss, and cosh-Gauss beams formulas are studied. The extended Huygens Fresnel principle that will be used for the propagation and the intensity calculations for the beams we produce are also investigated in this chapter. In Chapter 3, the average transmittance in the oceanic turbulent medium for flat-topped, cos-Gauss, cosh-Gauss beams, and their partially coherent forms are analyzed. Then, results on the average transmittance in oceanic turbulence are given in this chapter. Chapter 4 focuses on the beam spread of partially coherent flat-topped beams. The methodology and numerical results of the beam spread are given. In Chapter 5, the scintillation index being one of the important performance parameters of UWOC systems, which is again one of the most important fourth-order statistical quantities, is discussed. This chapter also includes numerical results of intensity fluctuation (scintillation) of the cos-Gauss and cosh-Gauss beams and comparison of both. Details about BER formulation and corresponding numerical results associated with cos & cosh- Gaussian beams along with their comparison are given in Chapter 6. Lastly, this thesis is completed with conclusions, as presented in Chapter 7.

CHAPTER 2

LASER BEAM PROPAGATION IN OCEANIC TURBULENCE

2.1 Oceanic Turbulence

Turbulence is a dominant physical process resulting from the temperature and mobility of the fluid and the proportions of dissolved organic/inorganic particles [197-198]. Oceanic turbulence is one of the main factors affecting the light propagation in underwater. Temperature, salinity and mobility are crucial parameters creating the optical turbulence and affecting the light propagation in underwater medium. Since, variations in temperature and salinity cause to change in refractive index of medium. Therefore, index of refraction defines the optical turbulence. On the other hand, fluctuations of the temperature and salinity determines the effect of oceanic turbulence. These fluctuations attenuate the signal propagation in underwater. Light wave propagation in oceanic turbulence is much more difficult than atmospheric turbulence due to the complexity and challenging medium of ocean. Although underwater medium is generally erratic and moving, oceanic turbulence can be explained and quantified [197]. Turbulence is defined by three basic assumptions, stationary, homogenous and isotropic [60]. Power spectrum of oceanic turbulence effect is defined under these assumptions. In this thesis, the power spectrum of oceanic turbulence which includes thermal diffusivity and diffusion of salt is homogenous and isotropic. The oceanic turbulence power spectrum $\Phi_n(\kappa)$ is expressed as [31,33,180,199].

$$\Phi_n(\kappa) = 0.388 \times 10^{-8} \varepsilon^{-1/3} \kappa^{-11/3} \left[1 + 2.35(\kappa\eta)^{2/3} \right] \times \frac{\chi_T}{\omega^2} \left(\omega^2 e^{-A_T \delta} + e^{-A_S \delta} - 2\omega e^{-A_{TS} \delta} \right), \quad (2.1)$$

where

$$\delta = 8.284(\kappa\eta)^{4/3} + 12.978(\kappa\eta)^2, \quad (2.2)$$

κ is the spatial frequency, η is the Kolmogorov micro scale length in m, ε is the rate of dissipation of kinetic energy per unit mass of fluid. Turbulent region of the ocean is most energetic. Breaking waves produce the motion. Transfers of the energy including motion is the important factor of turbulence. Deeper ocean is more regular than the surface and includes less mobility. From surface to deep in the ocean, mobility and kinetic energy depending on motion dissipates. Dissipation rate of kinetic energy of turbulent motion means that the mobility converts to heat with the help of viscosity. While motion decreases in the medium, heat increases. That causes the dispersion of kinetic energy. Thus, it can be said that ε determines the turbulent dissipation [197]. ε takes the value of the range from $10^{-1} \text{ m}^2/\text{s}^3$ to $10^{-10} \text{ m}^2/\text{s}^3$. Small values of ε means strong oceanic turbulence while large values of it defines the weak oceanic turbulence. χ_T is the rate of dissipation of the mean-squared temperature in K^2/s . Temperature is important measurement because it provides important information about the density, relation to heat energy, existence and movement of turbulent motion and its spatial variation. A measurable parameter χ_T defines the impact of the turbulence on the fluid temperature field [197]. Values of χ_T in the ocean range from $10^{-4} \text{ K}^2/\text{s}$ to $10^{-10} \text{ K}^2/\text{s}$. Upper and lower limit of χ_T reflect the strong and weak turbulence, respectively. ω is the unitless ratio of temperature and salinity contributions to the refractive index spectrum. ω takes the value of the range from -5 to 0 in oceanic turbulence. Lower bound of ω indicates that temperature-induced optical turbulence is dominant. If ω is about 0, the salinity-induced optical turbulence dominates the oceanic medium. Salinity-induced optical turbulence is much more strengthful than the temperature-induced optical turbulence. $A_T = 1.863 \times 10^{-2}$, $A_S = 1.9 \times 10^{-4}$, $A_{TS} = 9.41 \times 10^{-3}$ are constants.

2.2 Beam Types

2.1.1 Gaussian Beam Wave

Gaussian beam is an important solution of the paraxial Helmholtz equation. It is clearly revealing the properties of an optical beam. The intensity distribution of Gaussian beam wave is symmetrically centered about the beam axis in any transverse plane, the beam power is all around the beam axis, when the beam width decreases, the beam waist increases in both directions. Many types of lasers radiate light in Gaussian wave form [200]. Lowest order Gaussian beam is also named as TEM₀₀ wave. Gaussian beam wave function at the transverse plane $z = 0$, also called the source plane, is given in Equation 2.3 [201-202].

$$U_0(\mathbf{s}, 0) = a_0 \exp(-0.5\alpha k |\mathbf{s}|^2), \quad (2.3)$$

where

$$\alpha = 1/k\alpha_s^2 + i/F_0. \quad (2.4)$$

Eq. (2.3) can be written in a different form as seen below:

$$U_0(s, 0) = a_0 \exp(-s^2/2\alpha_s^2 - iks^2/2F_0), \quad (2.5)$$

where α is the complex parameter related to the spot size and phase front radius of curvature, a_0 is the field amplitude in $(\text{W}/\text{m}^2)^{1/2}$, $s = |\mathbf{s}| = (s_x^2 + s_y^2)^{1/2}$ is the transfer source coordinate in m (at receiver plane the transverse coordinate is shown by \mathbf{r}), s is the source transverse coordinate, α_s is the source size in m, $k = 2\pi/\lambda$ is the wave number in m^{-1} , λ is the wavelength, F_0 is the radius of curvature in m.

Intensity profile of Gaussian beam is plotted using MATLAB program for the source size $\alpha_s = 5$ cm, wavelength $\lambda = 532$ nm and the phase front radius of curvature $F_0 = \infty$ in Figure 1.

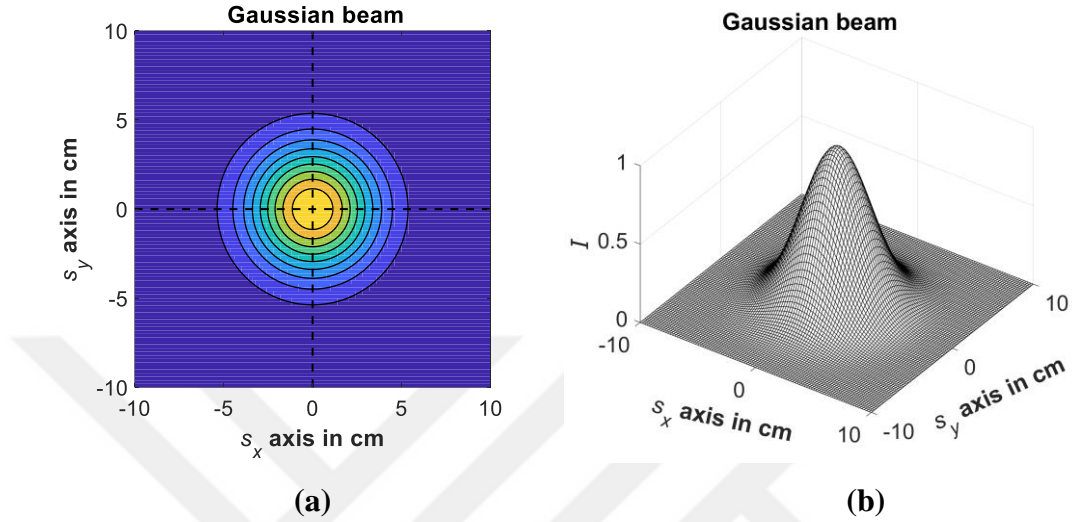


Figure 1 Intensity profile of Gaussian beam wave. (a) 2D beam profile, (b) 3D beam profile.

2.2.2 Multi Beams

The incident field at the source plane ($z=0$, where z is the propagation axis) for the general collimated multi-beam is given as [203]

$$u_{inc}(s_x, s_y, z=0) = \sum_{l=1}^N A_l \exp\left[-0.5\left(s_x^2/\alpha_{sxl}^2 + s_y^2/\alpha_{syl}^2\right)\right] \times \exp\left[-i\left(V_{xl}s_x + V_{yl}s_y\right)\right], \quad (2.6)$$

where N is the number of beams composing the multi beam, A_l is amplitude of each beam composing the multi-beam, V_{xl} and V_{yl} are complex displacement parameters in x and y directions which is defined $V_l = V_r + iV_i$. V_r and V_i are real and imaginary part of the complex displacement parameter, respectively. In all figures in this thesis,

V_i determines all imaginary part of the displacement parameter iV_i . α_{sxl} and α_{syl} are the source sizes in x and y directions.

2.2.2.1 Flat-Topped Beam Wave

Flat-topped beam is a special form of the general collimated multi-beam. If we define the amplitude and source size given below [101,103,109]

$$A_l = \frac{(-1)^{l-1}}{N} \binom{N}{l}, \quad \binom{N}{l} = \frac{N!}{l!(N-l)!}, \quad \alpha_{sl} = \alpha_s / \sqrt{l}, \quad (2.7)$$

and the displacement parameters V_{xl} and V_{yl} are taken be zero, then the flat-topped beam formulation can be obtained which is given in Eq. (2.8). The intensity profile of the flat-topped beam can be seen in Figure 2.

$$u_{inc}(s_x, s_y, z=0) = \sum_{l=1}^N \frac{(-1)^{l-1}}{N} \frac{N!}{l!(N-l)!} \exp\left[-0.5l\left(s_x^2/\alpha_{sxl}^2 + s_y^2/\alpha_{syl}^2\right)\right] \times \exp\left[-i\left(V_{xl}s_x + V_{yl}s_y\right)\right]. \quad (2.8)$$

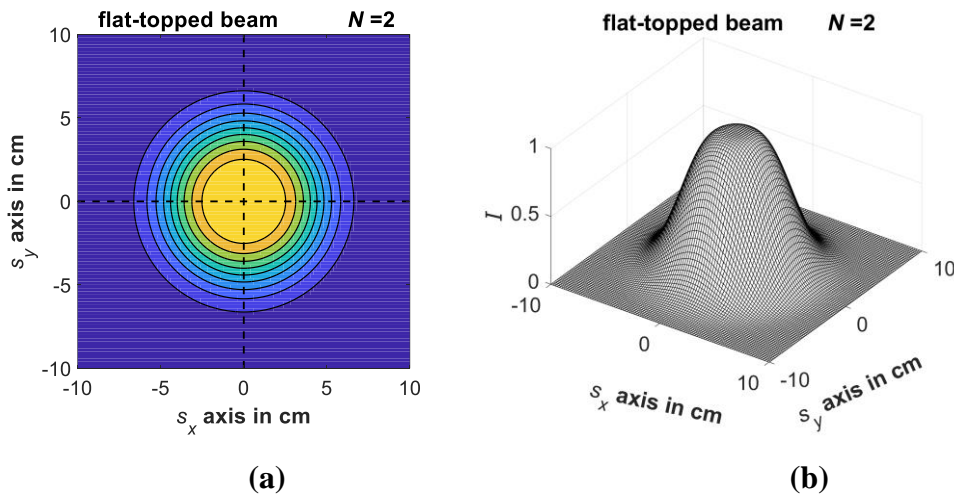


Figure 2 Intensity profile of flat-topped beam wave. (a) 2D beam profile, (b) 3D beam profile.

2.2.2.2 Cosine-Gaussian Beam Wave

Cosine-Gaussian beam can be obtained from the general beam formulation given Eq. (2.6). To obtain the cos-Gaussian beam amplitude A_l and displacement parameter V_l should be defined as [203]

$$A_l = [1/2 \quad 1/2], \quad V_l = [-V_r \quad V_r]. \quad (2.9)$$

If we substitute Eq. (2.9) into Eq. (2.6) we obtain cosine-Gaussian beam profile field. Multiplied by the conjugate, intensity profile is obtained and given in Figure 3.

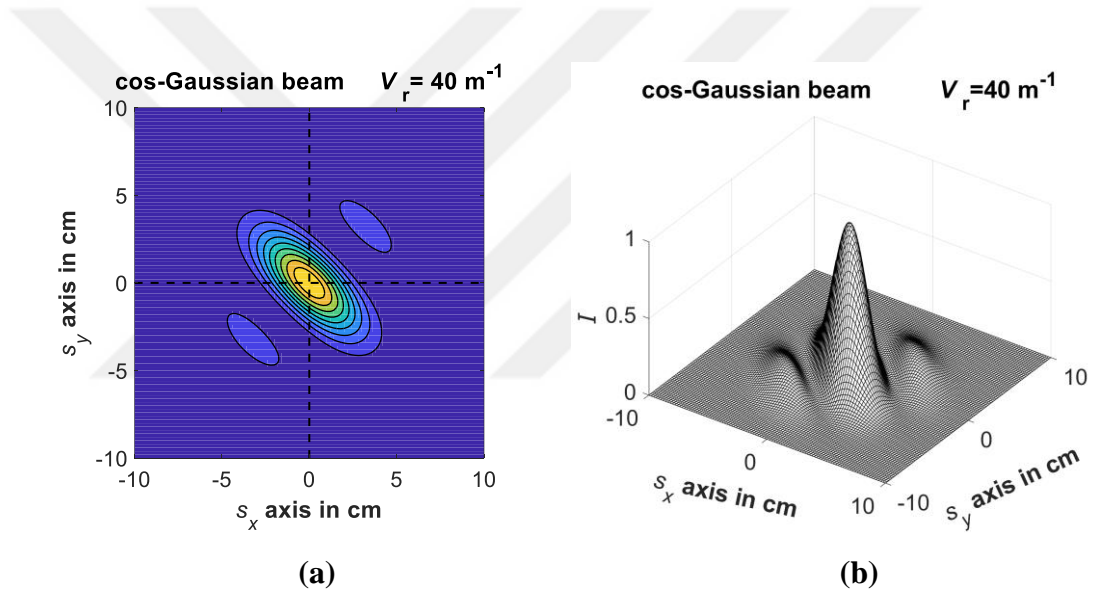


Figure 3 Intensity profile of cosine-Gaussian beam wave. (a) 2D beam profile, (b) 3D beam profile.

2.2.2.3 Cosine-Hyperbolic Gaussian Beam Wave

Cosine-hyperbolic beam wave is the special form of the general multi-beam like the flat-topped and cosine-Gaussian beam waves. It can be obtained from Eq. (2.6) applying the amplitude and complex displacement parameter values given below in Eq. (2.10) [203].

$$A_i = [1/2 \quad 1/2], \quad V_i = [iV_i \quad -iV_i]. \quad (2.10)$$

Figure 4 shows the intensity profile of the cosh-Gaussian beam wave.

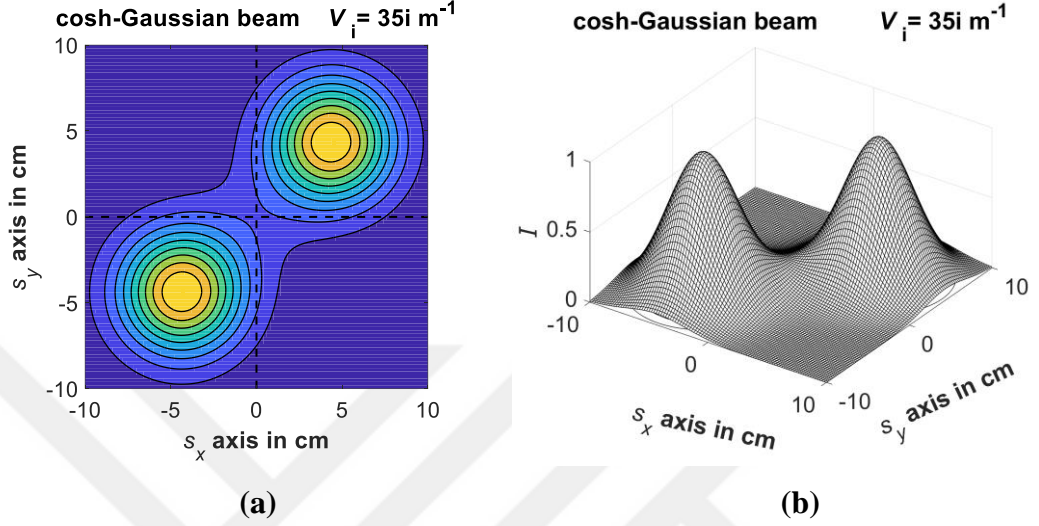


Figure 4 Intensity profile of cosine-hyperbolic Gaussian beam wave. (a) 2D beam profile, (b) 3D beam profile.

2.3 Extended Huygens Fresnel Principle

This theoretical study starts with the extended Huygens-Fresnel principle and applying it on the general multi-beam to calculate the intensity and transmittance. The extended Huygens Fresnel principle is defined as [201-202]

$$u(\mathbf{r}, L) = -\frac{ik}{2\pi\lambda} \exp(ikL) \int_{-\infty}^{\infty} \int_{-\infty}^{\infty} \mathbf{d}^2\mathbf{s} u(\mathbf{s}, z=0) \times \exp\left(\frac{ik}{2L} |\mathbf{s} - \mathbf{r}|^2\right) \exp[\psi(\mathbf{s}, \mathbf{r})], \quad (2.11)$$

where $u(\mathbf{s}, z=0)$ is the optical wave at source plane, $\psi(\mathbf{s}, \mathbf{r})$ is the random part of the complex phase of a spherical wave propagating in the turbulent medium from the point $(\mathbf{s}, 0)$ to the point (\mathbf{r}, L) . \mathbf{r} is the transverse coordinate at the receiver and L is

the propagation distance. Applying the extended Huygens Fresnel principle, the field at the receiver plane is obtained.

2.4 Average Intensity at Receiver plane for General Beam Types in Underwater

The average intensity at the receiver coordinate \mathbf{r} is calculated with the help of the extended Huygens Fresnel principle. For the intensity calculations, the receiver coordinate is taken to be $\mathbf{r}_1 = \mathbf{r}_2 = \mathbf{r}$. The average intensity calculation is found from [201-202]

$$\langle I(\mathbf{r}, z = L) \rangle = \langle u(\mathbf{r}, L) u^*(\mathbf{r}, L) \rangle, \quad (2.12)$$

where $*$ is the conjugate operator, $u^*(\mathbf{r}, L)$ is the conjugate of the field, $\langle \rangle$ is the ensemble averaging. Average intensity can be written in a different form:

$$\begin{aligned} \langle I(\mathbf{r}, L) \rangle &= \left(\frac{k}{2\pi L} \right)^2 \int_{-\infty}^{\infty} \int_{-\infty}^{\infty} \int_{-\infty}^{\infty} \int_{-\infty}^{\infty} d^2\mathbf{s}_1 d^2\mathbf{s}_2 u(\mathbf{s}_1) u^*(\mathbf{s}_2) \\ &\times \exp \left\{ \frac{ik}{2L} \left[|\mathbf{s}_1 - \mathbf{r}|^2 - |\mathbf{s}_2 - \mathbf{r}|^2 \right] \right\} \times \langle \exp \left[\psi(\mathbf{s}_1, \mathbf{r}) + \psi^*(\mathbf{s}_2, \mathbf{r}) \right] \rangle. \end{aligned} \quad (2.13)$$

Ensemble averaged term $\langle \exp \left[\psi(\mathbf{s}_1, \mathbf{r}) + \psi^*(\mathbf{s}_2, \mathbf{r}) \right] \rangle$ gives the turbulence effect on the average intensity. Then, ensemble averaging of turbulence field is given as [36,114,164]

$$\begin{aligned} \langle \exp \left[\psi(\mathbf{s}_1, \mathbf{r}) + \psi^*(\mathbf{s}_2, \mathbf{r}) \right] \rangle &= \exp \left[\frac{-\pi^2 k^2 L}{3} |\mathbf{s}_1 - \mathbf{s}_2|^2 \int_{-\infty}^{\infty} \kappa^3 \Phi_n(\kappa) d\kappa \right] \\ &= \exp \left(-\frac{|\mathbf{s}_1 - \mathbf{s}_2|^2}{\rho_{0_{uv}}^2} \right), \end{aligned} \quad (2.14)$$

where $\rho_{0_{uv}}^2$ is the coherence length of the underwater medium. Underwater coherence length that is obtained from Eq. (2.14) can be expressed in a different way as [114]

$$\rho_{0_oc}^2 = 3 / (\pi^2 k^2 L \int_0^\infty \kappa^3 \Phi_n(\kappa) d\kappa). \quad (2.15)$$

Coherence length ρ_s takes the value within the interval $[0, \infty]$. Note that when $\rho_s \rightarrow \infty$, the optical source is coherent and when it is equal to zero ($\rho_s = 0$), the source is incoherent. When ρ_s takes the value between zero and infinity, the source is called partially coherent.

This section includes intensity formulas as well as the intensity calculations required for our study. Beam types used in this thesis are examined as coherent and partially coherent. For this reason, the degree of coherence parameter ρ_s has been added to our intensity calculations [109,193].

$$\begin{aligned} \langle I(\mathbf{r}, L) \rangle = & \left(\frac{k}{2\pi L} \right)^2 \int_{-\infty}^{\infty} \int_{-\infty}^{\infty} \int_{-\infty}^{\infty} \int_{-\infty}^{\infty} d^2\mathbf{s}_1 d^2\mathbf{s}_2 u(\mathbf{s}_1) u^*(\mathbf{s}_2) \exp\left(\frac{1}{4\rho_s^2} |\mathbf{s}_1 - \mathbf{s}_2|^2 \right) \\ & \times \exp\left\{ \frac{ik}{2L} [|\mathbf{s}_1 - \mathbf{r}|^2 - |\mathbf{s}_2 - \mathbf{r}|^2] \right\} \langle \exp[\psi(\mathbf{s}_1, \mathbf{r}) + \psi^*(\mathbf{s}_2, \mathbf{r})] \rangle \end{aligned} \quad (2.16)$$

$\exp\left(\frac{1}{4\rho_s^2} |\mathbf{s}_1 - \mathbf{s}_2|^2 \right)$ gives the partially coherent effect on the intensity during the propagation. The general multi-beam we use as the incident beam $u_{inc}(s_x, s_y, z=0)$ defined in Eq. (2.6) is named as $u(\mathbf{s}_1)$. If we put Eq. (2.6) in the Eq. (2.16), we obtain following steps given below:

$$\begin{aligned}
\langle I(\mathbf{r}, L) \rangle &= \left(\frac{k}{2\pi L} \right)^2 \int_{-\infty}^{\infty} \int_{-\infty}^{\infty} \int_{-\infty}^{\infty} \int_{-\infty}^{\infty} ds_{1x} ds_{2x} ds_{1y} ds_{2y} \sum_{l_1=1}^N \sum_{l_2=1}^N A_{l_1} A_{l_2}^* \\
&\times \exp \left(-\frac{s_{1x}^2}{2\alpha_{sx l_1}^2} - \frac{s_{1y}^2}{2\alpha_{sy l_1}^2} - \frac{s_{2x}^2}{2\alpha_{sx l_2}^2} - \frac{s_{2y}^2}{2\alpha_{sy l_2}^2} \right) \\
&\times \exp \left\{ -i[(V_{xl_1} s_{1x} + V_{yl_1} s_{1y}) - (V_{xl_2}^* s_{2x} + V_{yl_2}^* s_{2y})] \right\} \quad (2.17) \\
&\times \exp \left[\frac{ik}{2L} (|\mathbf{s}_1 - \mathbf{r}|^2 - |\mathbf{s}_2 - \mathbf{r}|^2) \right] \\
&\times \exp \left(\frac{1}{4\rho_s^2} |\mathbf{s}_1 - \mathbf{s}_2|^2 \right) \exp \left(-\frac{1}{\rho_{0-oc}^2} |\mathbf{s}_1 - \mathbf{s}_2|^2 \right),
\end{aligned}$$

$$\begin{aligned}
\langle I(\mathbf{r}, L) \rangle &= \left(\frac{k}{2\pi L} \right)^2 \int_{-\infty}^{\infty} \int_{-\infty}^{\infty} \int_{-\infty}^{\infty} \int_{-\infty}^{\infty} ds_{1x} ds_{2x} ds_{1y} ds_{2y} \sum_{l_1=1}^N \sum_{l_2=1}^N A_{l_1} A_{l_2}^* \\
&\times \exp \left(-\frac{s_{1x}^2}{2\alpha_{sx l_1}^2} - \frac{s_{1y}^2}{2\alpha_{sy l_1}^2} - \frac{s_{2x}^2}{2\alpha_{sx l_2}^2} - \frac{s_{2y}^2}{2\alpha_{sy l_2}^2} \right) \\
&\times \exp \left(-iV_{xl_1} s_{1x} - iV_{yl_1} s_{1y} + iV_{xl_2}^* s_{2x} + iV_{yl_2}^* s_{2y} \right) \quad (2.18) \\
&\times \exp \left(\frac{ik}{2L} \left\{ [(s_{1x} - r_x)^2 + (s_{1y} - r_y)^2] - [(s_{2x} - r_x)^2 + (s_{2y} - r_y)^2] \right\} \right) \\
&\times \exp \left\{ -\left(\frac{1}{\rho_{0-oc}^2} + \frac{1}{4\rho_s^2} \right) [(s_{1x} - s_{2x})^2 + (s_{1y} - s_{2y})^2] \right\},
\end{aligned}$$

$$\begin{aligned}
\langle I(\mathbf{r}, L) \rangle &= \left(\frac{k}{2\pi L} \right)^2 \int_{-\infty}^{\infty} \int_{-\infty}^{\infty} \int_{-\infty}^{\infty} \int_{-\infty}^{\infty} ds_{1x} ds_{2x} ds_{1y} ds_{2y} \sum_{l_1=1}^N \sum_{l_2=1}^N A_{l_1} A_{l_2}^* \\
&\times \exp \left[s_{1x}^2 \left[-\frac{1}{2\alpha_{sx_1}^2} + \frac{ik}{2L} - \left(\frac{1}{\rho_{0_oc}^2} + \frac{1}{4\rho_s^2} \right) \right] \right. \\
&+ s_{1x} \left[-iV_{x_1} + 2s_{2x} \left(\frac{1}{\rho_{0_oc}^2} + \frac{1}{4\rho_s^2} \right) - 2\frac{ik}{2L} r_x \right] \left. \right] \\
&\times \exp \left(-\frac{s_{1y}^2}{2\alpha_{sy_1}^2} - \frac{s_{2x}^2}{2\alpha_{sx_2}^2} - \frac{s_{2y}^2}{2\alpha_{sy_2}^2} \right) \\
&\times \exp \left(-iV_{y_1} s_{1y} + iV_{x_2}^* s_{2x} + iV_{y_2}^* s_{2y} \right) \\
&\times \exp \left(\frac{ik}{2L} \left(-s_{2x}^2 + 2r_x s_{2x} + s_{1y}^2 - 2r_y s_{1y} - s_{2y}^2 + 2r_y s_{2y} \right) \right) \\
&\times \exp \left[\left(\frac{1}{\rho_{0_oc}^2} + \frac{1}{4\rho_s^2} \right) \left(-s_{2x}^2 - s_{1y}^2 + 2s_{1y} s_{2y} - s_{2y}^2 \right) \right].
\end{aligned} \tag{2.19}$$

With the help of the integration from Ref. [204]

$$\int_{-\infty}^{\infty} \exp(-p^2 x^2 \pm qx) dx = \exp\left(\frac{q^2}{4p^2}\right) \frac{\sqrt{\pi}}{p}, \quad [p > 0]. \tag{2.20}$$

we can see more clearly, if we name the part of Eq. (2.19),

$$\begin{aligned}
p_1^2 &= \left[\frac{1}{2\alpha_{sx_1}^2} - \frac{ik}{2L} + \left(\frac{1}{\rho_{0_oc}^2} + \frac{1}{4\rho_s^2} \right) \right] \\
q_1 &= \left[-iV_{x_1} + 2s_{2x} \left(\frac{1}{\rho_{0_oc}^2} + \frac{1}{4\rho_s^2} \right) - 2\frac{ik}{2L} r_x \right],
\end{aligned} \tag{2.21}$$

Eq. (2.19) is converted to

$$\begin{aligned}
\langle I(\mathbf{r}, L) \rangle &= \left(\frac{k}{2\pi L} \right)^2 \int_{-\infty}^{\infty} \int_{-\infty}^{\infty} \int_{-\infty}^{\infty} ds_{2x} ds_{1y} ds_{2y} \sum_{l_1=1}^N \sum_{l_2=1}^N A_{l_1} A_{l_2}^* \\
&\times \frac{\sqrt{\pi}}{\sqrt{\left[+\frac{1}{2\alpha_{sxl_1}^2} - \frac{ik}{2L} + \left(\frac{1}{\rho_{0-oc}^2} + \frac{1}{4\rho_s^2} \right) \right]}} \\
&\times \exp \left(\frac{\left[-\left(V_{xl_1} + \frac{k}{L} r_x \right)^2 \right]}{4 \left[+\frac{1}{2\alpha_{sxl_1}^2} - \frac{ik}{2L} + \left(\frac{1}{\rho_{0-oc}^2} + \frac{1}{4\rho_s^2} \right) \right]} \right) \\
&\times \exp \left(\frac{\left(\frac{1}{\rho_{0-oc}^2} + \frac{1}{4\rho_s^2} \right)^2}{\left[+\frac{1}{2\alpha_{sxl_1}^2} - \frac{ik}{2L} + \left(\frac{1}{\rho_{0-oc}^2} + \frac{1}{4\rho_s^2} \right) \right]} \right) \\
&\times \exp \left(-\left(\frac{1}{\rho_{0-oc}^2} + \frac{1}{4\rho_s^2} \right) - \frac{1}{2\alpha_{sxl_2}^2} - \frac{ik}{2L} \right) s_{2x}^2 \\
&\times \exp \left(\frac{\left\{ -i \left(V_{xl_1} + \frac{k}{L} r_x \right) \left(\frac{1}{\rho_{0-oc}^2} + \frac{1}{4\rho_s^2} \right) \right.}{\left[+\frac{1}{2\alpha_{sxl_1}^2} - \frac{ik}{2L} + \left(\frac{1}{\rho_{0-oc}^2} + \frac{1}{4\rho_s^2} \right) \right]} \right. \\
&\quad \left. \left. + \frac{ik}{L} r_x + iV_{xl_2}^* \right\} s_{2x} \right) \\
&\times \exp \left(-\frac{s_{1y}^2}{2\alpha_{syl_1}^2} - \frac{s_{2y}^2}{2\alpha_{syl_2}^2} \right) \exp(-iV_{yl_1} s_{1y} + iV_{yl_2}^* s_{2y}) \\
&\times \exp \left[\frac{ik}{2L} \left(+s_{1y}^2 - 2r_y s_{1y} - s_{2y}^2 + 2r_y s_{2y} \right) \right] \\
&\times \exp \left[\left(\frac{1}{\rho_{0-oc}^2} + \frac{1}{4\rho_s^2} \right) \left(-s_{1y}^2 + 2s_{1y} s_{2y} - s_{2y}^2 \right) \right].
\end{aligned} \tag{2.22}$$

Again, we named some parts of equation to see clearly, then to apply Eq. (2.20) on Eq. (2.22),

$$\begin{aligned}
p_2^2 &= \frac{-\left(\frac{1}{\rho_{0_oc}^2} + \frac{1}{4\rho_s^2}\right)^2}{\left[+\frac{1}{2\alpha_{sx1}^2} - \frac{ik}{2L} + \left(\frac{1}{\rho_{0_oc}^2} + \frac{1}{4\rho_s^2}\right)\right]} + \left(\frac{1}{\rho_{0_oc}^2} + \frac{1}{4\rho_s^2}\right) + \frac{1}{2\alpha_{sx2}^2} + \frac{ik}{2L} \\
q_2 &= \frac{-i\left(V_{xl_1} + \frac{k}{L}r_x\right)\left(\frac{1}{\rho_{0_oc}^2} + \frac{1}{4\rho_s^2}\right)}{\left[+\frac{1}{2\alpha_{sx1}^2} - \frac{ik}{2L} + \left(\frac{1}{\rho_{0_oc}^2} + \frac{1}{4\rho_s^2}\right)\right]} + \frac{ik}{L}r_x + iV_{xl_2}^*
\end{aligned} \tag{2.23}$$

$$\begin{aligned}
\langle I(\mathbf{r}, L) \rangle &= \left(\frac{k}{2\pi L} \right)^2 \int_{-\infty}^{\infty} \int_{-\infty}^{\infty} ds_{1y} ds_{2y} \sum_{l_1=1}^N \sum_{l_2=1}^N A_{l_1} A_{l_2}^* \\
&\times \frac{\sqrt{\pi}}{\sqrt{2\alpha_{sxl_1}^2 - \frac{ik}{2L} + \left(\frac{1}{\rho_{0-oc}^2} + \frac{1}{4\rho_s^2} \right)}} \\
&\times \exp \left\{ \frac{\left[-\left(V_{xl_1} + \frac{k}{L} r_x \right)^2 \right]}{4 \left[+\frac{1}{2\alpha_{sxl_1}^2} - \frac{ik}{2L} + \left(\frac{1}{\rho_{0-oc}^2} + \frac{1}{4\rho_s^2} \right) \right]} \right\} \\
&\times \exp \left\{ \frac{\left[\frac{-i \left(V_{xl_1} + \frac{k}{L} r_x \right) \left(\frac{1}{\rho_{0-oc}^2} + \frac{1}{4\rho_s^2} \right)}{\left(\frac{1}{2\alpha_{sxl_1}^2} - \frac{ik}{2L} + \frac{1}{\rho_{0-oc}^2} + \frac{1}{4\rho_s^2} \right)} + \frac{ik}{L} r_x + iV_{xl_2}^* \right]^2}{4 \left[\frac{-\left(\frac{1}{\rho_{0-oc}^2} + \frac{1}{4\rho_s^2} \right)^2}{\left(\frac{1}{2\alpha_{sxl_1}^2} - \frac{ik}{2L} + \frac{1}{\rho_{0-oc}^2} + \frac{1}{4\rho_s^2} \right)} + \frac{1}{\rho_{0-oc}^2} + \frac{1}{4\rho_s^2} + \frac{1}{2\alpha_{sxl_2}^2} + \frac{ik}{2L} \right]} \right\} \\
&\times \frac{\sqrt{\pi}}{\sqrt{\left[\frac{-\left(\frac{1}{\rho_{0-oc}^2} + \frac{1}{4\rho_s^2} \right)^2}{\left(\frac{1}{2\alpha_{sxl_1}^2} - \frac{ik}{2L} + \frac{1}{\rho_{0-oc}^2} + \frac{1}{4\rho_s^2} \right)} + \left(\frac{1}{\rho_{0-oc}^2} + \frac{1}{4\rho_s^2} \right) + \frac{1}{2\alpha_{sxl_2}^2} + \frac{ik}{2L} \right]}} \\
&\times \exp \left(-\frac{s_{1y}^2}{2\alpha_{syl_1}^2} - \frac{s_{2y}^2}{2\alpha_{syl_2}^2} \right) \exp(-iV_{yl_1} s_{1y} + iV_{yl_2}^* s_{2y}) \\
&\times \exp \left[\frac{ik}{2L} (+s_{1y}^2 - 2r_y s_{1y} - s_{2y}^2 + 2r_y s_{2y}) \right] \\
&\times \exp \left[\left(\frac{1}{\rho_{0-oc}^2} + \frac{1}{4\rho_s^2} \right) (-s_{1y}^2 + 2s_{1y} s_{2y} - s_{2y}^2) \right].
\end{aligned} \tag{2.24}$$

Then the average intensity is found to be

$$\begin{aligned}
\langle I(\mathbf{r}, L) \rangle = & \left(\frac{\pi}{\lambda L} \right)^2 \sum_{l_1=1}^N \sum_{l_2=1}^N \frac{A_{l_1} A_{l_2}^*}{-C^2 + BA} \\
& \times \exp \left\{ \frac{\left[\left(V_{l_1} + \frac{k}{L} r_x \right)^2 + \left(V_{l_1} + \frac{k}{L} r_y \right)^2 \right]}{-4A} \right\} \\
& \times \exp \left\{ \frac{\frac{1}{A} \left[-i \left(V_{l_1} + \frac{k}{L} r_x \right) C + iA \frac{k}{L} r_x + iA V_{l_2}^* \right]^2}{4(-C^2 + BA)}} \right\} \\
& \times \exp \left\{ \frac{\frac{1}{A} \left[-i \left(V_{l_1} + \frac{k}{L} r_y \right) C + iA \frac{k}{L} r_y + iA V_{l_2}^* \right]^2}{4(-C^2 + BA)}} \right\}, \tag{2.25}
\end{aligned}$$

where, $A = \frac{1}{2\alpha_{sl_1}^2} - \frac{ik}{2L} + \frac{1}{\rho_{0_oc}^2} + \frac{1}{4\rho_s^2}$, $B = \frac{1}{2\alpha_{sl_2}^2} + \frac{ik}{2L} + \frac{1}{\rho_{0_oc}^2} + \frac{1}{4\rho_s^2}$, and

$$C = \frac{1}{\rho_{0_oc}^2} + \frac{1}{4\rho_s^2}.$$

Obtaining results are checked with Ref. [112,205-206] for the limiting case of Eq. (2.25) by taking the same coherence lengths.

2.4.1 Average Intensity for the Gaussian Beam

The average intensity is calculated for the general beam in Section 2.4. Gaussian beam is the lowest order of the beam and it is not a multi-beam means $N = 1$. If we choose the $N = 1$ and $V_{xl} = V_{yl} = 0$ in Eq. (2.6), we obtain the Gaussian beam. Then, if we choose the same parameter in Eq. (2.25), this time we obtain the average intensity of the partially coherent Gaussian beam.

$$\begin{aligned} \langle I(\mathbf{r}, L) \rangle = & \left(\frac{\pi}{\lambda L} \right)^2 \frac{A_{l_1} A_{l_2}^*}{-C^2 + BA} \exp \left\{ \left[\left(\frac{k}{L} r_x \right)^2 + \left(\frac{k}{L} r_y \right)^2 \right] / (-4A) \right\} \\ & \times \exp \left\{ \frac{\left[-i \left(\frac{k}{L} r_x \right) C + iA \frac{k}{L} r_x \right]^2 + \left[-i \left(\frac{k}{L} r_y \right) C + iA \frac{k}{L} r_y \right]^2}{4A(-C^2 + BA)} \right\}. \end{aligned} \quad (2.26)$$

For on-axis average transmittance off-axis parameter takes the value $r_x = r_y = r = 0$,

$$\langle I(\mathbf{r}, L) \rangle = \left(\frac{\pi}{\lambda L} \right)^2 \frac{A_{l_1} A_{l_2}^*}{-C^2 + BA}. \quad (2.27)$$

2.4.2 Average Intensity for Flat-Topped Beam

The average intensity of the flat-topped beam is the special case of the multi beam. If we define displacement parameter $V_{xl} = V_{yl} = 0$, and the amplitude and source size given in Eq. (2.7), the average intensity of the partially coherent flat-topped beam becomes

$$\begin{aligned} \langle I(\mathbf{r}, L) \rangle = & \left(\frac{\pi}{\lambda L} \right)^2 \sum_{l_1=1}^N \sum_{l_2=1}^N \frac{A_{l_1} A_{l_2}^*}{-C^2 + BA} \\ & \times \exp \left\{ \left[\left(\frac{k}{L} r_x \right)^2 + \left(\frac{k}{L} r_y \right)^2 \right] / (-4A) \right\} \\ & \times \exp \left\{ \frac{\left[-i \frac{k}{L} r_x C + iA \frac{k}{L} r_x \right]^2 + \left[-i \frac{k}{L} r_y C + iA \frac{k}{L} r_y \right]^2}{4A(-C^2 + BA)} \right\}, \end{aligned} \quad (2.28)$$

where $A_l = \frac{(-1)^{l-1}}{N} \binom{N}{l}$, $\binom{N}{l} = \frac{N!}{l!(N-l)!}$, $\alpha_{sl} = \alpha_s / \sqrt{l}$. Eq. (2.27) gives the off-

axis average intensity. To obtain the on-axis average intensity, off-axis parameter

takes the value of $r_x = r_y = r = 0$, then the on-axis average intensity formula of the partially coherent flat-topped beam is

$$\langle I(\mathbf{r}, L) \rangle = \left(\frac{\pi}{\lambda L} \right)^2 \sum_{l_1=1}^N \sum_{l_2=1}^N \frac{A_{l_1} A_{l_2}^*}{-C^2 + BA} \quad (2.29)$$

2.4.3 Average Intensity for Cosine-Gaussian Beam

If we use the Eq. (2.25) with the values $N = 2$ and $A_{l_1} = [1/2 \ 1/2]$, $A_{l_2} = (A_{l_1})^*$, $V_{l_1} = [-V_r \ V_r]$, and $V_{l_2} = (V_{l_1})^*$, we obtain the off-axis average intensity of the partially coherent cosine-Gaussian beam as

$$\begin{aligned} \langle I(\mathbf{r}, L) \rangle &= \left(\frac{\pi}{\lambda L} \right)^2 \sum_{l_1=1}^N \sum_{l_2=1}^N \frac{A_{l_1} A_{l_2}^*}{-C^2 + BA} \\ &\times \exp \left\{ \frac{\left[\left(V_{l_1} + \frac{k}{L} r_x \right)^2 + \left(V_{l_1} + \frac{k}{L} r_y \right)^2 \right]}{-4A} \right\} \\ &\times \exp \left\{ \frac{\frac{1}{A} \left[-i \left(V_{l_1} + \frac{k}{L} r_x \right) C + iA \frac{k}{L} r_x + iA V_{l_2}^* \right]^2}{4(-C^2 + BA)}} \right\} \\ &\times \exp \left\{ \frac{\frac{1}{A} \left[-i \left(V_{l_1} + \frac{k}{L} r_y \right) C + iA \frac{k}{L} r_y + iA V_{l_2}^* \right]^2}{4(-C^2 + BA)}} \right\}. \end{aligned} \quad (2.30)$$

Then, if we want to calculate the on-axis average intensity of the partially coherent cosine-Gaussian beam, we take r_x and r_y to be equal to zero.

$$\begin{aligned} \langle I(\mathbf{r}, L) \rangle = & \left(\frac{\pi}{\lambda L} \right)^2 \sum_{l_1=1}^N \sum_{l_2=1}^N \frac{A_{l_1} A_{l_2}^*}{-C^2 + BA} \exp(V_{l_1}^2 / -2A) \\ & \times \exp \left\{ \frac{\left[-i(V_{l_1})C + iAV_{l_2}^* \right]^2 + \left[-i(V_{l_1})C + iAV_{l_2}^* \right]^2}{4A(-C^2 + BA)} \right\}. \end{aligned} \quad (2.31)$$

If we want to examine the fully coherent on-axis and off-axis average intensity, we take ρ_s as infinity, then A , B and C convert to Eq. (2.30) and (2.31) with

$$\begin{aligned} A &= \frac{1}{2\alpha_{sl_1}^2} - \frac{ik}{2L} + \frac{1}{\rho_{0-oc}^2}, \\ B &= \frac{1}{2\alpha_{sl_2}^2} + \frac{ik}{2L} + \frac{1}{\rho_{0-oc}^2}, \\ C &= \frac{1}{\rho_{0-oc}^2}. \end{aligned} \quad (2.32)$$

2.4.4 Average Intensity for Cosine-Hyperbolic Gaussian Beam

To obtain the off-axis average intensity of the partially coherent cosine-hyperbolic Gaussian beam, Eq. (2.30) is used with the parameters $N=2$ and $A_{l_1} = [1/2 \quad 1/2]$, $A_{l_2} = (A_{l_1})^*$, $V_{l_1} = [iV_i \quad -iV_i]$, and $V_{l_2} = (V_{l_1})^*$. With these parameters, Eq. (2.31) gives us the on-axis average intensity of the partially coherent cosh-Gaussian beam. If Eq. (2.30) and (2.32) is combined, off-axis average intensity of the fully coherent cosh-Gaussian beam can be obtained. On-axis average intensity of this beam with the coherent case can be examined by the combination of the Eqs. (2.30) and (2.31).

CHAPTER 3

AVERAGE TRANSMITTANCE IN UNDERWATER MEDIUM

This chapter focuses on the theoretical consideration of the optical transmittance with various beam types in underwater medium. In particular, the effects of oceanic turbulence on the average transmittance are closely examined when different types of optical beam waves propagate in a wireless underwater medium. For general beams, Huygens-Fresnel principle-based off- and on-axis transmittance are formulated in a homogeneous and isotropic turbulent oceanic medium for all observations of the average transmittance. General multi-beam formulation is then applied to multi-beam such as a flat-topped beam, cos-Gaussian beam, and cosh-Gaussian beam. The effects of the parameters of the oceanic turbulence power spectrum on the on-axis and off-axis average transmittance are analyzed as well. The analysis of the numerical results of the analytically obtained results is made with the aid of MATLAB program.

3.1 Methodology

The derivations of the optical transmittance model for the underwater environment are mostly based on those derived for the atmospheric environment due to extensive similarities of the light propagation properties. That is, the underwater optical wireless communication is inspired extensively by free-space and atmospheric optical models. Of course, there are some distinct features between the atmospheric and underwater optical transmittances especially in terms of the medium characteristics and the energy spectra [31]. Therefore, the derivations for underwater transmittance consider all these, as will be discussed next.

Our starting point is to apply the extended Huygens-Fresnel principle for the derivation of off-axis transmittance for the multi-Gaussian beam model. In particular, partially coherent flat-topped, cos, and cosh-Gaussian beams, which are derived from multi-beam definition, are studied to obtain the influence of different beam types on the on-axis and off-axis average transmittance for the underwater environment. To the best of the author's knowledge, off-axis transmittance of the partially coherent flat-topped beam, cosine, and cosine-hyperbolic Gaussian beams and their partially coherent forms for the underwater environment are studied for the first time. The average intensity is calculated with the help of the extended Huygens-Fresnel principle then it is normalized to find the average transmittance values.

Two different definitions can be used to find the average transmittance. More specifically, the first one deals with the average intensity at the receiver plane under the effect of turbulence normalized with respect to the average intensity at the receiver plane without turbulence effects. On the other hand, the second one defines the ratio of the average intensity at the receiver plane with the turbulence effects divided by the average intensity at the source plane. The former one is used to observe only the oceanic turbulence effects on the propagation of optical beam waves in the underwater medium. In this work, the former definition is used since our objective is to observe how much the environment weakens the transmittance by examining the light that has passed through a turbulent environment. In particular, the average intensity at the receiver plane under the effect of oceanic turbulence and the average intensity at the receiver plane without turbulence effects are given in Section 2.4. The average transmittances within the above definitions can be written in mathematical form of [20, 61]. The average transmittance normalized by the received intensity without turbulence is given as

$$\langle \tau_t \rangle = \frac{\langle I(\mathbf{r}, L) \rangle}{I^0(\mathbf{r}, L)}. \quad (3.1)$$

The average transmittance normalized by the intensity at the source plane is

$$\langle \tau_s \rangle = \frac{\langle I(\mathbf{r}, L) \rangle}{I(\mathbf{r}, z = 0)}. \quad (3.2)$$

3.2 Results for Average Transmittance of Partially Coherent Gaussian Beam in Underwater Medium

In this section, the average transmittance is analyzed when the partially coherent Gaussian beam propagates in underwater turbulence. The results are presented mainly by using the average transmittance definition in Eq. (3.1), i.e., by using the normalization with respect to the received intensity without turbulence. The variations of the on-axis average transmittances with respect to propagation distance for different turbulence parameters and coherency degrees are evaluated. For this section, the wavelength is chosen to be 532 nm, source size is used as 0.05 m and Kolmogorov microscale is 1 mm. Other parameters observed in this section $\rho_s = 10^{-3}$ m, $\varepsilon = 10^{-10}$ m²/s³, $\chi_T = 10^{-7}$ K²/s, $\omega = -0.3$ are used. The variation of the average transmittance is observed against the propagation distance L for different degrees of coherence values in Figure 5. Degree of coherence ρ_s takes the value within the interval $[0, \infty]$. 0 defines the incoherent source wave, ∞ determines the perfect coherency that was mentioned in Section 2.4. As seen in Figure 5, as the beam becomes more incoherent, the average transmittance increases. When the degree of coherence is close to the perfect coherency, the light beam is more affected by the turbulence. Average transmittance attains lower values for shorter propagation distances. Figure 5 agrees well with Ref. [71].

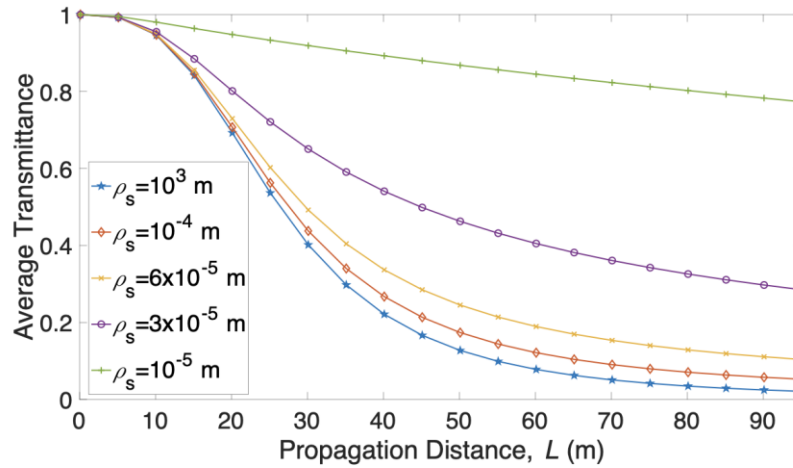


Figure 5 Average transmittance of partially coherent Gaussian beam versus propagation distance L for different partial coherence degrees ρ_s .

As seen in Figure 6, the temperature-induced optical turbulence ($\omega = -5$) has least decrease on the average transmittance. However, the salinity-induced optical turbulence affects the average transmittance significantly, especially at longer distances. Salinity-induced oceanic turbulence increases dramatically in between $\omega = -0.3$ and $\omega = -0.1$. The average transmittance decreases tremendously as seen in Figure 6 if the salinity-induced turbulence is dominant.

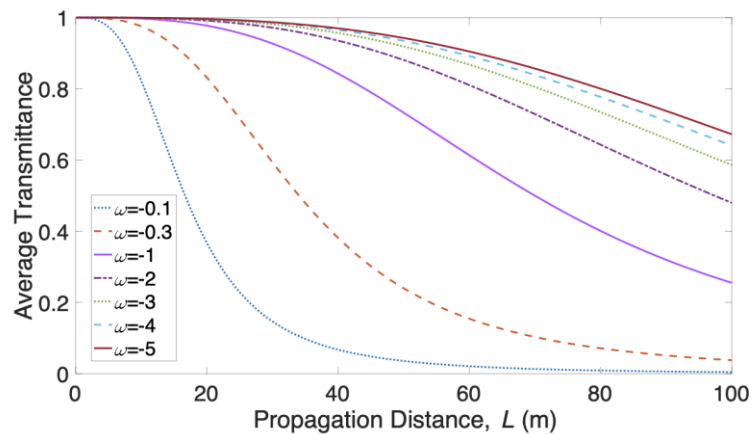


Figure 6 Average transmittance of partially coherent Gaussian beam versus propagation distance L for different ratio of temperature and salinity contributions to the refractive index spectrum ω .

In Figure 7, curves of the average transmittance versus L are plotted for different rate of dissipation of mean square temperature χ_T values in the defined range. With decreasing χ_T , oceanic turbulence effect decreases, so the decrease in the average transmittance becomes smaller.

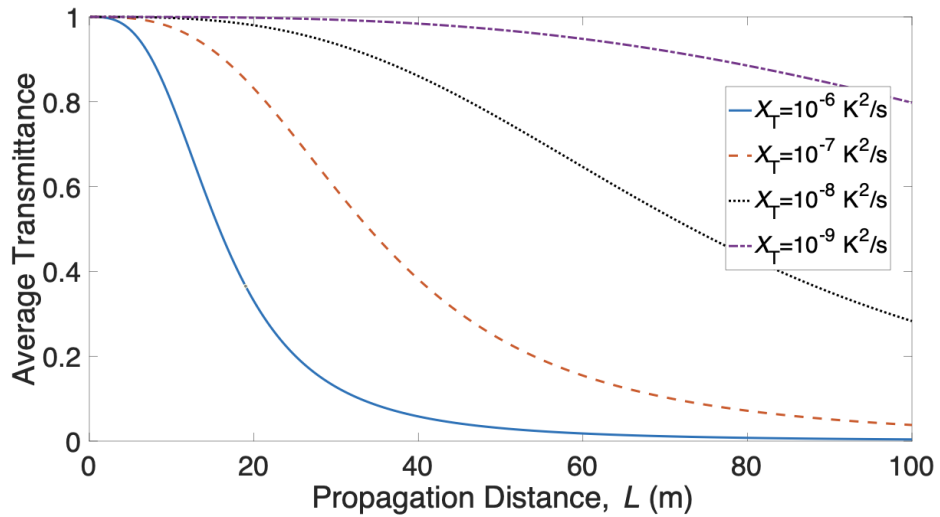


Figure 7 Average transmittance of partially coherent Gaussian beam versus propagation distance L for different rate of dissipation of mean square temperature χ_T .

The graphs of the average transmittance versus propagation distance L are presented in Figure 8 for different values of the rate of dissipation of kinetic energy per unit mass of fluid ε . For high values of ε , the average transmittance slightly decreases. The growth of ε results in a decrease of turbulence associated with the reduction of water motion. For example, when ε takes the biggest value of its range, the corresponding curve goes nearly straight line. When ε is decreased, the average transmittance values decrease more gradually with respect to L .

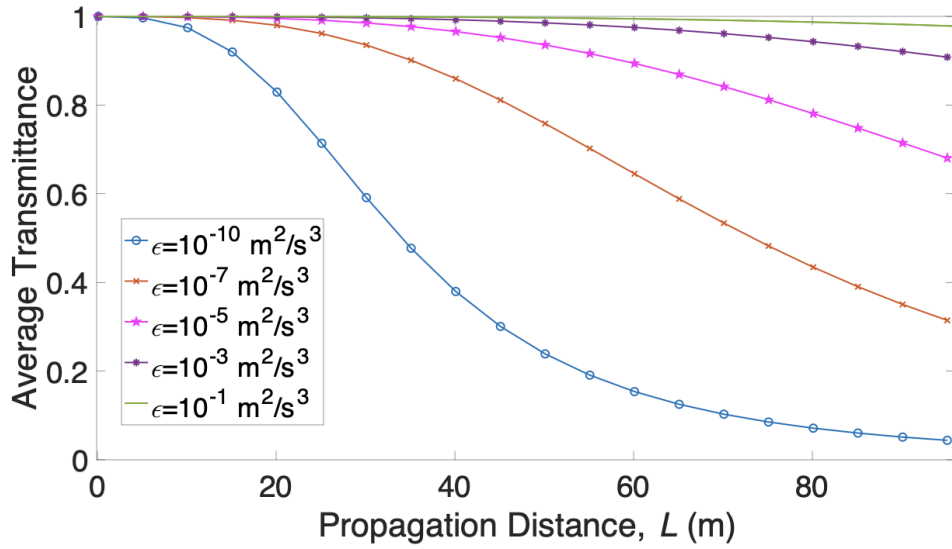


Figure 8 Average transmittance of partially coherent Gaussian beam versus propagation distance L for different rate of dissipation of kinetic energy for unit mass of fluid ϵ .

3.3 Results for Average Transmittance of Partially Coherent Flat-Topped Beam in Underwater Medium

In this part, the on-axis average transmittance for the partially coherent flat-topped beam in a wireless underwater medium is investigated. More specifically, the impacts of the constitutive parameters of oceanic turbulence power spectrum on the on-axis average transmittance for the partially coherent flat-topped beam are studied in this section. The variation of the on-axis average transmittance with respect to the propagation distance L for different oceanic turbulence parameters is shown in Figures 9-14, respectively. The results given in Figures 9-14 are based on our conference paper [207].

As shown in Figure 9, higher average transmittance values can be achieved with larger N values for the flat-topped beam model. A larger N means a flatter beam, and the flatter beam is less affected by underwater turbulence. In contrast, longer link distance results in lower average transmittance values. As expected, the longer propagation distance results in a decrease in transmittance.

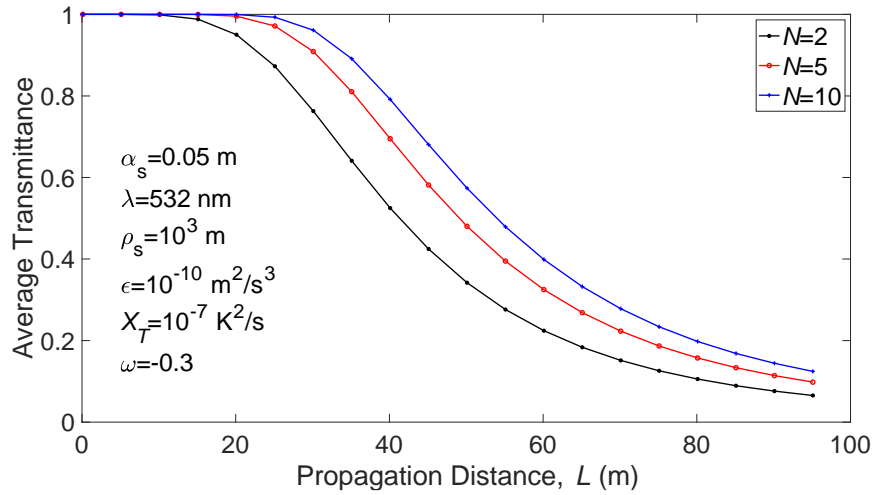


Figure 9 The average transmittance of partially coherent flat-topped beam versus propagation distance L for different various numbers of beams composing the flat-topped beam N .

As shown in Figure 10, the lower degree of coherence yields larger average transmittance, whereas average transmittance decreases with increasing link distances. It should be noted that a linear relationship is observed for a relatively lower ρ_s value of 10^{-5} m. However, increasing the coherence degree ρ_s results in an exponential decrease of the average transmittance with the link distance L .

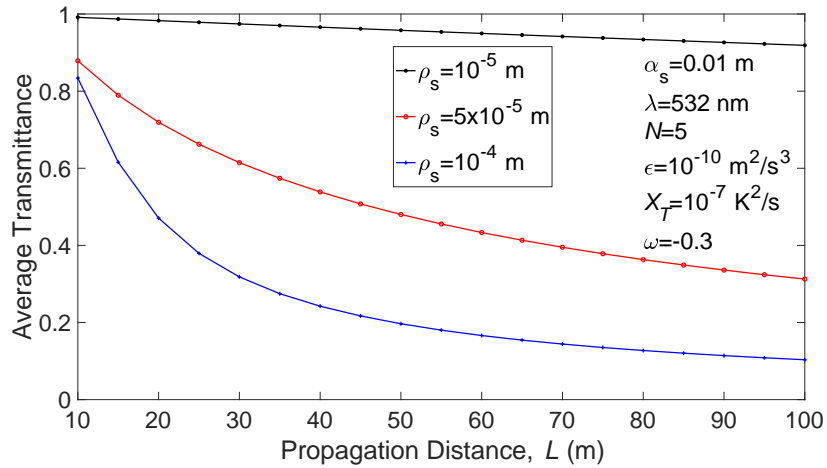


Figure 10 The average transmittance of partially coherent flat-topped beam versus propagation distance L for different partially coherence values ρ_s .

In Figure 11, the higher number of beams composing the flat-topped beam provides larger average transmittance. A small degree of coherence ρ_s gives larger average transmittance value because the beam with reduced coherence degree is less affected by turbulence.

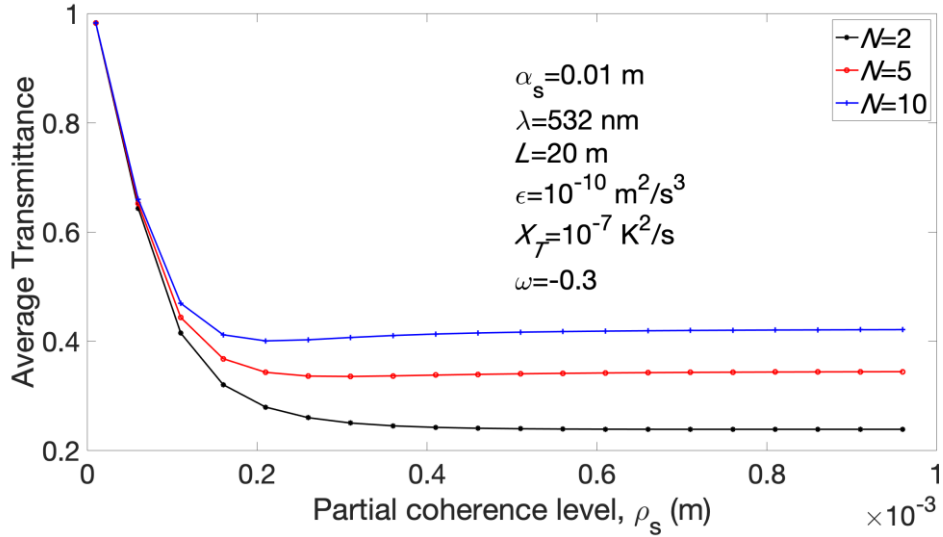


Figure 11 The average transmittance of the partially coherent flat-topped beam versus partial coherence level ρ_s for different numbers of beams composing the flat-topped beam N .

As shown in Figure 12, when the value of the ω is less than -1.5, the average transmittance almost stays the same for any value of other parameters. Therefore, we choose the ω -axis from -1.5 to 0 to observe the results clearly. As can be seen in Figure 12, the temperature-induced optical turbulence has almost no effect on the average transmittance. However, the salinity-induced optical turbulence makes it nearly zero especially in the interval [-0.5, 0]. The salinity induced optical turbulence has more negative effects than the temperature-induced optical turbulence on the average transmittance. Figure 12 also shows that a decrease in the coherence level results in an increase on the average transmittance.

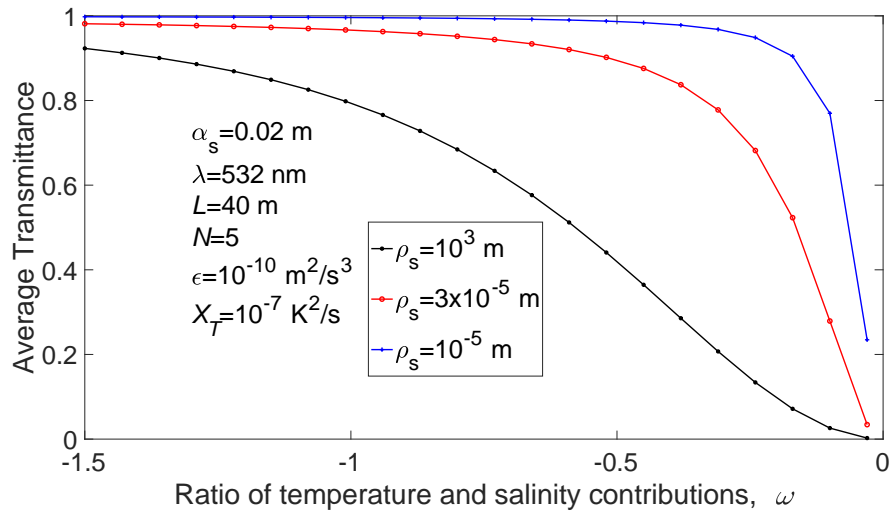


Figure 12 The average transmittance of partially coherent flat-topped beam versus the ratio of temperature and salinity contributions to the refractive index spectrum ω for different partially coherence values ρ_s .

In Figure 13, curves of the average transmittance versus χ_T are plotted against different partial coherent degrees, showing that the average transmittance of a partially coherent flat-topped beam becomes smaller for larger χ_T . Larger χ_T values yield larger temperature differences and this, in turn, causes an increase in turbulence strength. When a source is less coherent, the average transmittance is affected less from an increase on χ_T and so the average transmittance gets higher for decreasing ρ_s .

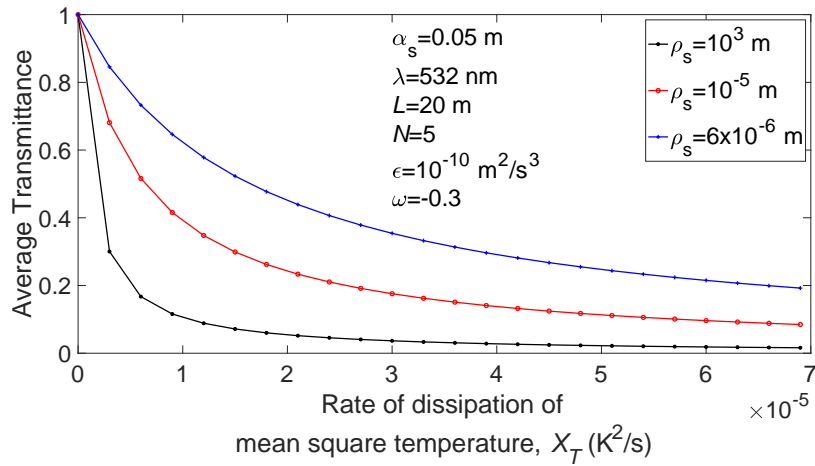


Figure 13 The average transmittance of partially coherent flat-topped beam versus the rate of dissipation of mean square temperature χ_T for different partially coherence values ρ_s .

As can be seen in Figure 14, the average transmittance decreases more in low values of ϵ than the high values of it since decreasing of ϵ means the kinetic energy is high. The turbulence increases in areas where kinetic energy is high and causes a decrease in transmittance. On the other hand, for high values of ϵ , the average transmittance increases for any different partial coherence degrees. When the level of coherence is decreased, the off-axis average transmittance increases.

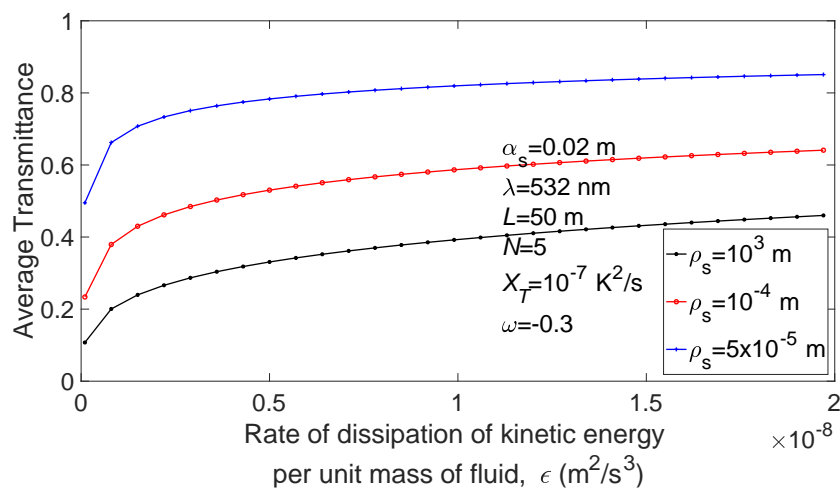


Figure 14 The average transmittance of partially coherent flat-topped beam versus the rate dissipation of kinetic energy per unit mass of fluid ϵ for different partially coherence values ρ_s .

The results also indicate that if the flatness increases, the average transmittance is greater, which means greater N (number of Gaussian beam wave composing the flat-topped beam) gives greater transmittance. Degree of coherency (ρ_s) is inversely proportional to the average transmittance. An increase in the link distance reduces the average transmittance. The loss of the kinetic energy of fluid causes less turbulence. The rate of dissipation of kinetic energy per unit mass of fluid is directly proportional to the average transmittance while the rate of dissipation of the mean-squared temperature is inversely proportional to the average transmittance. When the temperature-induced optical turbulence is dominant, the average transmittance almost never decreases. However, the salinity-induced optical turbulence reduces the average transmittance sharply.

3.4 Results for Off-axis Average Transmittance of Partially Coherent Flat-Topped Beam in Underwater Medium

In this part of the study, the off-axis average transmittance of partially coherent flat-topped beam is examined in turbulent underwater medium. The oceanic turbulence effects on the average transmittance is observed with respect to the parameters ω , χ_T , ε , α_s , N , ρ_s , and r_x . The wavelength is chosen from the blue-green region range which is 532 nm. Kolmogorov microscale length η in all the figures is 1 mm. The other related parameters are shown on the figures. Figures 15-21 demonstrate the results of the off-axis average transmittance for partially coherent flat-topped (PCFT) beams and these figures are based on our paper [61].

Figure 15 shows the effect of turbulent underwater medium on the off-axis average transmittance of the coherent flat-topped beam versus the rate of dissipation of kinetic energy per unit mass of fluid axis for different degrees of flatness. It is found that as the flatness increases (i.e. higher N), larger average transmittance is observed. By our definition of flat-topped beam, flatter beam formulation produces the reduced amplitude and enlarged source size. As seen in Figure 15, the average transmittance increases with increasing N . It means that the oceanic turbulence affects the flatter

beam less. It is noticed from Figures 15 and 16 that when ε reduces, the average transmittance also reduces. The increase on ε means that oceanic turbulence effects are reducing. Figure 16 also indicates that the size of the source affects the average transmittance in turbulent ocean. Larger source size provides larger average transmittance.

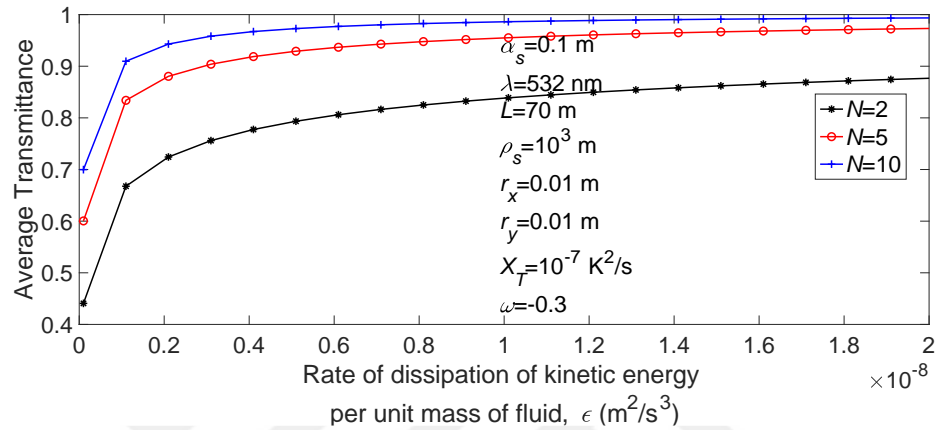


Figure 15 The average transmittance of the partially coherence flat topped beam versus the rate of dissipation of kinetic energy per unit mass of fluid ε for various numbers of beams composing the flat-topped beam N .

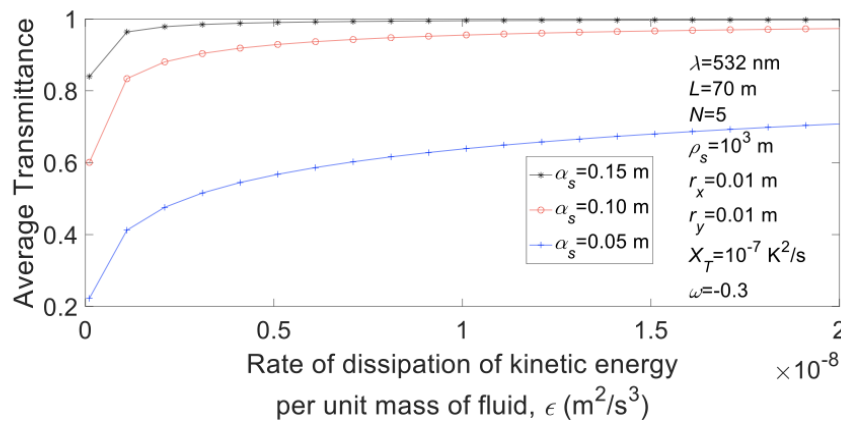


Figure 16 The average transmittance of partially coherence flat-topped beam versus the rate of dissipation of kinetic energy per unit mass of fluid ε for different source size values α_s .

In Figures 17 and 18, the average transmittance is shown against χ_T , for different degrees of flattened N and degrees of source coherence ρ_s . The smaller value of χ_T determines weak oceanic turbulence and the bigger value of χ_T means strong oceanic turbulence. From Figures 17 and 18, it can be understood that when χ_T becomes larger, the average transmittance decreases for all N . Additionally, from Figure 17, it is observed that the average transmittance is higher at larger values of N . This figure also reveals that the average transmittance decreases when the off-axis parameter r_x is becomes larger.

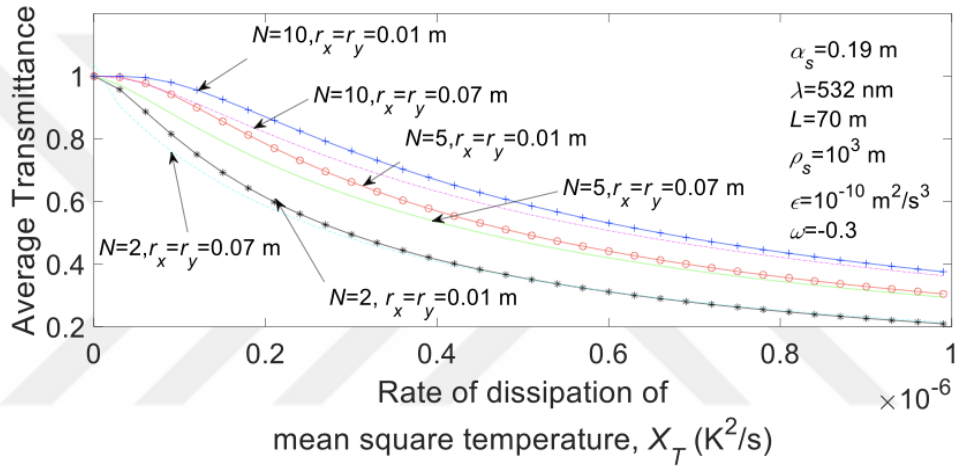


Figure 17 The average transmittance of partially coherent flat topped beam versus the rate of dissipation of mean square temperature χ_T for various numbers of beams composing the flat-topped beam N and off-axis parameter r_x .

In Figure 18, when χ_T is kept fixed, for a smaller degree of ρ_s , the average transmittance is larger. As seen in Figure 18 and 19, if ρ_s is very small, the average transmittance decreases only a little. However, if the ρ_s increases, the average transmittance is getting smaller. In Figure 18, it is understood that when the flat-topped beam becomes more incoherent, the average transmittance rises.

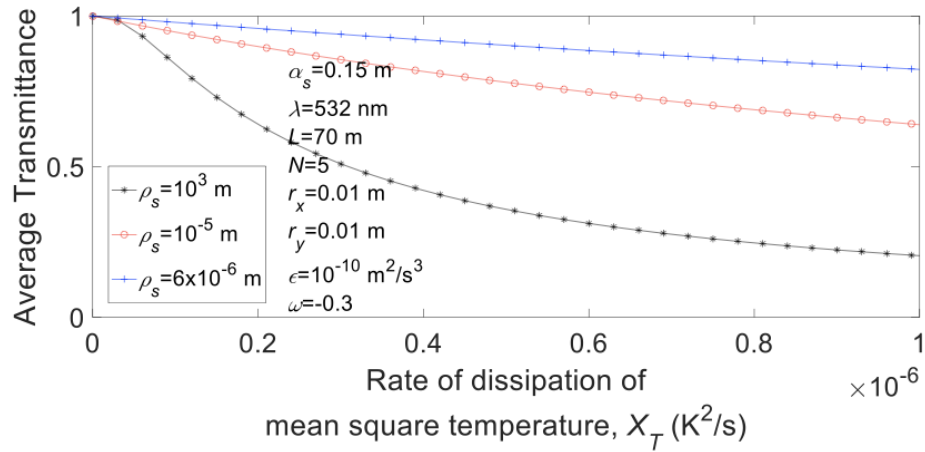


Figure 18 The average transmittance of partially coherent flat-topped beam versus the rate of dissipation of mean square temperature χ_T for various degrees of partial coherence ρ_s .

Figures 19 and 20 shows the variation of the average transmittance against the ratio of salinity and temperature contributions ω . When $\omega = -5$, the temperature-based optical turbulence is effective, for $\omega = 0$ salinity-based optical turbulence is dominant. Temperature-based optical turbulence affects the average transmittance slightly, but the salinity-based optical turbulence reduces the average transmittance to almost zero, especially in the $[-0.5, 0]$ range.

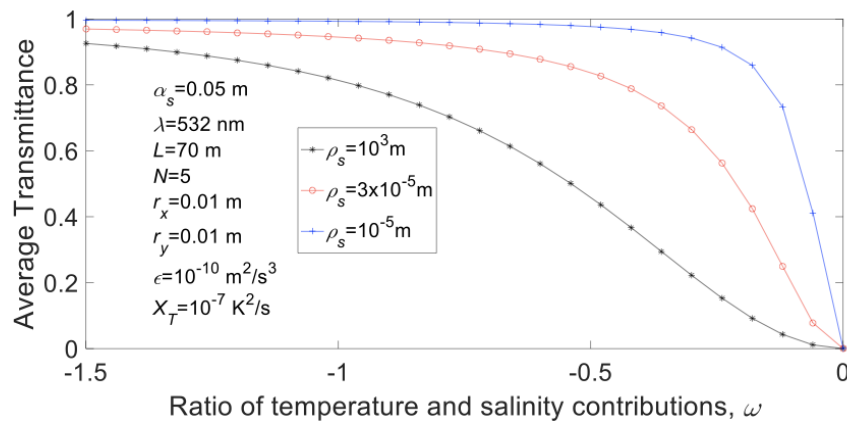


Figure 19 The average transmittance of partially coherent flat-topped beam versus the ratio of temperature and salinity contributions ω for various degrees of partial coherence ρ_s .

From Figure 20, it is seen that when the source size becomes smaller, the average transmittance is reduced more in salinity-based turbulent ocean. Thus, when a small source size is used, a smaller average transmittance is obtained. The beam waves with smaller source size are affected from the turbulence and expands in any medium.

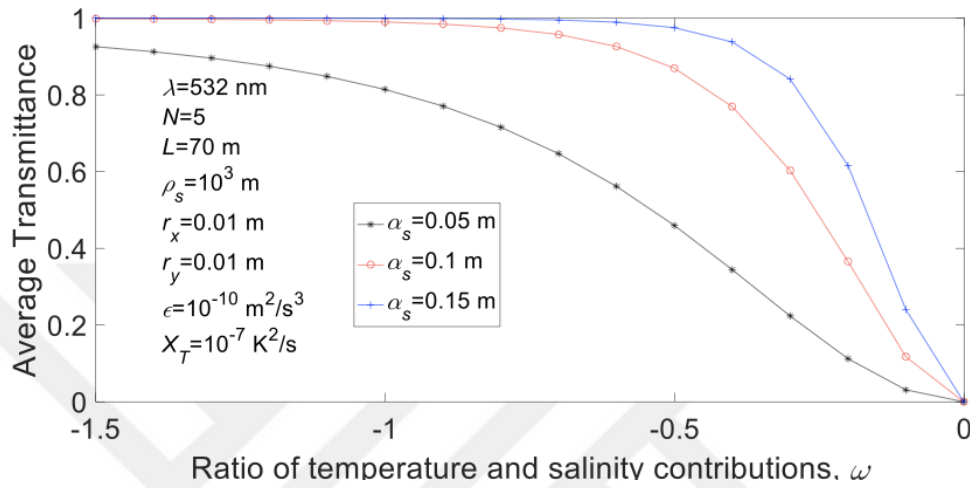


Figure 20 The average transmittance of partially coherent flat-topped beam versus the ratio of temperature and salinity contributions ω for different source sizes α_s .

It can be observed from Figure 21 that the behavior of the average transmittance against the off-axis parameter r_x for different N values. The average transmittance decreases if r_x becomes larger. For the same r_x , bigger N provides higher average transmittance.

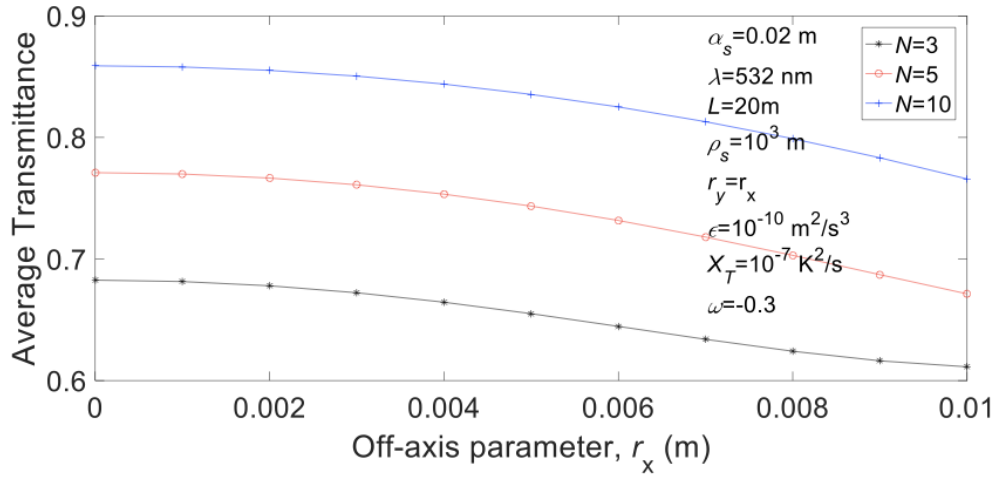


Figure 21 The average transmittance of partially coherent flat-topped beam versus off-axis parameter r_x for various numbers of beams composing the flat-topped beam N .

In Figure 22, it is seen that the average transmittance decreases more at small wavelengths. In Figure 22, all different wavelength curves decrease with increasing propagation distance.

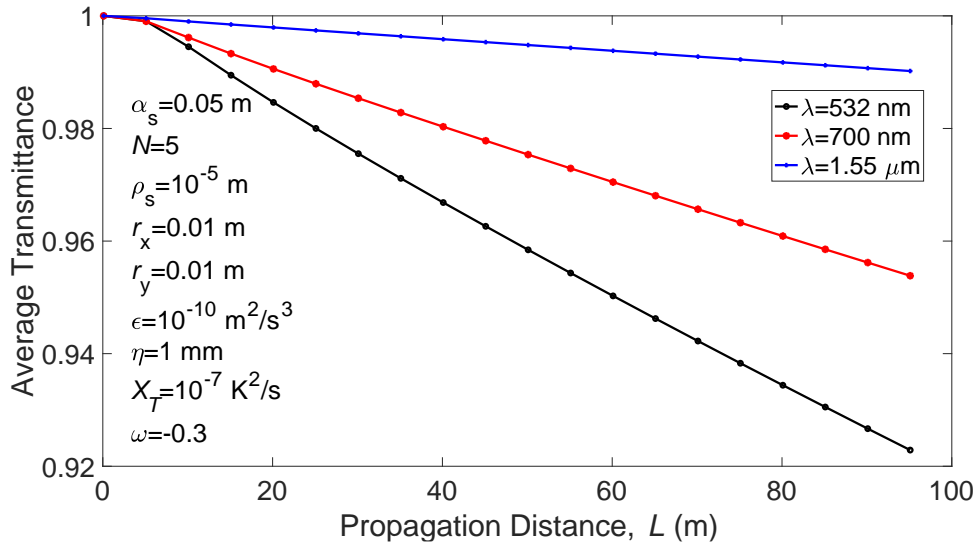


Figure 22 The average transmittance of partially coherent flat-topped beam versus propagation distance L for different wavelength values λ .

3.5 Results for the Average Transmittance of Cosine Gaussian Beam in Underwater Medium

In this section, impacts of turbulent ocean medium on the propagation of on-axis average transmittance of cosine-Gaussian beam is analyzed. The behavior of on-axis average transmittances corresponding to the parameters ω , χ_T , ε , α_s , and V_l is observed. In this part of study, the wavelength is chosen as 532 nm from the blue-green region, because the blue-green region is the least attenuated at the clear ocean water [20,59,61]. Kolmogorov microscale length η is used as 10^{-3} m in all the figures. Other relevant parameters are shown on the figures. Figures 23-28 show the average transmittance of the cos-Gaussian beam in turbulent ocean. These figures are based on our paper [62].

From Figure 23 it can be seen that the effect of the oceanic turbulence on the average transmittance of the cos-Gaussian beam versus the rate of dispersion rate of kinetic energy for different displacement parameters V . It is observed that for any value of ε , as the displacement parameter V decreases, larger average transmittance is observed. Figure 23 also demonstrates that with an increase in ε , average transmittance increases. Increasing the dispersion rate of kinetic energy causes the strength of the oceanic turbulence to decrease. Since less kinetic energy causes the turbulent motion to decrease. Weaker turbulence provides larger average transmittance.

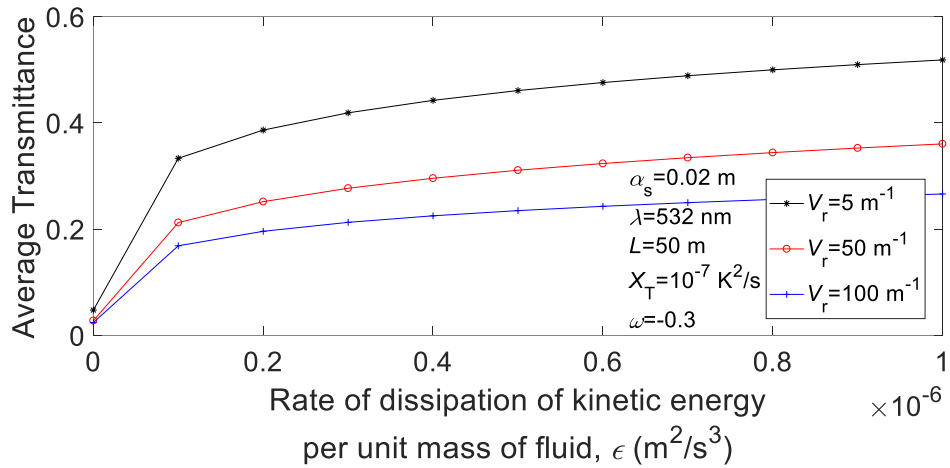


Figure 23 Average transmittance of cos-Gaussian beam versus the rate of dissipation of kinetic energy per unit mass of fluid ϵ for different displacement parameters V .

Figure 24 shows that when the rate of dissipation of kinetic energy per unit mass of fluid ϵ increases, the average transmittance also increases since decreasing ϵ means strong oceanic turbulence. Figure 24 also indicates that for any value of ϵ , larger average transmittance is obtained with larger source size.

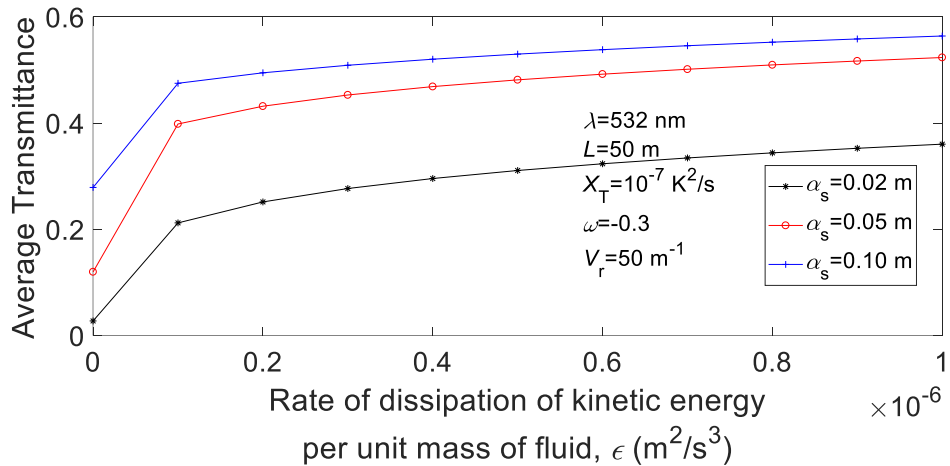


Figure 24 Average transmittance of cos-Gaussian beam versus the rate of dissipation of kinetic energy per unit mass of fluid ϵ for different source size α_s values.

Figures 25 and 26 show the variations of the average transmittance versus the ratio of salinity and temperature contributions ω . Salt dissolved in seawater is quantified as the salinity. Increasing salinity means there are many salt ions in that area. That causes salinity-based oceanic turbulence is dominating. Salinity-based turbulence affects the average transmittance considerably. If the heat and temperature increases, dissolved salt decreases so temperature-based oceanic turbulence is effective. Salinity-based turbulence reduces slightly and affects hardly the transmittance. ω axis is observed in the range $[-1.5, 0]$ in Figures 25 and 26 since, this is the most effective range of ω (salinity induced turbulence effect). Figure 25 exhibits that at any value of ω , as V becomes larger, the average transmittance becomes smaller. In Figure 26, the observation is that while source size is getting smaller, the average transmittance is affected more negatively from the salinity-based optical turbulence.

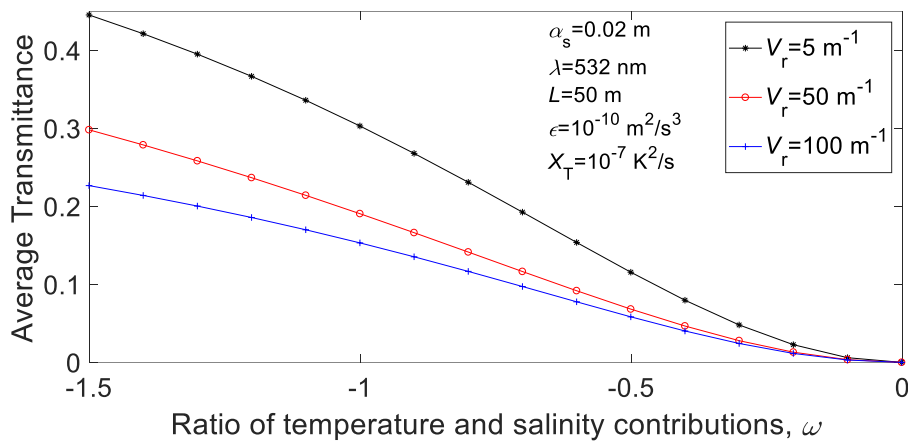


Figure 25 Average transmittance of cos-Gaussian beam versus the ratio of temperature and salinity contributions ω for different displacement parameter V .

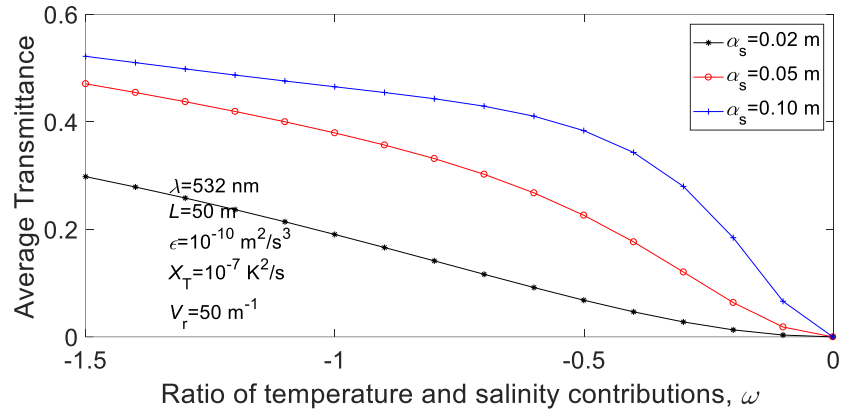


Figure 26 Average transmittance of cos-Gaussian beam versus the ratio of temperature and salinity contributions ω for different source size α_s .

In Figures 27 and 28, the average transmittance is shown with respect to the rate of dissipation of mean-square temperature χ_T , for different displacement parameter V and source size α_s . From Figures 27 and 28, it can be seen that if V is kept fixed, with increasing χ_T , the on-axis transmittance decreases. In Figure 27, when the displacement parameter V_r becomes larger, the average transmittance becomes smaller. In Figure 28, when χ_T is kept fixed, the average transmittance is smaller for a smaller value of source size.

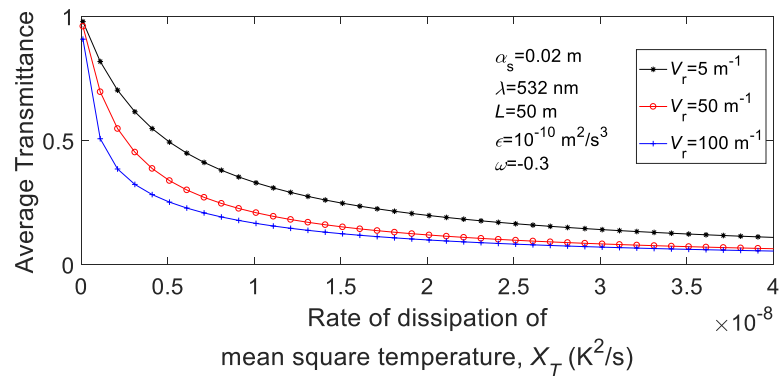


Figure 27 Average transmittance of cos-Gaussian beam versus the rate of dissipation of mean square temperature χ_T for different displacement parameter V .

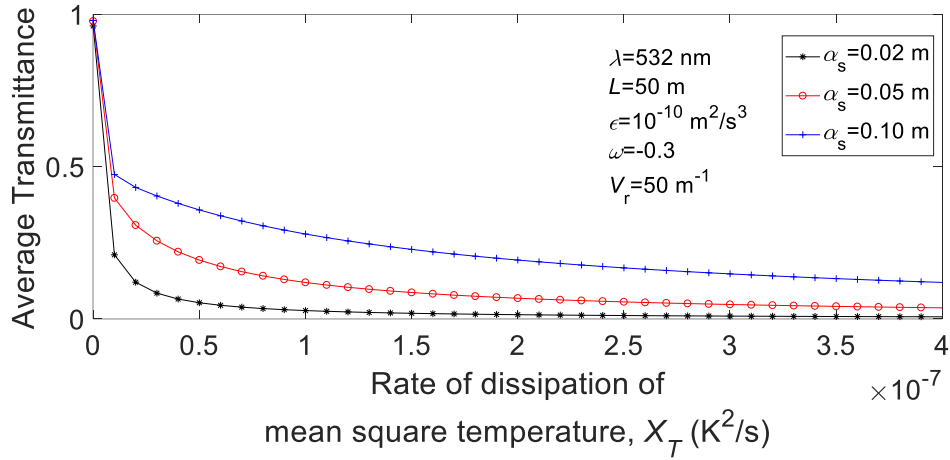


Figure 28 Average transmittance of cos-Gaussian beam versus the rate of dissipation of mean square temperature χ_T for different source size α_s .

It is not possible to directly support the results with the studies existing in literature. This study has been brought to the literature by our works. However, the studies for atmospheric turbulence is used to understand the accuracy of it. In addition, it is observed that there are similar trends with cos-Gauss intensity, which are in [56].

3.6 Results for Off-axis Average Transmittance of Partially Coherent Cosine Gaussian Beam in Underwater Medium

Note that the off-axis average transmittance in underwater for the partially coherent cosine-Gaussian beam is presented in Figures 29-31, respectively, based on our study [191]. In this section, the mentioned transmittance expression represents the off-axis average transmittance. The results were analyzed with respect to ϵ , χ_T , and ω . Furthermore, r and ρ_s parameters and the effect of the partial coherence are used to examine the effect of oceanic turbulence on the off-axis average transmittance. In addition, observations were made by using different V values to examine the effect of the displacement parameter that is used to create the cosine and hyperbolic cosine Gaussian beams. The values of the parameters used in each figure are specified on

the figures. Kolmogorov microscale η is the same for all analyses with a value of 1 mm.

In Figure 29, the off-axis average transmittance of partially coherent cosine Gaussian beam is examined in a way that corresponds to the dispersion rate in kinetic energy, simultaneously. Figure 29 also shows the effect of the distance of the receiver moving away from the center, i.e. off-axis parameter r is not equal to zero. As can be seen from Figure 29, with increasing dissipation rate in kinetic energy also reduces turbulence whereas the average transmittance increases. The average transmittance of the partially coherent cosine increases as the receiver moves away from the center because of the beam shape of the cos-Gaussian and position of the receiver.

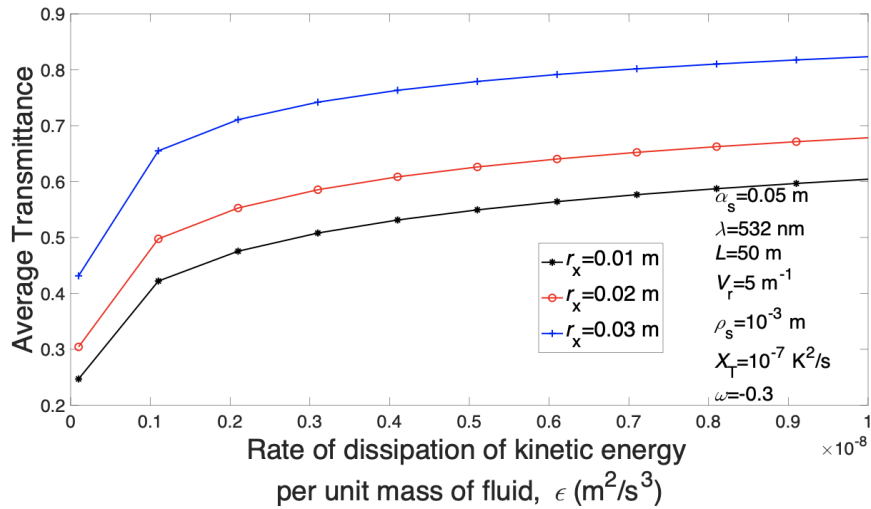


Figure 29 Off-axis average transmittance of partially coherent cos-Gaussian beam versus ϵ , for different off-axis parameters

$$r_x.$$

In Figure 30, another oceanic turbulence parameter that is dissipation rate of the mean square temperature is examined according to the average transmittance of the cos-Gaussian beam. It is observed that more differences in the temperature field result in more turbulence and therefore, the average transmittance decreases accordingly. The increase of V_r , which indicates the displacement parameters of the

cosine-Gaussian light beam, causes a decrease in the average transmittance for the cosine-Gaussian beam.

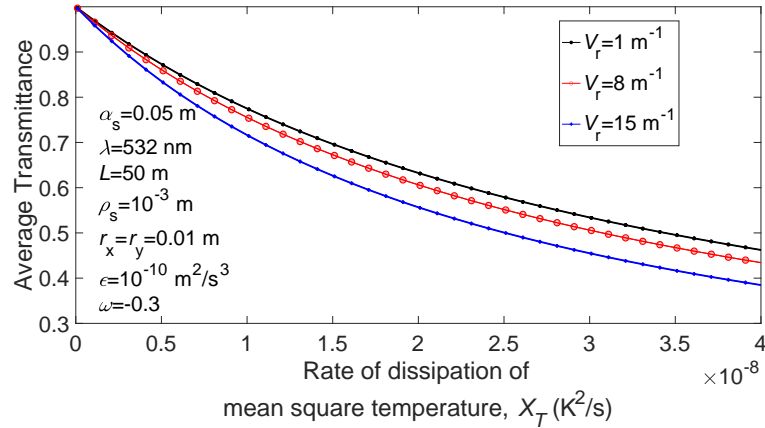


Figure 30 Off-axis average transmittance of partially coherent cos-Gaussian beam versus χ_T , for different displacement parameters V_r .

When examining the ω effect in Figure 31, it was observed that temperature-based turbulence did not have a great effect on the average transmittance and the transmittance remained almost the same. As ω value approaches 0, the salinity-based optical turbulence becomes important and it causes a significant decrease in the average transmittance. With its maximum, the optical transmittance is completely lost. Again, we can observe the partial coherence effect for the cosine-Gaussian beam over the same figure of 31; the average transmittance appears to increase as the degree of coherence of the cosine-Gaussian beam decreases. It was observed that the partially coherence case of Cos-Gaussian beam has been less affected by turbulence.

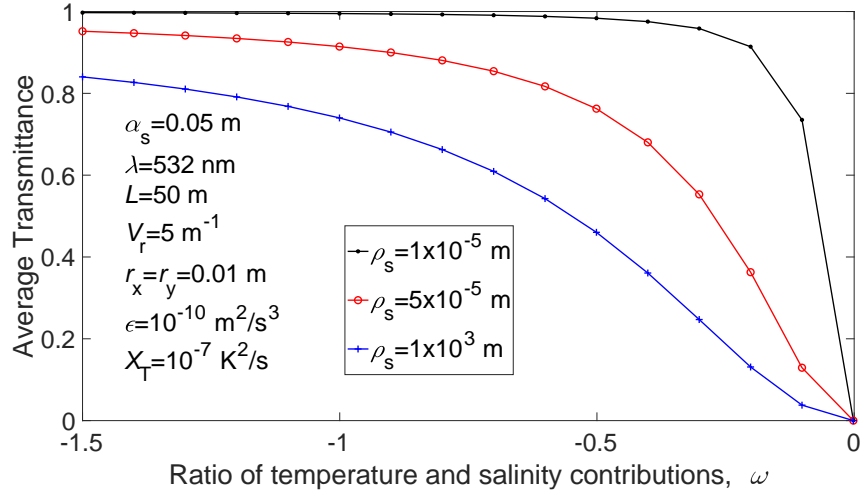


Figure 31 Off-axis average transmittance of partially coherent cos-Gaussian versus ω , for various degrees of partially coherence ρ_s .

3.7 Results for the Average Transmittance of Cosine Hyperbolic Gaussian Beam in Underwater Medium

In this part of this study, influence of turbulent ocean on the average transmittance is examined when the cosine hyperbolic Gaussian beam propagates in an oceanic turbulent medium. The trends of the average transmittances are observed against the parameters ω , χ_T , ε , α_s and V_i . The wavelength was chosen as 532 nm. Kolmogorov microscale length η is taken to be 1 mm in all the figures. Other relevant parameters are shown on the figures. Given results are based in our paper [62].

In Figure 32, the average transmittance is observed with respect to the rate of dissipation of mean square temperature ε for different displacement parameter V values. With increase in ε , the average transmittance increases, which is true for any V_i value. For the same ε , larger V_i gives larger average transmittance.

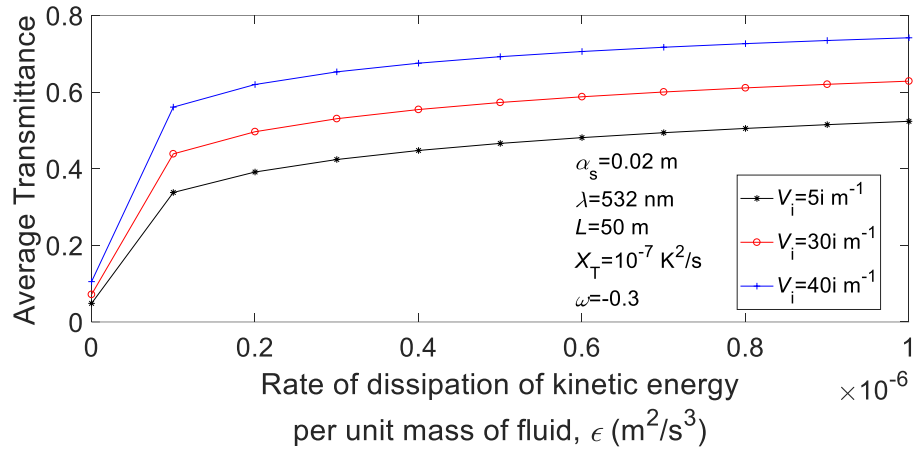


Figure 32 Average transmittance of cosh-Gaussian beam versus the rate of dissipation of kinetic energy per unit mass of fluid ϵ for different displacement parameters V .

Figure 33 shows that larger ϵ yields larger average transmittance for any value of source size, which can be explained physically that larger ϵ results in less motion in underwater, which means less turbulence strength. At the same ϵ , larger α_s causes the average transmittance to reduce.

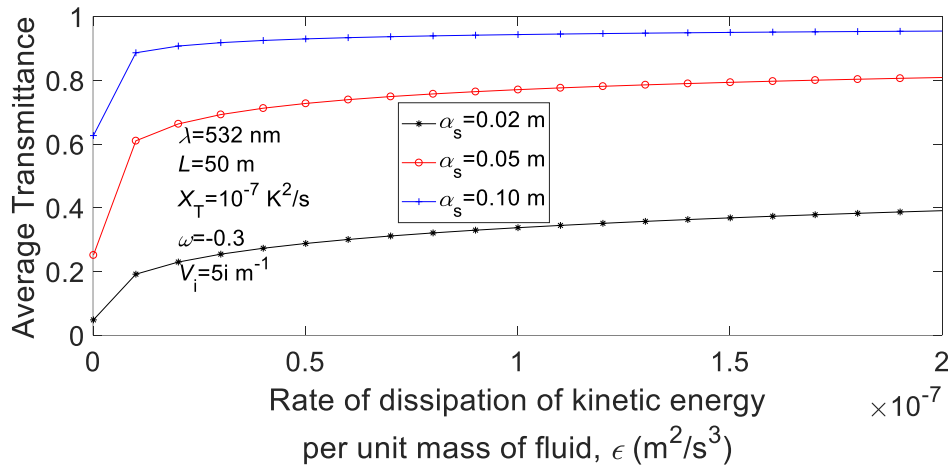


Figure 33 Average transmittance of cosh-Gaussian beam versus the rate of dissipation of kinetic energy per unit mass of fluid ϵ for different source size, α_s values.

Figures 34 and 35 are provided to observe the variations of the average transmittance versus the ratio of temperature and salinity contributions ω for different values of V_i and α_s values, respectively. When ω determines the salinity-based optical turbulence, oceanic turbulence effect increases and the average transmittance decreases for all V_i and α_s values. As seen in Figure 34, at fixed ω , it is seen that bigger V_i provides larger average transmittance for the cosh-Gaussian beam. In Figure 35, at fixed ω , larger α_s makes the average transmittance at the receiver plane to become larger.

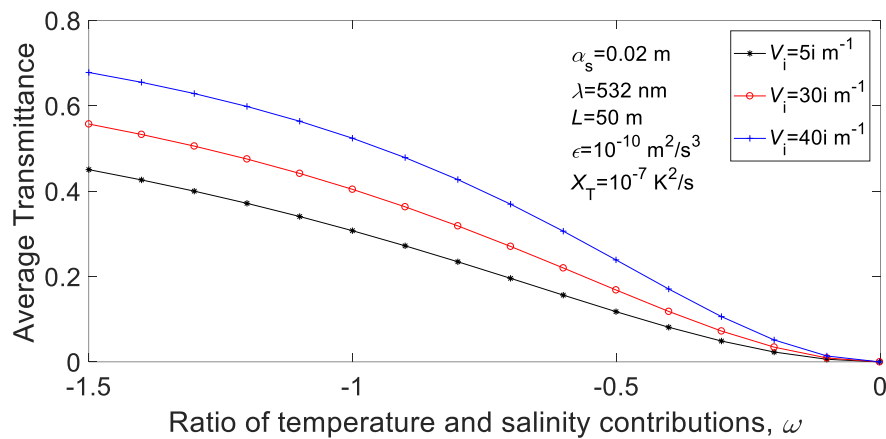


Figure 34 Average transmittance of cosh-Gaussian beam versus the ratio of temperature and salinity contributions ω for different displacement parameter V .

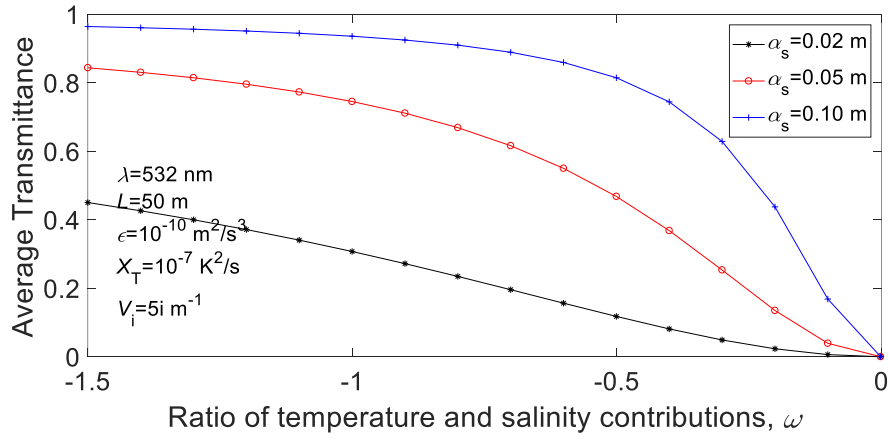


Figure 35 Average transmittance of cosh-Gaussian beam versus the ratio of temperature and salinity contributions ω for different source size α_s .

As seen in Figures 36 and 37, the average transmittance decreases along the χ_T axis. This is owing to the physical fact that for larger χ_T , the power of turbulence gets higher. In Figure 36, for the smaller displacement parameter V_i , larger average transmittance is obtained. From Figure 37, it is seen that the impact of turbulence increases with increasing χ_T , which is valid for all α_s . Moreover, if χ_T is kept fixed, the average transmittance is less for small values of α_s . It can be said that the cosh-Gaussian beam which has a larger source size is less affected in the oceanic turbulence.

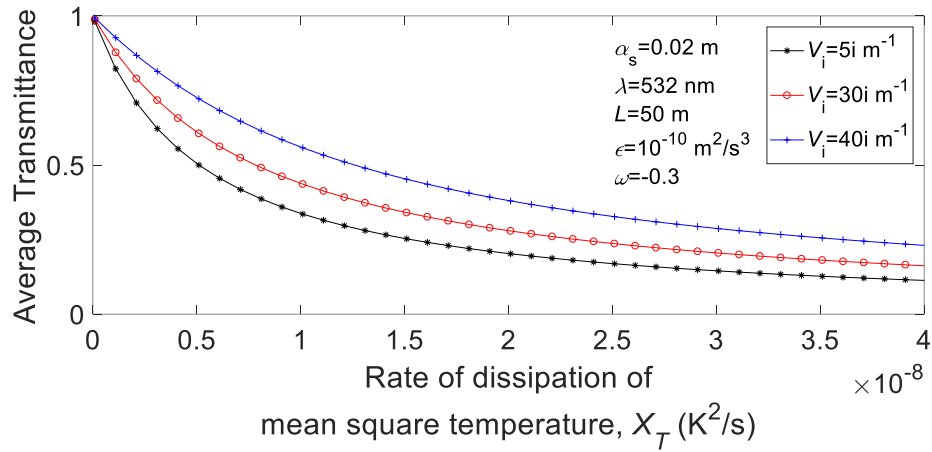


Figure 36 Average transmittance of cosh-Gaussian beam versus the rate of dissipation of mean square temperature χ_T for different displacement parameters V .

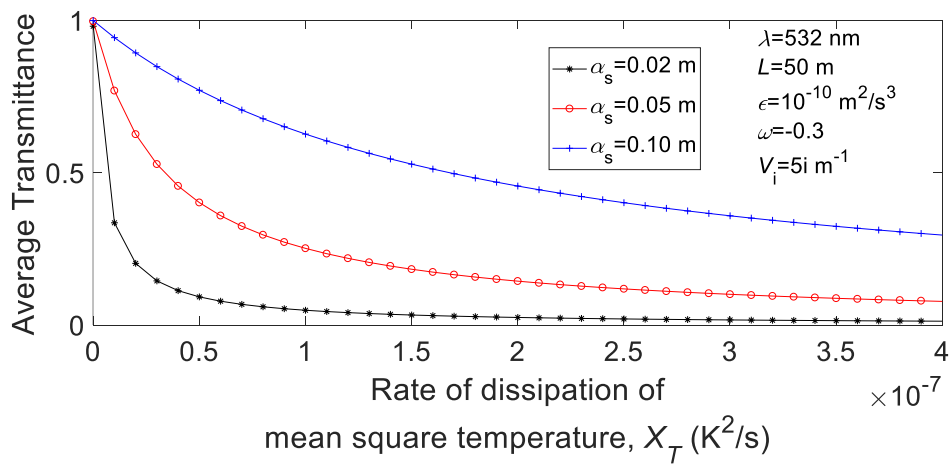


Figure 37 Average transmittance of cosh-Gaussian beam versus the rate of dissipation of mean square temperature χ_T for different source sizes α_s .

3.8 Results for Off-axis Average Transmittance of Partially Coherent Cosine Hyperbolic Gaussian Beam in Underwater Medium

Similar to the cosine-Gaussian beam investigations, hyperbolic cosine-Gaussian beam analysis is also carried out. These results are from our accepted paper [191]. As

shown in Figure 38, similar to the cosine-Gaussian one, the average transmittance increases with the increase of ϵ and the distance of the receiver from the axis center.

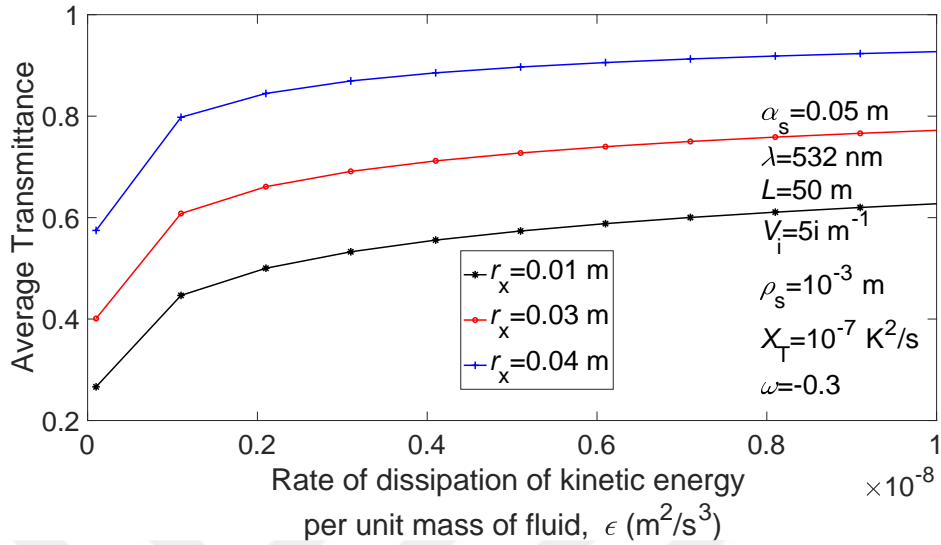


Figure 38 Off-axis average transmittance of partially coherent cosh-Gaussian versus ϵ , for different off-axis parameters r_x .

Figure 39 shows that the turbulence effect increases and the average transmittance decreases with the increase in χ_T , as in the case for the cosine Gaussian. However, for this case, unlike the cosine Gaussian, as the displacement parameter of the hyperbolic cosine-Gaussian beam increases, the average transmittance increases. This result is supported by Ref [57]. Since the beam propagation shows similar properties in atmospheric turbulence and underwater turbulence. Therefore, we can compare the similarity of both environments by analyzing the investigations conducted in the atmosphere although we cannot make a one-to-one comparison. It should be noted that the cosh-Gaussian beam has not been studied previously in the underwater environment.

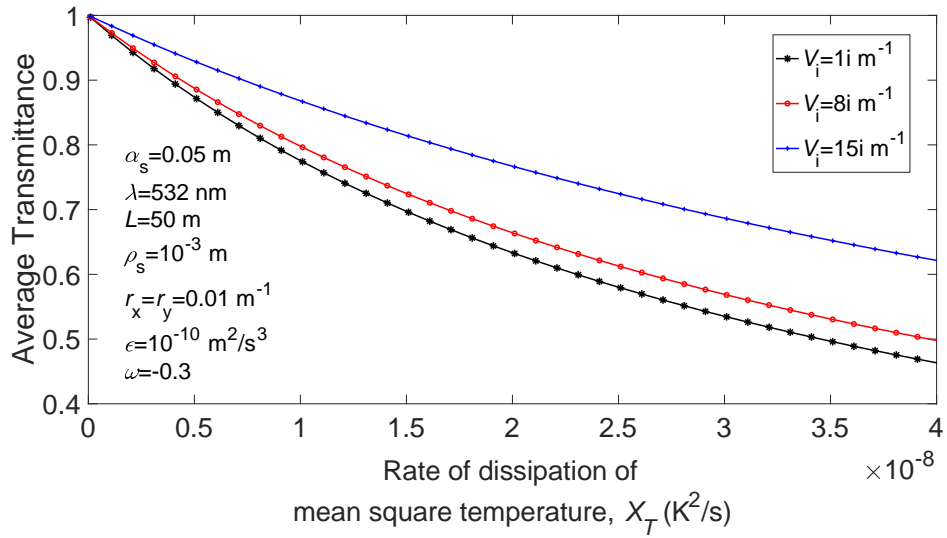


Figure 39 Off-axis average transmittance of partially coherent cosh-Gaussian versus χ_T , for different displacement parameters.

In Figure 40, salinity-based optical turbulence and partially coherence effects are observed. While temperature-based turbulence hardly changes the transmittance, salinity-based turbulence causes a deep reduction in the average transmittance. The partial coherence effect is also similar to that of the cosine_Gaussian and as the degree of coherence decreases, the off-axis average transmittance increases.

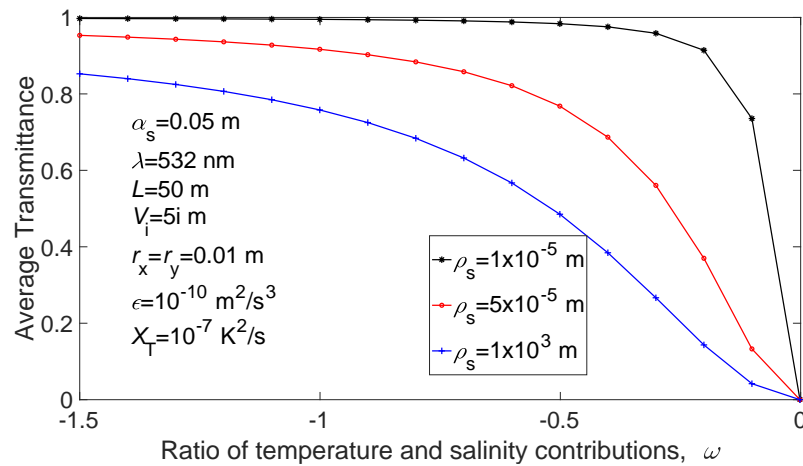


Figure 40 Off-axis average transmittance of partially coherent cosh-Gaussian versus ω , for various degrees of partially coherence ρ_s .

3.9 Conclusion

In this chapter, the average transmittance for different beam types in underwater turbulent conditions is studied extensively. The effect of each oceanic turbulence parameter on all the beams is found to be similar. That is, an increase in χ_T and ω values, which cause an increase in turbulence strength, yields a decrease in the average transmittance for all beams. On the other hand, increasing ω and/or χ_T , strength of oceanic turbulence is increasing [37,167]. In strong turbulence conditions, the average transmittance decreases [65]. Increasing oceanic turbulence effects cause the average transmittance to decrease, which is also supported by Refs. [65]. As opposed to χ_T and ω , it was observed that with increasing ε , the average transmittance increases for all beam types. Increase in ε values results in a decrease in mobility and kinetic energy in water and thus a decrease in turbulence. As expected, the average transmittance decreases with increasing propagation distance L . Numerical simulations also showed that an increase in the beam source size increases the average transmittance in all the conditions we have examined. When we observe the N parameter for the flat-topped beam, as the number of Gaussians forming the flat-topped beam increases, that is, the flatness degree of the beam increases, the average transmittance also increases. This result is supported by the references [85,86]. When the average transmittance of the flat-topped beam was examined for atmospheric turbulence, it was observed that as the level of flatness increased, it was less affected by turbulence [167].

When we use a partially coherence source for the flat-topped, cos-Gaussian, and cosh-Gaussian beam, the increase in ρ_s (i.e. the more coherent beam) decreases the transmittance. Once again, when the off-axis average transmittance is studied for the flat-topped, cos-Gaussian, and cosh-Gaussian beams, the transmittance increases with the increase of the off-axis variable r_x for the cos and cosh-Gaussian beams, while the transmittance decreases for the flat-topped beam owing to the sources shape. Lastly, while the transmittance of the cosine-Gaussian beam decreases with the increase of the displacement parameter V_r forming the cosine beam, the

transmittance of the cosh-Gaussian beam increases with the increase of V_i (i.e. the corresponding counterpart of V_r in cosine hyperbolic).

As a result, when we compare the transmittance with respect to link distance for all beam types we examined under the same conditions, we can see that coherent beams have lower transmittance than partially coherent beams. However, as we can observe from Figure 41, the flat-topped beam has the highest average transmittance compared to other beams for all conditions we examined (parameters and values are indicated on the figure). The lowest average transmittance is seen for cos-Gaussian beam of coherent beams. While the coherent flat-topped beam has the highest average transmittance in the short distance, a faster decrease in the average transmittance has been observed, as the distance gets larger. The reason might be that the coherent flat-topped beam turns into a Gaussian beam more quickly than the other beams. When we compare Figure 37 and Figure 38, it is observed that the hyperbolic cosine-Gaussian beam has a greater average transmittance than the cosine-Gaussian beam. Figure 42 shows the off-axis transmittance investigations of all beams examined in Figure 41. Although the two figures seem to be the same, the off-axis average transmittances are lower than the on-axis ones. All beams exhibited the similar characteristics in both figures. This study will provide an opportunity to choose the appropriate beam type for the environment.

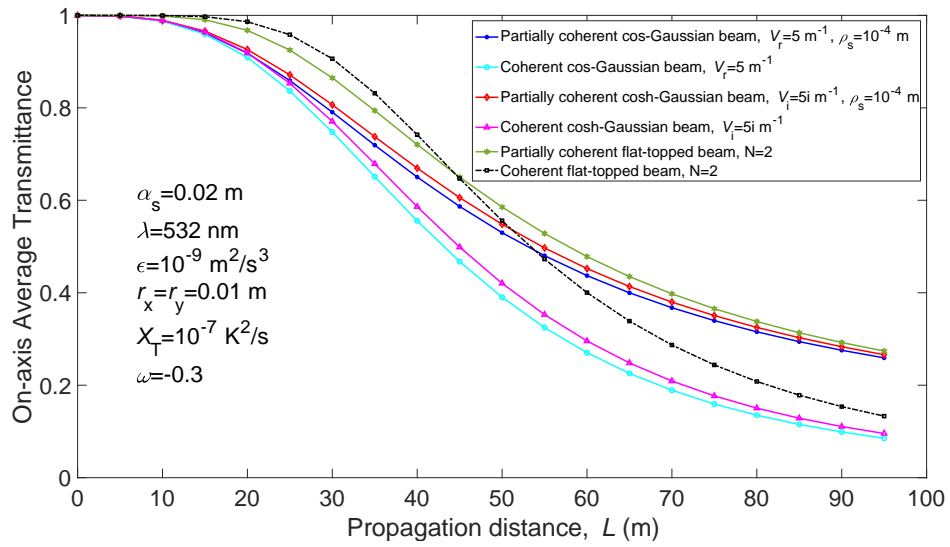


Figure 41 On-axis average transmittance versus propagation distance L , for different beam types.

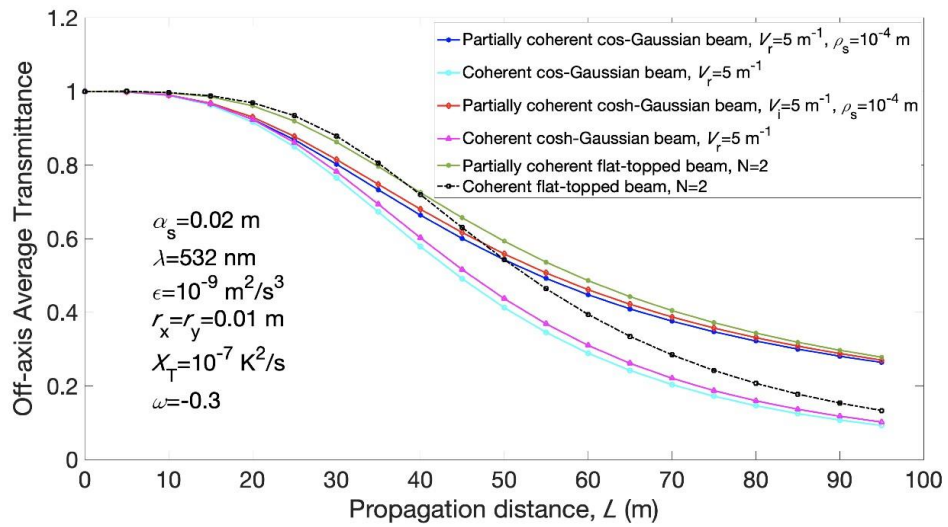


Figure 42 Off-axis average transmittance versus propagation distance L , for different beam types.

CHAPTER 4

BEAM SPREAD

4.1 Methodology for Beam Spread of Partially Coherent Flat-Topped Beam in Underwater Medium

This section started with Carter's definition that helps to define the effective beam spot. Partially coherent multiple Gaussian beams such as the flat-topped is applied in the formulation. Then, the beam size is calculated for partially coherent flat-topped (PCFT) beam. Beam spread formulation for the receiver plane is then applied to obtain only the turbulence effect. Derivation results are valid by comparison in [208].

The effective beam spot can be defined based on Carter's definition as [201],

$$\sigma_x = \sqrt{\frac{2 \int_{-\infty}^{\infty} \int_{-\infty}^{\infty} r_x^2 \langle I(r_x, r_y, L) \rangle dr_x dr_y}{\int_{-\infty}^{\infty} \int_{-\infty}^{\infty} \langle I(r_x, r_y, L) \rangle dr_x dr_y}}, \quad (4.1)$$

where $\langle I(r_x, r_y, L) \rangle$ is the average intensity and r_x and r_y is the transverse coordinate at the receiver plane. If we change the variable to solve in two parts

$$\sigma_x = \sqrt{\frac{2 \int_{-\infty}^{\infty} \int_{-\infty}^{\infty} r_x^2 \langle I(r_x, r_y, L) \rangle dr_x dr_y}{\int_{-\infty}^{\infty} \int_{-\infty}^{\infty} \langle I(r_x, r_y, L) \rangle dr_x dr_y}} = \sqrt{\frac{X}{Y}}, \quad (4.2)$$

$$X = 2 \int_{-\infty}^{\infty} \int_{-\infty}^{\infty} r_x^2 \langle I(r_x, r_y, L) \rangle dr_x dr_y. \quad (4.3)$$

The average intensity calculation for flat-topped beam in Chapter 2, Section 2.4.2 can be used in this part.

$$\begin{aligned} X = & 2 \int_{-\infty}^{\infty} \int_{-\infty}^{\infty} r_x^2 dr_x dr_y \left(\frac{\pi}{\lambda L} \right)^2 \sum_{l_1=1}^N \sum_{l_2=1}^N \frac{A_{l_1} A_{l_2}^*}{-C^2 + BA} \\ & \times \exp \left\{ \left[\left(\frac{k}{L} r_x \right)^2 + \left(\frac{k}{L} r_y \right)^2 \right] / (-4A) \right\} \\ & \times \exp \left[\frac{\left(-i \frac{k}{L} r_x C + iA \frac{k}{L} r_x \right)^2 + \left(-i \frac{k}{L} r_y C + iA \frac{k}{L} r_y \right)^2}{4A(-C^2 + BA)} \right], \end{aligned} \quad (4.4)$$

where $A = \frac{1}{2\alpha_{sl_1}^2} - \frac{ik}{2L} + \frac{1}{\rho_{0_oc}^2} + \frac{1}{4\rho_s^2}$, $B = \frac{1}{2\alpha_{sl_2}^2} + \frac{ik}{2L} + \frac{1}{\rho_{0_oc}^2} + \frac{1}{4\rho_s^2}$, and $C = \frac{1}{\rho_{0_oc}^2} + \frac{1}{4\rho_s^2}$. If we change the variable to sum up the equation, we obtain

$$X = 2 \int_{-\infty}^{\infty} \int_{-\infty}^{\infty} \left(\frac{\pi}{\lambda L} \right)^2 \sum_{l_1=1}^N \sum_{l_2=1}^N A_{l_1} A_{l_2}^* \frac{r_x^2}{x_1} \exp \left[\frac{-\frac{k^2}{4L^2} (r_x^2 + r_y^2)}{z_1} \frac{y_1}{x_1} \right] dr_x dr_y, \quad (4.5)$$

where $x_1 = -C^2 + BA$, $y_1 = 1 + (C - A)^2 / x_1$, $z_1 = A$. Our flat-topped beam intensity can be written with new notation

$$\langle I(r_x, r_y, L) \rangle = \left(\frac{\pi}{\lambda L} \right)^2 \sum_{l_1=1}^N \sum_{l_2=1}^N A_{l_1} A_{l_2}^* \frac{1}{x_1} \exp \left[\frac{-\frac{k^2}{4L^2} (r_x^2 + r_y^2)}{z_1} \frac{y_1}{x_1} \right]. \quad (4.6)$$

Then if we choose $t_1 = \frac{k^2}{4L^2} y_1 / z_1 x_1$, our equation can be written as

$$X = 2 \left(\frac{\pi}{\lambda L} \right)^2 \sum_{l_1=1}^N \sum_{l_2=1}^N A_{l_1} A_{l_2}^* \frac{1}{x_1} \int_{-\infty}^{\infty} \exp(-r_y^2 t_1) \int_{-\infty}^{\infty} r_x^2 \exp(-r_x^2 t_1) dr_x dr_y. \quad (4.7)$$

If we calculate the integration parts gradually, first integral part of Eq. (4.7) is

$$\int_{-\infty}^{\infty} r_x^2 \exp(-t_1 r_x^2) dr_x. \quad (4.8)$$

To solve Eq. (4.8) we use Eq. (2.61) from Ryzhik [49] and obtain

$$\begin{aligned} \int_{-\infty}^{\infty} x^2 \exp(-\mu x^2 + 2vx) dx &= \frac{1}{2\mu} \sqrt{\frac{\pi}{\mu}} \left(1 + 2 \frac{v^2}{\mu} \right) \exp\left(\frac{v^2}{\mu}\right), \\ v = 0 &\Rightarrow \int_{-\infty}^{\infty} x^2 \exp(-\mu x^2) dx = \frac{1}{2\mu} \sqrt{\frac{\pi}{\mu}}, \\ \int_{-\infty}^{\infty} r_x^2 \exp(-t_1 r_x^2) dr_x &= \frac{1}{2t_1} \sqrt{\frac{\pi}{t_1}}. \end{aligned} \quad (4.9)$$

Our equation converts to

$$X = 2 \left(\frac{\pi}{\lambda L} \right)^2 \sum_{l_1=1}^N \sum_{l_2=1}^N A_{l_1} A_{l_2}^* \frac{1}{x_1} \int_{-\infty}^{\infty} \exp(-r_y^2 t_1) \frac{1}{2t_1} \sqrt{\frac{\pi}{t_1}} dr_y. \quad (4.10)$$

If $p^2 = a$ is taken in Eq. (2.20) which converts to

$$\begin{aligned} \int_{-\infty}^{\infty} \exp(-ax^2 \pm qx) dx &= \exp\left(\frac{q^2}{4a}\right) \frac{\sqrt{\pi}}{\sqrt{a}}, \\ q = 0 &\Rightarrow \int_{-\infty}^{\infty} \exp(-ax^2) dx = \sqrt{\frac{\pi}{a}}, \end{aligned} \quad (4.11)$$

then with the help of Eq. (4.11), we obtain

$$X = \left(\frac{\pi}{\lambda L} \right)^2 \sum_{l_1=1}^N \sum_{l_2=1}^N A_{l_1} A_{l_2}^* \frac{\pi}{x_1 t_1^2}. \quad (4.12)$$

Continuing to derive Y , which is in the denominator part of Eq. (4.2)

$$Y = \int_{-\infty}^{\infty} \int_{-\infty}^{\infty} \langle I(r_x, r_y, L) \rangle dr_x dr_y. \quad (4.13)$$

Eq. (4.6) is substituted into Eq. (4.13), then

$$Y = \left(\frac{\pi}{\lambda L} \right)^2 \sum_{l_1=1}^N \sum_{l_2=1}^N A_{l_1} A_{l_2}^* \frac{1}{x_1} \int_{-\infty}^{\infty} \exp(-t_1 r_x^2) dr_x \int_{-\infty}^{\infty} \exp(-t_1 r_y^2) dr_y. \quad (4.14)$$

With the help of Eq. (4.11), Y is found as

$$Y = \left(\frac{\pi}{\lambda L} \right)^2 \sum_{l_1=1}^N \sum_{l_2=1}^N A_{l_1} A_{l_2}^* \frac{1}{x_1} \frac{\pi}{t_1}. \quad (4.15)$$

If X and Y are inserted in Eq. (4.2), beam size along the propagation axis is found to be

$$\sigma_x = \sqrt{\frac{\sum_{l_1=1}^N \sum_{l_2=1}^N A_{l_1} A_{l_2}^* \frac{\pi}{x_1 t_1^2}}{\sum_{l_1=1}^N \sum_{l_2=1}^N A_{l_1} A_{l_2}^* \frac{\pi}{x_1 t_1}}}. \quad (4.16)$$

To observe the beam spread, we need beam size difference after propagation (in Eq. (4.17)) or to observe only turbulence effect on the beam size, Eq. (4.18) is used as

$$\Delta \sigma_{xL} = \sigma_{xL}(z=L) - \sigma_{xL}(z=0), \quad (4.17)$$

or

$$\Delta\sigma_{xL} = \sigma_{xL_{oc}}(z = L) - \sigma_{xL_{fs}}(z = L). \quad (4.18)$$

where $\sigma_{xL_{uw}}(z = L)$ is the beam size in r_x direction at receiver plane after the beam propagates in oceanic turbulent medium and $\sigma_{xL_{fs}}(z = L)$ is the beam size in r_x direction at the receiver plane after the beam propagates in free space. Eq. (4.18) is used in defining the beam spread to obtain only turbulence effect. Beam spread due to propagation is eliminated in our procedure.

4.2 Results for Beam Spread of a Partially Coherent Flat-Topped Beam in Underwater Medium

It should be stated that the beam spread given by Eq. (4.18) is used in our analysis. It is defined as the differences between the beam sizes in r_x direction at the receiver plane in oceanic turbulence and in free space. Figs. 43-48 give the oceanic turbulence effect on beam spread with respect to oceanic turbulence parameter χ_T , ε , and ω for different α_s , N and ρ_s . In Figure 43, with increasing χ_T the oceanic turbulence effect increases so beam spread increases. Figure 43 also shows that if the number of beams composing the flat-topped beam N is larger, the beam spread is smaller along the χ_T axis.

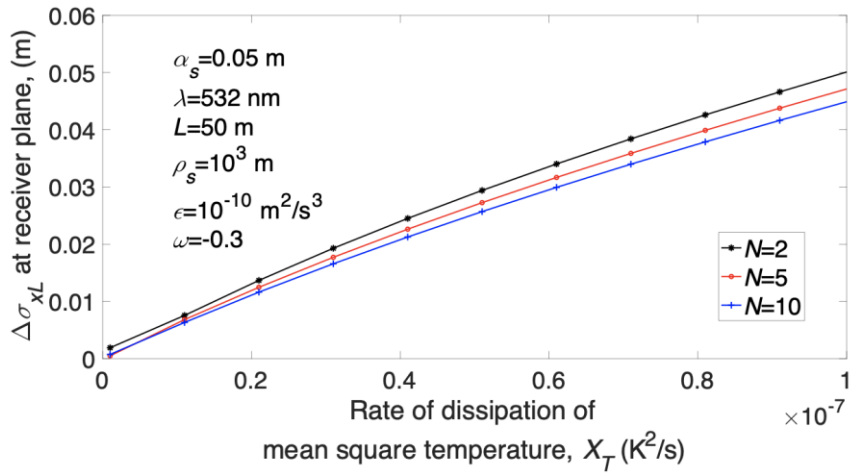


Figure 43 The beam spread due to oceanic turbulence versus the rate of dissipation of mean square temperature χ_T for various number of beams composing the flat-topped beam N .

From Figure 44 it is seen that when the degree of source coherence decreases, the beam spread decreases. However, when the source is more coherent (i.e. ρ_s increases), beam spread increases, since the more coherent source is more affected by the turbulence. When the degree of coherence decreases, the oceanic turbulence effect on the source beam decreases at the receiver plane.

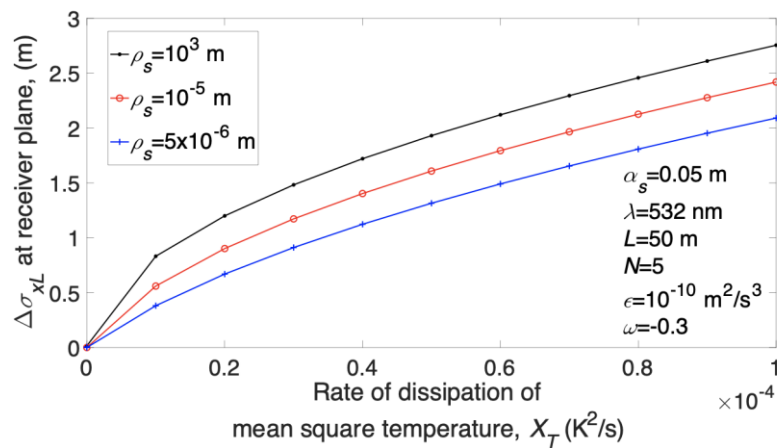


Figure 44 The beam spread due to oceanic turbulence versus the rate of dissipation of mean square temperature χ_T for various degree of partial coherence ρ_s .

In Figure 45, with the increase of χ_T , effects of oceanic turbulence increase because temperature field include many differences from mean square temperature. This causes an increase on the beam spread for all α_s . Additionally, for constant χ_T , the beam spread is less at high values of source sizes. It can be said that the large source size flat-topped beam expands less in the oceanic turbulent medium.

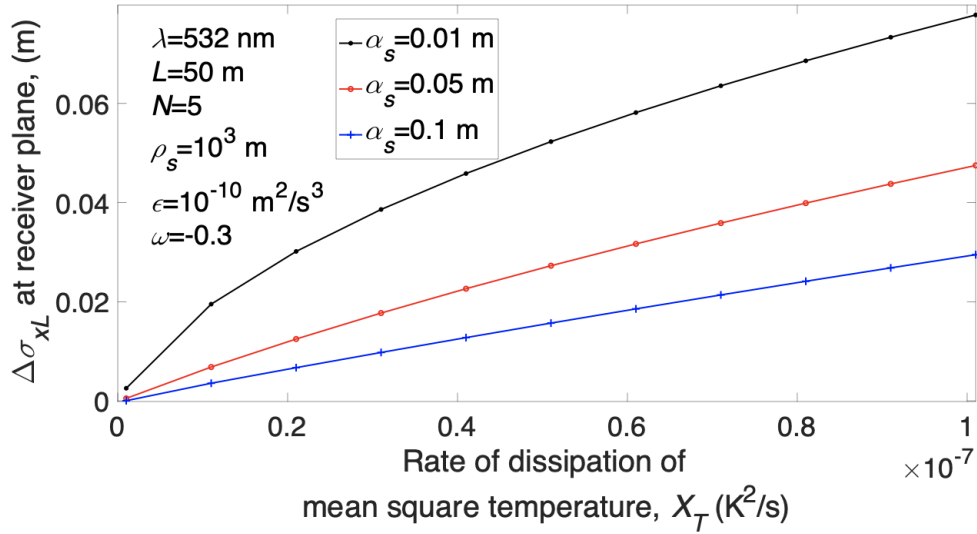


Figure 45 The beam spread due to oceanic turbulence versus the rate of dissipation of mean square temperature χ_T for different source size α_s values.

As Figure 44, Figure 46 also shows that coherent flat-topped beams have larger beam spread than the partially coherent flat-topped beam. Increase in the rate of dissipation of kinetic energy per unit mass of fluid ϵ causes decrease in the kinetic energy that decreases the turbulence effect. This causes to reduce the beam spread.

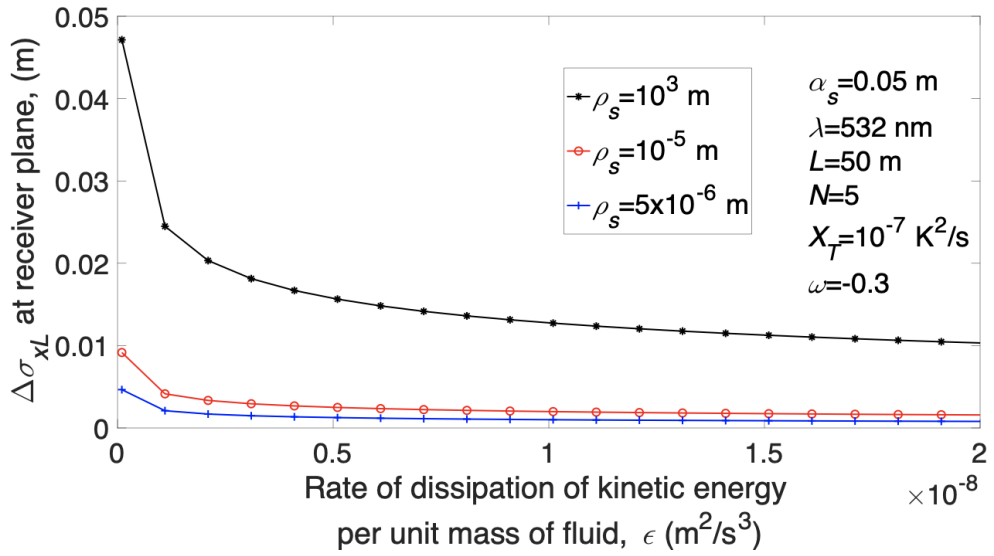


Figure 46 The beam spread due to oceanic turbulence versus the rate of dissipation of kinetic energy per unit mass of fluid ϵ for various degree of partial coherence ρ_s .

In Fig. 47, if the source size of flat-topped beam is larger, beam spread due to the oceanic turbulence is smaller. As the turbulence effect and ϵ are inversely proportional, increase in ϵ causes the beam spread to reduce.

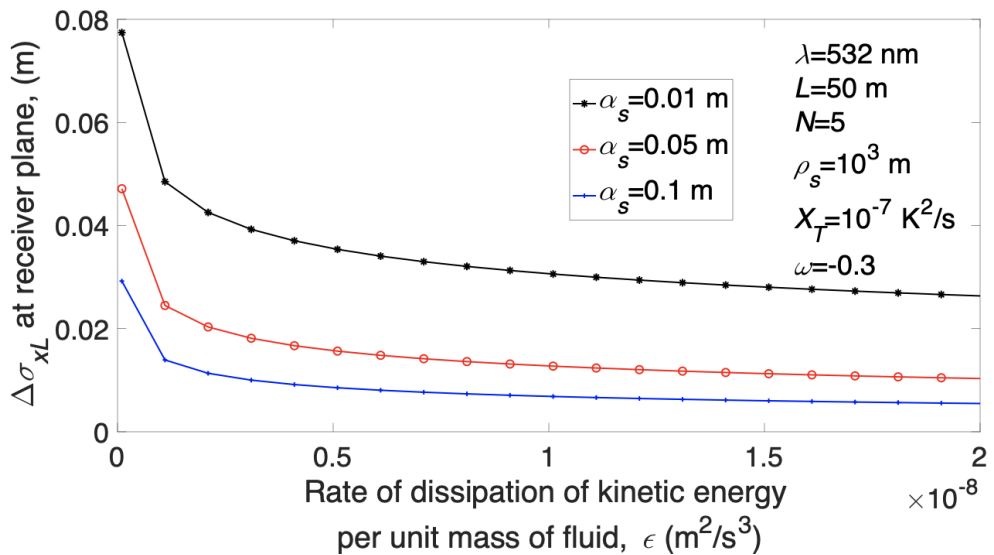


Figure 47 The beam spread due to oceanic turbulence versus the rate of dissipation of kinetic energy per unit mass of fluid ϵ for different source size α_s .

It is seen from Figure 48 that, if source goes to incoherence, the beam spread decreases, and beam size of the source is less affected from turbulence. It is also seen that from Figure 48 that temperature-induced oceanic turbulence causes almost no change on the beam spread. However, the beam expands distinctly when the salinity-induced optical turbulence exists.

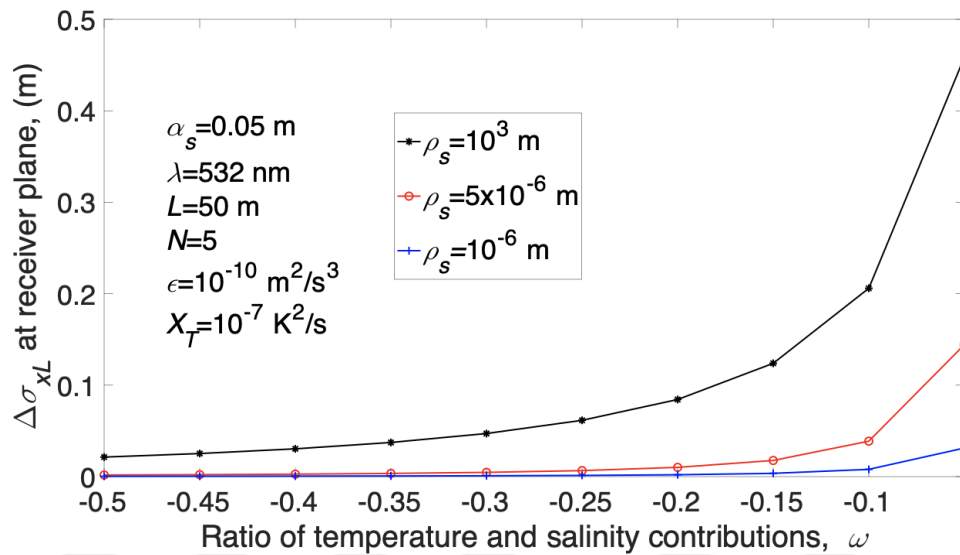


Figure 48 The beam spread due to oceanic turbulence versus the ratio of temperature and salinity contributions ω for various degree of partial coherence ρ_s .

Figures 49-51 give the variations in the beam size in r_x direction with respect to ε and ω at the receiver plane in turbulent underwater. In Figure 49, when the rate of dissipation of kinetic energy increases, beam size at the receiver plane decreases.

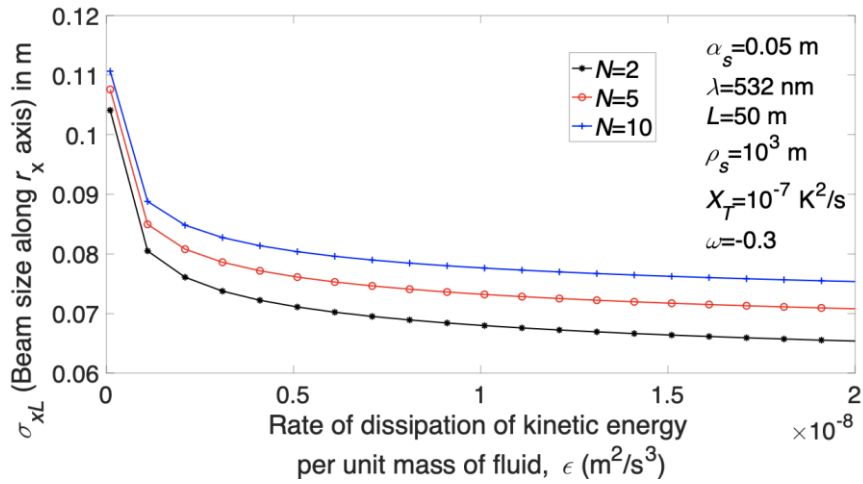


Figure 49 The beam size in r_x direction at the receiver plane versus the rate of dissipation of kinetic energy per unit mass of fluid ϵ for various number of beams composing the flat-topped beam N .

It can be understood from Figures 50 and 51 that when ω is close to zero (i.e. salinity-based turbulence is effective), turbulence gets higher and the beam size in r_x direction at the receiver plane expands. In Figure 50, for a constant ω , if the number of beams composing the flat-topped beam N is larger, the beam size in r_x direction at the receiver plane is larger.

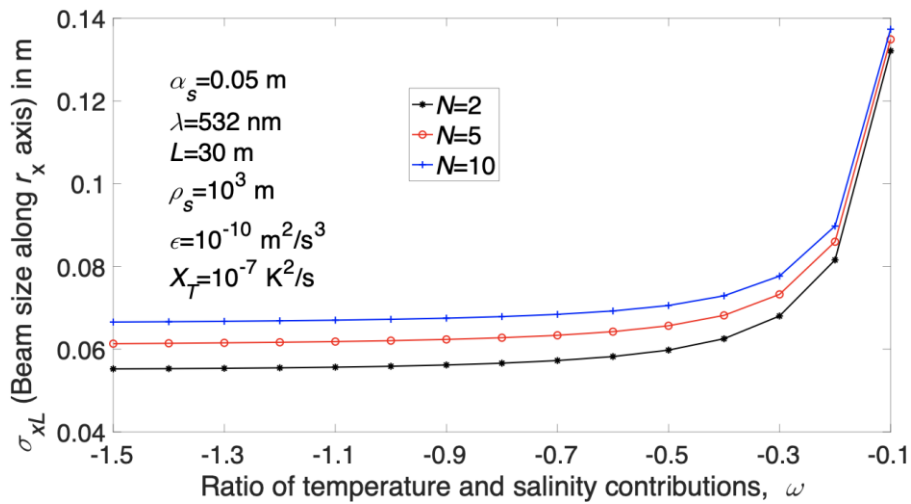


Figure 50 The beam size in r_x direction at the receiver plane versus the ratio of temperature and salinity contributions ω for various number of beams composing the flat-topped beam N .

It is seen from Figure 51 that at a fixed ω , when the source size becomes larger, the beam size in r_x direction at the receiver plane enlarges.

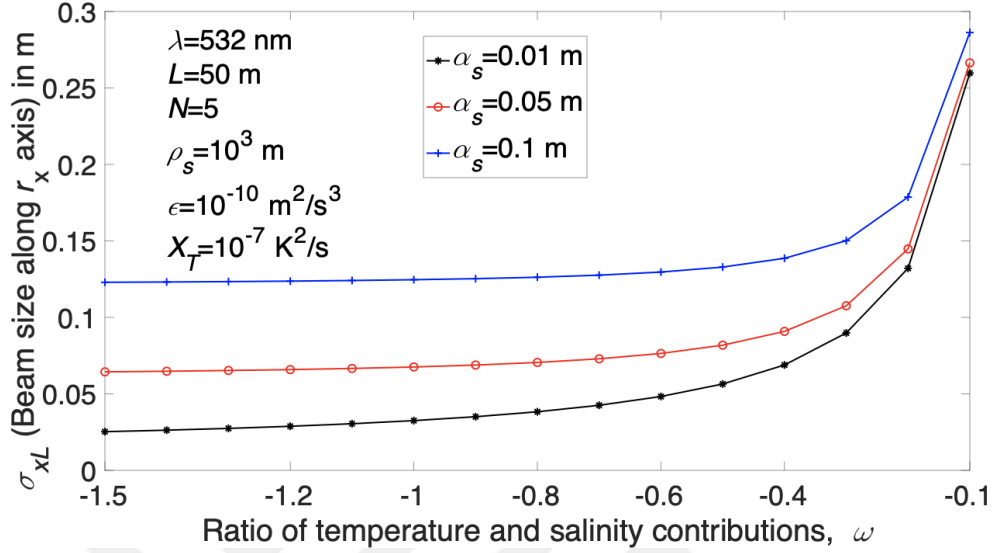


Figure 51 The beam size in r_x direction at the receiver plane versus the ratio of temperature and salinity contributions ω for different source size values α_s .

4.3 Conclusion

If the oceanic turbulence is strong, the beam spread increases [65,113]. With increasing strength of the oceanic turbulence, the beam spread increases that is also supported by Refs. [65,113].

This part of our thesis analyzes the effect of oceanic turbulence on the beam spread of partially coherent flat-topped beam. This part starts with the Carter's definition, which is employed to calculate the beam spread. These results indicate that the partially coherent flat-topped beam is less affected than the partially coherent Gaussian beam and coherent flat-topped beam by the oceanic turbulence. χ_T and ω have similar effects on the beam spread unlike ϵ . Increment of χ_T and ω increase the oceanic turbulence strength, on the contrary an increment in ϵ decreases the

beam spread. The larger sized flat-topped beams exhibit smaller beam spread in underwater turbulence.



CHAPTER 5

INTENSITY SCINTILLATION

5.1 Methodology of Scintillation Index

Scintillation index known as the intensity fluctuations is the normalized intensity variance caused by turbulence. It is obtained by Eq. (5.1) [105]

$$m^2 = \frac{\langle I^2(\mathbf{r}, L) \rangle}{\langle I(\mathbf{r}, L) \rangle^2} - 1, \quad (5.1)$$

where $I(\mathbf{r}, L)$ is the instantaneous intensity at the receiver plane. The average intensity was calculated with the help of the extended Huygens Fresnel principle in Chapter 2, Eq. (2.25). Eq. (2.31) is used which is the special case of Eq. (2.25) that gives the on-axis average intensity for coherent case of cosine-Gaussian beam. This equation also gives the on-axis average intensity of multiple-beam. In this section of this thesis, fourth order moments' derivation of the scintillation index will be given [105].

$$\begin{aligned} \langle I^2(\mathbf{r}, L) \rangle &= \frac{1}{(\lambda L)^4} \int_{-\infty}^{\infty} \int_{-\infty}^{\infty} \mathbf{d}^2 \mathbf{s}_1 \int_{-\infty}^{\infty} \int_{-\infty}^{\infty} \mathbf{d}^2 \mathbf{s}_2 \int_{-\infty}^{\infty} \int_{-\infty}^{\infty} \mathbf{d}^2 \mathbf{s}_3 \int_{-\infty}^{\infty} \int_{-\infty}^{\infty} \mathbf{d}^2 \mathbf{s}_4 \\ &\times \sum_{n=1}^N \sum_{m=1}^N \sum_{\ell=1}^N \sum_{o=1}^N A_n A_m^* A_\ell A_o^* \\ &\times \exp\left(-\frac{1}{2\alpha_s^2} |\mathbf{s}_1|^2 - \frac{1}{2\alpha_s^2} |\mathbf{s}_2|^2 - \frac{1}{2\alpha_s^2} |\mathbf{s}_3|^2 - \frac{1}{2\alpha_s^2} |\mathbf{s}_4|^2\right) \\ &\times \exp(-i\mathbf{V}_n \cdot \mathbf{s}_1) \exp(i\mathbf{V}_m^* \cdot \mathbf{s}_2) \exp(-i\mathbf{V}_\ell \cdot \mathbf{s}_3) \exp(i\mathbf{V}_o^* \cdot \mathbf{s}_4) \\ &\times \exp\left[\frac{ik}{2L} (|\mathbf{s}_1|^2 - |\mathbf{s}_2|^2 + |\mathbf{s}_3|^2 - |\mathbf{s}_4|^2)\right] \Gamma_4^m(\mathbf{s}_1, \mathbf{s}_2, \mathbf{s}_3, \mathbf{s}_4, \mathbf{r}), \end{aligned} \quad (5.2)$$

where the fourth-order medium correlation function is given for weak turbulence as [105]

$$\begin{aligned}
\Gamma_4^m(\mathbf{s}_1, \mathbf{s}_2, \mathbf{s}_3, \mathbf{s}_4, \mathbf{r}) &= \left\langle \exp[\psi(\mathbf{s}_1, \mathbf{r})] \exp[\psi^*(\mathbf{s}_2, \mathbf{r})] \right. \\
&\quad \left. \exp[\psi(\mathbf{s}_3, \mathbf{r})] \exp[\psi^*(\mathbf{s}_4, \mathbf{r})] \right\rangle \\
&= \left[1 + 2B_\chi(\mathbf{s}_1 - \mathbf{s}_3) + 2B_\chi(\mathbf{s}_2 - \mathbf{s}_4) \right] \\
&\quad \exp\left[-0.5D_\psi(\mathbf{s}_1 - \mathbf{s}_2) - 0.5D_\psi(\mathbf{s}_3 - \mathbf{s}_4) \right. \\
&\quad \left. - 0.5D_\psi(\mathbf{s}_2 - \mathbf{s}_3) - 0.5D_\psi(\mathbf{s}_1 - \mathbf{s}_4) \right. \\
&\quad \left. + 0.5D_\psi(\mathbf{s}_1 - \mathbf{s}_3) + 0.5D_\psi(\mathbf{s}_2 - \mathbf{s}_4) \right. \\
&\quad \left. + iD_{\chi s}(\mathbf{s}_2 - \mathbf{s}_4) - iD_{\chi s}(\mathbf{s}_1 - \mathbf{s}_3) \right]. \tag{5.3}
\end{aligned}$$

Here Eqs. (5.4) to (5.6) are the log-amplitude correlation, wave structure and log-amplitude phase structure functions, respectively, which are given as [105]

$$B_\chi(\mathbf{s}_n - \mathbf{s}_m) = \sigma_\chi^2 \exp\left(-|\mathbf{s}_n - \mathbf{s}_m|^2 \rho_0^{-2}\right), \quad n=1,2 \text{ and } m=3,4, \tag{5.4}$$

$$D_\psi(\mathbf{s}_r - \mathbf{s}_q) = 2\left(|\mathbf{s}_r - \mathbf{s}_q|^2 \rho_0^{-2}\right), \quad r=1-3 \text{ and } q=2-4, \tag{5.5}$$

$$D_{\chi s}(\mathbf{s}_r - \mathbf{s}_q) = \frac{|\mathbf{s}_r - \mathbf{s}_q|^2}{\rho_{\chi s}^2}, \quad r=1-3, \text{ and } q=2-4, \tag{5.6}$$

where $\sigma_\chi^2 = 0.124C_n^2 k^{7/6} L^{11/6}$ is the log amplitude variance, and the coherence length of the log amplitude and phase is $\rho_{\chi s} = \left(0.114k^{13/6} C_n^2 L^{5/6}\right)^{-1/2}$. C_n^2 is the parameter of structure constant for horizontal links which is expressed in [154] in terms of the underwater turbulence parameters as

$$C_n^2 = 16\pi^2 k^{-7/6} L^{-11/6} \operatorname{Re} \left\{ \int_0^L d\zeta \int_0^\infty \kappa d\kappa [E(\zeta, \kappa, L) \right. \\ \left. \times E(\zeta, -\kappa, L) + |E(\zeta, \kappa, L)|^2] \Phi_n(\kappa) \right\}, \quad (5.7)$$

where for the spherical wave,

$$E(\zeta, \kappa, L) = ik \exp \left[-\frac{0.5i\zeta(L-\zeta)\kappa^2}{kL} \right]. \quad (5.8)$$

C_n^2 is calculated numerically for the oceanic turbulent medium and validated by Ref. [154]. Then it is used to examine the scintillation index.

From Eqs. (5.4), (5.5) and (5.6) we obtained

$$\begin{aligned} B_\chi(s_1 - s_3) &= \sigma_\chi^2 \exp(-|s_1 - s_3|^2 \rho_0^{-2}), \\ B_\chi(s_2 - s_4) &= \sigma_\chi^2 \exp(-|s_2 - s_4|^2 \rho_0^{-2}), \\ D_\psi(s_1 - s_2) &= 2(|s_1 - s_2|^2 \rho_0^{-2}), \quad D_\psi(s_3 - s_4) = 2(|s_3 - s_4|^2 \rho_0^{-2}), \\ D_\psi(s_2 - s_3) &= 2(|s_2 - s_3|^2 \rho_0^{-2}), \quad D_\psi(s_1 - s_4) = 2(|s_1 - s_4|^2 \rho_0^{-2}), \\ D_\psi(s_1 - s_3) &= 2(|s_1 - s_3|^2 \rho_0^{-2}), \quad D_\psi(s_2 - s_4) = 2(|s_2 - s_4|^2 \rho_0^{-2}), \\ D_{\chi S}(s_2 - s_4) &= \frac{|s_2 - s_4|^2}{\rho_{\chi S}^2}, \quad D_{\chi S}(s_1 - s_3) = \frac{|s_1 - s_3|^2}{\rho_{\chi S}^2}, \end{aligned} \quad (5.9)$$

then Eqs. (5.3) and (5.7) are substituted into (5.2) and $\langle I^2(p, L) \rangle$ is obtained to be

$$\begin{aligned}
\langle I^2(\mathbf{r}, L) \rangle &= \frac{1}{(\lambda L)^4} \int_{-\infty}^{\infty} \int_{-\infty}^{\infty} \mathbf{d}^2 \mathbf{s}_1 \int_{-\infty}^{\infty} \int_{-\infty}^{\infty} \mathbf{d}^2 \mathbf{s}_2 \int_{-\infty}^{\infty} \int_{-\infty}^{\infty} \mathbf{d}^2 \mathbf{s}_3 \int_{-\infty}^{\infty} \int_{-\infty}^{\infty} \mathbf{d}^2 \mathbf{s}_4 \\
&\times \sum_{n=1}^N \sum_{m=1}^N \sum_{\ell=1}^N \sum_{o=1}^N A_n A_m^* A_\ell A_o^* \\
&\times \exp \left[\left(\frac{ik}{2L} - \frac{1}{2\alpha_s^2} \right) |\mathbf{s}_1|^2 - \left(\frac{ik}{2L} + \frac{1}{2\alpha_s^2} \right) |\mathbf{s}_2|^2 \right. \\
&\quad \left. + \left(\frac{ik}{2L} - \frac{1}{2\alpha_s^2} \right) |\mathbf{s}_3|^2 - \left(\frac{ik}{2L} + \frac{1}{2\alpha_s^2} \right) |\mathbf{s}_4|^2 \right] \\
&\times \exp(-i\mathbf{V}_n \cdot \mathbf{s}_1) \exp(i\mathbf{V}_m^* \cdot \mathbf{s}_2) \exp(-i\mathbf{V}_\ell \cdot \mathbf{s}_3) \exp(i\mathbf{V}_o^* \cdot \mathbf{s}_4) \\
&\times \left[1 + 2\sigma_\chi^2 \exp(-|\mathbf{s}_1 - \mathbf{s}_3|^2 \rho_0^{-2}) + 2\sigma_\chi^2 \exp(-|\mathbf{s}_2 - \mathbf{s}_4|^2 \rho_0^{-2}) \right] \\
&\times \exp \left[-(|\mathbf{s}_1 - \mathbf{s}_2|^2 \rho_0^{-2}) - (|\mathbf{s}_3 - \mathbf{s}_4|^2 \rho_0^{-2}) \right. \\
&\quad \left. - (|\mathbf{s}_2 - \mathbf{s}_3|^2 \rho_0^{-2}) - (|\mathbf{s}_1 - \mathbf{s}_4|^2 \rho_0^{-2}) \right. \\
&\quad \left. + (|\mathbf{s}_1 - \mathbf{s}_3|^2 \rho_0^{-2}) + (|\mathbf{s}_2 - \mathbf{s}_4|^2 \rho_0^{-2}) + i \frac{|\mathbf{s}_2 - \mathbf{s}_4|^2}{\rho_{\chi s}^2} - i \frac{|\mathbf{s}_1 - \mathbf{s}_3|^2}{\rho_{\chi s}^2} \right].
\end{aligned} \tag{5.10}$$

where

$$\begin{aligned}
|\mathbf{s}_a| &= s_{ax}^2 + s_{ay}^2, \quad a = 1, \dots, 4, \\
|\mathbf{s}_b - \mathbf{s}_c| &= (s_{bx} - s_{cx})^2 + (s_{by} - s_{cy})^2, \quad b = 1, \dots, 3, \quad c = 2, \dots, 4, \\
(\mathbf{V}_d \cdot \mathbf{s}_a) &= (V_{ax} s_{bx} + V_{ay} s_{by}), \quad d = n, m, \ell, o, \quad a = 1, \dots, 4,
\end{aligned} \tag{5.11}$$

with combining the Eq. (5.10) & (5.11), we obtain

$$\begin{aligned}
\langle I^2(\mathbf{r}, L) \rangle &= \frac{1}{(\lambda L)^4} \int_{-\infty}^{\infty} \int_{-\infty}^{\infty} \mathbf{d}^2 \mathbf{s}_1 \int_{-\infty}^{\infty} \int_{-\infty}^{\infty} \mathbf{d}^2 \mathbf{s}_2 \int_{-\infty}^{\infty} \int_{-\infty}^{\infty} \mathbf{d}^2 \mathbf{s}_3 \int_{-\infty}^{\infty} \int_{-\infty}^{\infty} \mathbf{d}^2 \mathbf{s}_4 \\
&\times \sum_{n=1}^N \sum_{m=1}^N \sum_{\ell=1}^N \sum_{o=1}^N A_n A_m^* A_\ell A_o^* \\
&\times \exp \left[\left(\frac{ik}{2L} - \frac{1}{2\alpha_s^2} \right) (s_{1x}^2 + s_{1y}^2) - \left(\frac{ik}{2L} + \frac{1}{2\alpha_s^2} \right) (s_{2x}^2 + s_{2y}^2) \right. \\
&\quad \left. + \left(\frac{ik}{2L} - \frac{1}{2\alpha_s^2} \right) (s_{3x}^2 + s_{3y}^2) - \left(\frac{ik}{2L} + \frac{1}{2\alpha_s^2} \right) (s_{4x}^2 + s_{4y}^2) \right] \\
&\times \exp \left[-i(V_{nx}s_{1x} + V_{ny}s_{1y}) \right] \exp \left[i(V_{mx}^*s_{2x} + V_{my}^*s_{2y}) \right] \\
&\times \exp \left[-i(V_{\ell x}s_{3x} + V_{\ell y}s_{3y}) \right] \exp \left[i(V_{ox}^*s_{4x} + V_{oy}^*s_{4y}) \right] \\
&\times \left(1 + 2\sigma_z^2 \exp \left\{ - \left[(s_{1x} - s_{3x})^2 + (s_{1y} - s_{3y})^2 \right] \rho_0^{-2} \right\} \right. \\
&\quad \left. + 2\sigma_z^2 \exp \left\{ - \left[(s_{2x} - s_{4x})^2 + (s_{2y} - s_{4y})^2 \right] \rho_0^{-2} \right\} \right) \\
&\times \exp \left\{ - \left[(s_{1x} - s_{2x})^2 + (s_{1y} - s_{2y})^2 \right] \rho_0^{-2} \right. \\
&\quad - \left[(s_{3x} - s_{4x})^2 + (s_{3y} - s_{4y})^2 \right] \rho_0^{-2} \\
&\quad - \left[(s_{2x} - s_{3x})^2 + (s_{2y} - s_{3y})^2 \right] \rho_0^{-2} \\
&\quad - \left[(s_{1x} - s_{4x})^2 + (s_{1y} - s_{4y})^2 \right] \rho_0^{-2} \\
&\quad + \left[(s_{1x} - s_{3x})^2 + (s_{1y} - s_{3y})^2 \right] \rho_0^{-2} \\
&\quad + \left[(s_{2x} - s_{4x})^2 + (s_{2y} - s_{4y})^2 \right] \rho_0^{-2} \\
&\quad + i \left[(s_{2x} - s_{4x})^2 + (s_{2y} - s_{4y})^2 \right] \rho_z^{-2} s \\
&\quad \left. - i \left[(s_{1x} - s_{3x})^2 + (s_{1y} - s_{3y})^2 \right] \rho_z^{-2} s \right\}.
\end{aligned} \tag{5.12}$$

We derive Eq. (5.12) in three parts, which are given below from Eq. (5.13) to (5.15).

$$\begin{aligned}
\langle I^2(\mathbf{r}, L) \rangle_{p=1} &= \frac{1}{(\lambda L)^4} \int_{-\infty}^{\infty} \int_{-\infty}^{\infty} \mathbf{d}^2 \mathbf{s}_1 \int_{-\infty}^{\infty} \int_{-\infty}^{\infty} \mathbf{d}^2 \mathbf{s}_2 \int_{-\infty}^{\infty} \int_{-\infty}^{\infty} \mathbf{d}^2 \mathbf{s}_3 \int_{-\infty}^{\infty} \int_{-\infty}^{\infty} \mathbf{d}^2 \mathbf{s}_4 \\
&\times \sum_{n=1}^N \sum_{m=1}^N \sum_{\ell=1}^N \sum_{o=1}^N A_n A_m^* A_\ell A_o^* \\
&\times \exp \left[\left(\frac{ik}{2L} - \frac{1}{2\alpha_s^2} \right) s_{1x}^2 + \left(\frac{ik}{2L} - \frac{1}{2\alpha_s^2} \right) s_{1y}^2 \right. \\
&\quad - \left(\frac{ik}{2L} + \frac{1}{2\alpha_s^2} \right) s_{2x}^2 - \left(\frac{ik}{2L} + \frac{1}{2\alpha_s^2} \right) s_{2y}^2 \\
&\quad + \left(\frac{ik}{2L} - \frac{1}{2\alpha_s^2} \right) s_{3x}^2 + \left(\frac{ik}{2L} - \frac{1}{2\alpha_s^2} \right) s_{3y}^2 \\
&\quad \left. - \left(\frac{ik}{2L} + \frac{1}{2\alpha_s^2} \right) s_{4x}^2 - \left(\frac{ik}{2L} + \frac{1}{2\alpha_s^2} \right) s_{4y}^2 \right] \\
&\times \exp \left[-i(V_{nx}s_{1x} + V_{ny}s_{1y}) \right] \exp \left[i(V_{mx}^*s_{2x} + V_{my}^*s_{2y}) \right] \\
&\times \exp \left[-i(V_{\ell x}s_{3x} + V_{\ell y}s_{3y}) \right] \exp \left[i(V_{ox}^*s_{4x} + V_{oy}^*s_{4y}) \right] \\
&\times \exp \left\{ -\left(s_{1x}^2 - 2s_{1x}s_{2x} + s_{2x}^2 \right) \rho_0^{-2} - \left(s_{1y} - s_{2y} \right)^2 \rho_0^{-2} \right. \\
&\quad - \left[\left(s_{3x}^2 - 2s_{3x}s_{4x} + s_{4x}^2 \right) \rho_0^{-2} + \left(s_{3y} - s_{4y} \right)^2 \rho_0^{-2} \right] \\
&\quad - \left[\left(s_{2x}^2 - 2s_{2x}s_{3x} + s_{3x}^2 \right) \rho_0^{-2} + \left(s_{2y} - s_{3y} \right)^2 \rho_0^{-2} \right] \\
&\quad - \left[\left(s_{1x}^2 - 2s_{1x}s_{4x} + s_{4x}^2 \right) \rho_0^{-2} + \left(s_{1y} - s_{4y} \right)^2 \rho_0^{-2} \right] \\
&\quad + \left[\left(s_{1x}^2 - 2s_{1x}s_{3x} + s_{3x}^2 \right) \rho_0^{-2} + \left(s_{1y} - s_{3y} \right)^2 \rho_0^{-2} \right] \\
&\quad + \left[\left(s_{2x}^2 - 2s_{2x}s_{4x} + s_{4x}^2 \right) \rho_0^{-2} + \left(s_{2y} - s_{4y} \right)^2 \rho_0^{-2} \right] \\
&\quad + i \left[\left(s_{2x}^2 - 2s_{2x}s_{4x} + s_{4x}^2 \right) \rho_{\chi}^{-2} s + \left(s_{2y} - s_{4y} \right)^2 \rho_{\chi}^{-2} s \right] \\
&\quad \left. - i \left[\left(s_{1x}^2 - 2s_{1x}s_{3x} + s_{3x}^2 \right) \rho_{\chi}^{-2} s + \left(s_{1y} - s_{3y} \right)^2 \rho_{\chi}^{-2} s \right] \right\}, \tag{5.13}
\end{aligned}$$

Rearranging

$$\begin{aligned}
\langle I^2(\mathbf{r}, L) \rangle_{p=2} &= \frac{1}{(\lambda L)^4} \int_{-\infty}^{\infty} \int_{-\infty}^{\infty} \mathbf{d}^2 \mathbf{s}_1 \int_{-\infty}^{\infty} \int_{-\infty}^{\infty} \mathbf{d}^2 \mathbf{s}_2 \int_{-\infty}^{\infty} \int_{-\infty}^{\infty} \mathbf{d}^2 \mathbf{s}_3 \int_{-\infty}^{\infty} \int_{-\infty}^{\infty} \mathbf{d}^2 \mathbf{s}_4 \\
&\times \sum_{n=1}^N \sum_{m=1}^N \sum_{\ell=1}^N \sum_{o=1}^N A_n A_m^* A_\ell A_o^* \\
&\times 2\sigma_z^2 \exp \left[-\left(s_{1x}^2 - 2s_{1x}s_{3x} + s_{3x}^2 \right) \rho_0^{-2} - \left(s_{1y} - s_{3y} \right)^2 \rho_0^{-2} \right] \\
&\times \exp \left[\left(\frac{ik}{2L} - \frac{1}{2\alpha_s^2} \right) s_{1x}^2 + \left(\frac{ik}{2L} - \frac{1}{2\alpha_s^2} \right) s_{1y}^2 \right. \\
&\quad - \left(\frac{ik}{2L} + \frac{1}{2\alpha_s^2} \right) s_{2x}^2 - \left(\frac{ik}{2L} + \frac{1}{2\alpha_s^2} \right) s_{2y}^2 \\
&\quad + \left(\frac{ik}{2L} - \frac{1}{2\alpha_s^2} \right) s_{3x}^2 + \left(\frac{ik}{2L} - \frac{1}{2\alpha_s^2} \right) s_{3y}^2 \\
&\quad \left. - \left(\frac{ik}{2L} + \frac{1}{2\alpha_s^2} \right) s_{4x}^2 - \left(\frac{ik}{2L} + \frac{1}{2\alpha_s^2} \right) s_{4y}^2 \right] \\
&\times \exp \left[-i \left(V_{nx} s_{1x} + V_{ny} s_{1y} \right) \right] \exp \left[i \left(V_{mx}^* s_{2x} + V_{my}^* s_{2y} \right) \right] \\
&\times \exp \left[-i \left(V_{\ell x} s_{3x} + V_{\ell y} s_{3y} \right) \right] \exp \left[i \left(V_{ox}^* s_{4x} + V_{oy}^* s_{4y} \right) \right] \\
&\times \exp \left\{ -\left(s_{1x}^2 - 2s_{1x}s_{2x} + s_{2x}^2 \right) \rho_0^{-2} - \left(s_{1y} - s_{2y} \right)^2 \rho_0^{-2} \right. \\
&\quad - \left[\left(s_{3x}^2 - 2s_{3x}s_{4x} + s_{4x}^2 \right) \rho_0^{-2} + \left(s_{3y} - s_{4y} \right)^2 \rho_0^{-2} \right] \\
&\quad - \left[\left(s_{2x}^2 - 2s_{2x}s_{3x} + s_{3x}^2 \right) \rho_0^{-2} + \left(s_{2y} - s_{3y} \right)^2 \rho_0^{-2} \right] \\
&\quad - \left[\left(s_{1x}^2 - 2s_{1x}s_{4x} + s_{4x}^2 \right) \rho_0^{-2} + \left(s_{1y} - s_{4y} \right)^2 \rho_0^{-2} \right] \\
&\quad + \left[\left(s_{1x}^2 - 2s_{1x}s_{3x} + s_{3x}^2 \right) \rho_0^{-2} + \left(s_{1y} - s_{3y} \right)^2 \rho_0^{-2} \right] \\
&\quad + \left[\left(s_{2x}^2 - 2s_{2x}s_{4x} + s_{4x}^2 \right) \rho_0^{-2} + \left(s_{2y} - s_{4y} \right)^2 \rho_0^{-2} \right] \\
&\quad + i \left[\left(s_{2x}^2 - 2s_{2x}s_{4x} + s_{4x}^2 \right) \rho_{\chi s}^{-2} + \left(s_{2y} - s_{4y} \right)^2 \rho_{\chi s}^{-2} \right] \\
&\quad \left. - i \left[\left(s_{1x}^2 - 2s_{1x}s_{3x} + s_{3x}^2 \right) \rho_{\chi s}^{-2} + \left(s_{1y} - s_{3y} \right)^2 \rho_{\chi s}^{-2} \right] \right\},
\end{aligned} \tag{5.14}$$

Rearranging

$$\begin{aligned}
\langle I^2(\mathbf{p}, L) \rangle_{p=3} &= \frac{1}{(\lambda L)^4} \int_{-\infty}^{\infty} \int_{-\infty}^{\infty} \mathbf{d}^2 \mathbf{s}_1 \int_{-\infty}^{\infty} \int_{-\infty}^{\infty} \mathbf{d}^2 \mathbf{s}_2 \int_{-\infty}^{\infty} \int_{-\infty}^{\infty} \mathbf{d}^2 \mathbf{s}_3 \int_{-\infty}^{\infty} \int_{-\infty}^{\infty} \mathbf{d}^2 \mathbf{s}_4 \\
&\times \sum_{n=1}^N \sum_{m=1}^N \sum_{\ell=1}^N \sum_{o=1}^N A_n A_m^* A_\ell A_o^* \\
&\times 2\sigma_\chi^2 \exp \left[-\left(s_{2x}^2 - 2s_{2x}s_{4x} + s_{4x}^2 \right) \rho_0^{-2} - \left(s_{2y} - s_{4y} \right)^2 \rho_0^{-2} \right] \\
&\times \exp \left[\left(\frac{ik}{2L} - \frac{1}{2\alpha_s^2} \right) s_{1x}^2 + \left(\frac{ik}{2L} - \frac{1}{2\alpha_s^2} \right) s_{1y}^2 \right. \\
&\quad - \left(\frac{ik}{2L} + \frac{1}{2\alpha_s^2} \right) s_{2x}^2 - \left(\frac{ik}{2L} + \frac{1}{2\alpha_s^2} \right) s_{2y}^2 \\
&\quad + \left(\frac{ik}{2L} - \frac{1}{2\alpha_s^2} \right) s_{3x}^2 + \left(\frac{ik}{2L} - \frac{1}{2\alpha_s^2} \right) s_{3y}^2 \\
&\quad \left. - \left(\frac{ik}{2L} + \frac{1}{2\alpha_s^2} \right) s_{4x}^2 - \left(\frac{ik}{2L} + \frac{1}{2\alpha_s^2} \right) s_{4y}^2 \right] \\
&\times \exp \left[-i \left(V_{mx} s_{1x} + V_{my} s_{1y} \right) \right] \exp \left[i \left(V_{mx}^* s_{2x} + V_{my}^* s_{2y} \right) \right] \\
&\times \exp \left[-i \left(V_{\ell x} s_{3x} + V_{\ell y} s_{3y} \right) \right] \exp \left[i \left(V_{\ell x}^* s_{4x} + V_{\ell y}^* s_{4y} \right) \right] \\
&\times \exp \left\{ -\left(s_{1x}^2 - 2s_{1x}s_{2x} + s_{2x}^2 \right) \rho_0^{-2} - \left(s_{1y} - s_{2y} \right)^2 \rho_0^{-2} \right. \\
&\quad - \left[\left(s_{3x}^2 - 2s_{3x}s_{4x} + s_{4x}^2 \right) \rho_0^{-2} + \left(s_{3y} - s_{4y} \right)^2 \rho_0^{-2} \right] \\
&\quad - \left[\left(s_{2x}^2 - 2s_{2x}s_{3x} + s_{3x}^2 \right) \rho_0^{-2} + \left(s_{2y} - s_{3y} \right)^2 \rho_0^{-2} \right] \\
&\quad - \left[\left(s_{1x}^2 - 2s_{1x}s_{4x} + s_{4x}^2 \right) \rho_0^{-2} + \left(s_{1y} - s_{4y} \right)^2 \rho_0^{-2} \right] \\
&\quad + \left[\left(s_{1x}^2 - 2s_{1x}s_{3x} + s_{3x}^2 \right) \rho_0^{-2} + \left(s_{1y} - s_{3y} \right)^2 \rho_0^{-2} \right] \\
&\quad + \left[\left(s_{2x}^2 - 2s_{2x}s_{4x} + s_{4x}^2 \right) \rho_0^{-2} + \left(s_{2y} - s_{4y} \right)^2 \rho_0^{-2} \right] \\
&\quad + i \left[\left(s_{2x}^2 - 2s_{2x}s_{4x} + s_{4x}^2 \right) \rho_\chi^{-2} s + \left(s_{2y} - s_{4y} \right)^2 \rho_\chi^{-2} s \right] \\
&\quad \left. - i \left[\left(s_{1x}^2 - 2s_{1x}s_{3x} + s_{3x}^2 \right) \rho_\chi^{-2} s + \left(s_{1y} - s_{3y} \right)^2 \rho_\chi^{-2} s \right] \right\}.
\end{aligned} \tag{5.15}$$

Eqs. (5.12), (5.13) and (5.14) are integrated by the help of Eq. (2.20) with the similar procedure of the average intensity calculation. Then, Eq. (5.12) converts to

$$\begin{aligned}
\langle I^2(\mathbf{p}, L) \rangle_{p=1} &= \frac{1}{(\lambda L)^4} \sum_{n=1}^N \sum_{m=1}^N \sum_{\ell=1}^N \sum_{o=1}^N A_n A_m^* A_\ell A_o^* \frac{\pi^4}{H_{p1} H_{p2} H_{p3} H_{p4}} \\
&\times \exp \left\{ \left[-i\rho_0^{-2} V_n \left(\frac{T_p}{H_{p1}} + 1 \right) + iV_m^* (T_p + H_{p1}) \right]^2 \right. \\
&\times \left(\frac{\rho_0^{-2}}{H_{p2} H_{p1}} \right)^2 \frac{2}{4H_{p3}} \left. \exp \left[\frac{-T_p^2 V_n^2}{2H_{p3} H_{p1}^2} \right. \right. \\
&+ \frac{-V_\ell^2 H_{p1}^2}{2H_{p3} H_{p1}^2} + \frac{-T_p V_n V_\ell H_{p1}}{H_{p3} H_{p1}^2} - i\rho_0^{-2} V_n \left(\frac{T_p}{H_{p1}} + 1 \right) \\
&\left. \left. \frac{(-T_p iV_n - iV_\ell H_{p1}) \rho_0^{-2}}{H_{p3} H_{p2} H_{p1}^2} \right] \exp \left(\frac{-V_n^2}{2H_{p1}} \right) \right. \\
&\times \exp \left[iV_m^* (T_p + H_{p1}) \frac{(-T_p iV_n - iV_\ell H_{p1}) \rho_0^{-2}}{H_{p3} H_{p2} H_{p1}^2} \right] \\
&\times \exp \left[\frac{(-i\rho_0^{-2} V_n + iV_m^* H_{p1})^2}{2H_{p2} H_{p1}^2} \right] \exp \left(\frac{1}{2H_{p4}} \left\{ \frac{\rho_0^{-2}}{H_{p1}} \frac{i}{H_{p2}} \right. \right. \\
&\times \left. \left. \left[\left(\frac{\rho_0^{-2}}{H_{p1} \rho_0^2} - R_p \right) \left(-V_n + V_m^* \frac{H_{p1}}{\rho_0^{-2}} \right) - H_{p2} V_n \right] + iV_o^* \right\}^2 \right) \\
&\times \exp \left\{ \frac{1}{2H_{p4}} \left(\frac{\rho_0^{-2}}{H_{p3} H_{p2} H_{p1}^2} \right)^2 \right. \\
&\times \left[\left(iV_m^* - i\rho_0^{-2} V_n \frac{1}{H_{p1}} \right) (T_p + H_{p1}) \frac{\rho_0^{-2}}{H_{p2}} - T_p iV_n - iV_\ell H_{p1} \right]^2 \\
&\times \left[\rho_0^{-2} \left(\frac{T_p}{H_{p1}} \rho_0^{-2} + \rho_0^{-2} \right) - R_p (T_p + H_{p1}) + (T_p + H_{p1}) H_{p2} \right]^2 \left. \right\} \\
&\times \exp \left(\frac{1}{H_{p4}} \left\{ \frac{\rho_0^{-2}}{H_{p1}} \frac{i}{H_{p2}} \left[\left(\frac{\rho_0^{-2}}{H_{p1} \rho_0^2} - R_p \right) \right. \right. \right. \\
&\times \left. \left. \left(-V_n + V_m^* \frac{H_{p1}}{\rho_0^{-2}} \right) - H_{p2} V_n \right] + iV_o^* \right\} \left(\frac{\rho_0^{-2}}{H_{p3} H_{p2} H_{p1}^2} \right) \right. \\
&\times \left[\left(iV_m^* - i\rho_0^{-2} V_n \frac{1}{H_{p1}} \right) (T_p + H_{p1}) \frac{\rho_0^{-2}}{H_{p2}} - T_p iV_n - iV_\ell H_{p1} \right] \\
&\times \left. \left[\rho_0^{-2} \left(\frac{T_p}{H_{p1}} \rho_0^{-2} + \rho_0^{-2} \right) - R_p (T_p + H_{p1}) + (T_p + H_{p1}) H_{p2} \right] \right),
\end{aligned} \tag{5.16}$$

where,

$$\begin{aligned}
H_{p1} &= \frac{1}{2\alpha_s^2} - \frac{ik}{2L} + 2\rho_0^{-2} + T_p, & T_p &= i\rho_{\chi s}^{-2} - \rho_0^{-2}. \\
H_{p2} &= -\frac{\rho_0^{-4}}{H_{p1}} + \frac{1}{2\alpha_s^2} + \frac{ik}{2L} + 2\rho_0^{-2} - R_p, & R_p &= \rho_0^{-2} + i\rho_{\chi s}^{-2}. \\
H_{p3} &= H_{p1} - \frac{T_p^2}{H_{p1}} - \frac{1}{H_{p2}} \left(\frac{T_p}{H_{p1}} \rho_0^{-2} + \rho_0^{-2} \right)^2, & T_p &= i\rho_{\chi s}^{-2} - \rho_0^{-2}. \\
H_{p4} &= H_{p2} - \frac{1}{H_{p2}} \left(\frac{\rho_0^{-2}}{H_{p1}\rho_0^2} - R_n \right)^2 \\
&\quad - \frac{1}{H_{p3}} \left[\left(\frac{\rho_0^{-2}}{H_{p2}H_{p1}\rho_0^2} - \frac{R_p}{H_{p2}} \right) \left(\frac{T_p}{H_{p1}} \rho_0^{-2} + \rho_0^{-2} \right) \right. \\
&\quad \left. + \left(\frac{T_p}{H_{p1}} \rho_0^{-2} + \rho_0^{-2} \right)^2 \right].
\end{aligned} \tag{5.17}$$

With the same procedure, the second part of the integration which is Eq. (5.13) can be found as

$$\begin{aligned}
\langle I^2(p, L) \rangle_{p=2} &= \sum_{n=1}^N \sum_{m=1}^N \sum_{\ell=1}^N \sum_{o=1}^N A_n A_m^* A_\ell A_o^* \frac{\pi^4}{(\lambda L)^4} \frac{2\sigma_\chi^2}{H_{p1} H_{p2} H_{p3} H_{p4}} \\
&\quad \times \exp \left(-\frac{V_n^2 \rho_0^{-4}}{2H_{p2} H_{p1}^2} + \frac{V_n V_m^* \rho_0^{-2}}{H_{p2} H_{p1}} - \frac{V_m^{*2}}{2H_{p2}} \right) \\
&\quad \times \exp \left(\frac{X_{pmol}^2}{2H_{p4}} \right) \exp \left(-\frac{V_n^2}{2H_{p1}} \right) \exp \left[\frac{1}{2H_{p3}} \left(-\frac{iV_n \rho_0^{-4}}{H_{p2} H_{p1}} \right. \right. \\
&\quad \left. \left. - \frac{V_m^* \rho_0^{-2} \rho_{\chi s}^{-2}}{H_{p2} H_{p1}} + \frac{iV_m^* \rho_0^{-2}}{H_{p2}} - iV_\ell + \frac{V_n \rho_0^{-4} \rho_{\chi s}^{-2}}{H_{p2} H_{p1}^2} + \frac{V_n \rho_{\chi s}^{-2}}{H_{p1}} \right)^2 \right],
\end{aligned} \tag{5.18}$$

where

$$\begin{aligned}
X_{pnmol} = & \left[\left(\frac{\rho_0^{-2}}{H_{p2}H_{p1}\rho_0^2} - \frac{R_p}{H_{p2}} \right) \left(\frac{T_p\rho_0^{-2}}{H_{p1}} + \rho_0^{-2} \right) + \left(\frac{T_p\rho_0^{-2}}{H_{p1}} + \rho_0^{-2} \right) \right] \\
& \times \frac{i}{H_{p3}} \left[\frac{1}{H_{p2}} \left(\frac{T_p\rho_0^{-2}}{H_{p1}} + \rho_0^{-2} \right) \left(V_m^* - \frac{V_n\rho_0^{-2}}{H_{p1}} \right) - \frac{T_p V_n}{H_{p1}} - V_\ell \right] \\
& + \frac{i}{H_{p2}} \left(\frac{1}{H_{p1}\rho_0^2} \rho_0^{-2} - R_p \right) \left(V_m^* - \frac{V_n\rho_0^{-2}}{H_{p1}} \right) - \frac{i\rho_0^{-2}}{H_{p1}} V_n + iV_o^*.
\end{aligned} \tag{5.19}$$

The 3rd part of the integration is calculated as

$$\begin{aligned}
\langle I^2(\mathbf{p}, L) \rangle_{p=3} = & \frac{\pi^4}{(\lambda L)^4} \sum_{n=1}^N \sum_{m=1}^N \sum_{\ell=1}^N \sum_{o=1}^N A_n A_m^* A_\ell A_o^* \frac{2\sigma_\chi^2}{H_{p1}H_{p2}H_{p3}H_{p4}} \\
& \times \exp\left(\frac{X_{pnmol}^2}{2H_{p4}} \right) \exp\left[-\frac{1}{2H_{p2}} \left(V_m^* - \frac{V_n\rho_0^{-2}}{H_{p1}} \right)^2 \right] \\
& \times \exp\left(-\frac{V_n^2}{2H_{p1}} \right) \exp\left\{ -\frac{1}{2H_{p3}} \left[\frac{1}{H_{p2}} \left(\frac{T_p\rho_0^{-2}}{H_{p1}} + \rho_0^{-2} \right) \right. \right. \\
& \left. \left. \times \left(V_m^* - \frac{V_n\rho_0^{-2}}{H_{p1}} \right) - \frac{V_n T_p}{H_{p1}} - V_\ell \right]^2 \right\}.
\end{aligned} \tag{5.20}$$

If these equations are summarized,

$$\langle I^2(\mathbf{p}, L) \rangle = \sum_{p=1}^3 \sum_{n=1}^N \sum_{m=1}^N \sum_{\ell=1}^N \sum_{o=1}^N A_n A_m^* A_\ell A_o^* M_{pnmol}, \tag{5.21}$$

where

$$\begin{aligned}
M_{pnmol} = & \left(\frac{\pi}{\lambda L} \right)^4 \frac{1}{H_{p4} H_{p3} H_{p2} H_{p1}} \exp \left[-\frac{1}{2H_{p2}} \left(V_m^* - \frac{V_n \rho_0^{-2}}{H_{p1}} \right)^2 \right] \\
& \times \exp \left\{ -\frac{1}{2H_{p3}} \left[\frac{1}{H_{p2}} \left(\frac{T_p \rho_0^{-2}}{H_{p1}} + \rho_0^{-2} \right) \left(V_m^* - \frac{V_n \rho_0^{-2}}{H_{p1}} \right) - \frac{V_n T_p}{H_{p1}} - V_\ell \right]^2 \right\} \quad (5.22) \\
& \times \exp \left(-\frac{V_n^2}{2H_{p1}} \right) \exp \left(\frac{X_{pnmol}}{2H_{p4}} \right).
\end{aligned}$$

Our analytical solution is validated by using Ref. [105] for the Gaussian, cosine-Gaussian and cosine-hyperbolic Gaussian beams.

5.2 Results for Scintillation of Cosine-Gaussian beam in Underwater

Figure 52 demonstrates the influence of the underwater turbulence on scintillation index of cos-Gaussian beam for different rate of dissipation of kinetic energy per unit mass of fluid ε versus source size. It is observed that for any value of the rate of dissipation of kinetic energy per unit mass of fluid, as the source size α_s increases, scintillation index first increases then at larger source sizes, very small increase or no increase in the scintillations is observed. Figure 52 also shows that with increasing the rate of dissipation of kinetic energy per unit mass of fluid ε , scintillation index decreases. Increasing ε means that the turbulence strength decreases since less kinetic energy causes to decrease the turbulent motion. In turn, smaller turbulence strength provides smaller scintillation index.

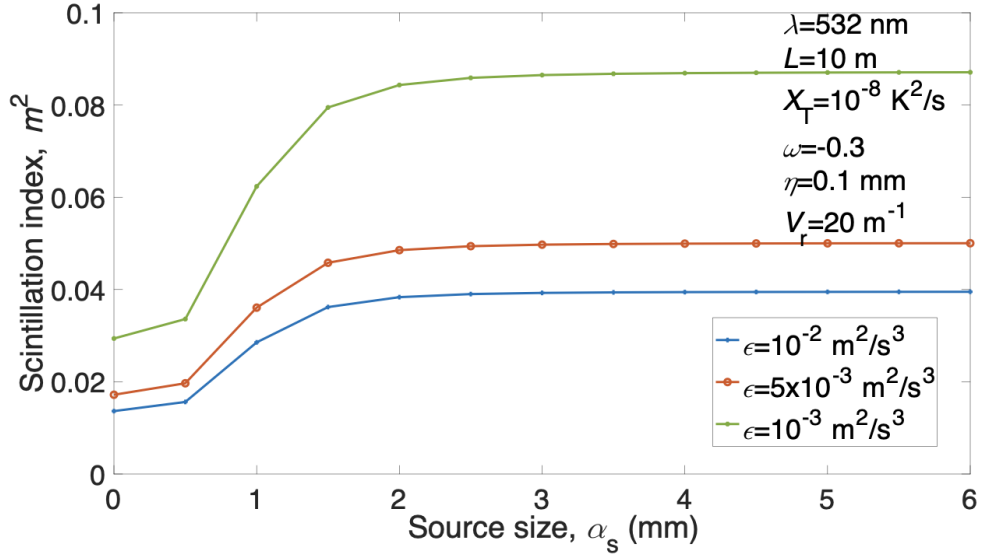


Figure 52 Scintillation index of cos-Gaussian beam versus the source size α_s for different ϵ .

Figure 53 shows the scintillation index versus the source size α_s for different ω . The temperature-induced optical turbulence ($\omega = -5$) has almost no effect on the turbulence, so we cannot observe scintillations. However, the salinity-induced optical turbulence causes large increase in the scintillation index especially in the interval $[-0.5, 0]$ for all ω and α_s values. Salt dissolved in seawater is quantified as the salinity. Increase in salinity increases the density because of the increase in the mass of salt. Salinity induced turbulence affects the scintillation index dramatically. When the temperature is increased, dissolved salt decreases, which causes the density and salinity to decrease. Thus, temperature induced turbulence becomes effective in this condition so this range of ω $[-0.5, 0]$ is used in our observation. If ω is closer the zero, we observe larger scintillations. In Figure 53, the observation is that if α_s is smaller, the scintillation index is smaller.

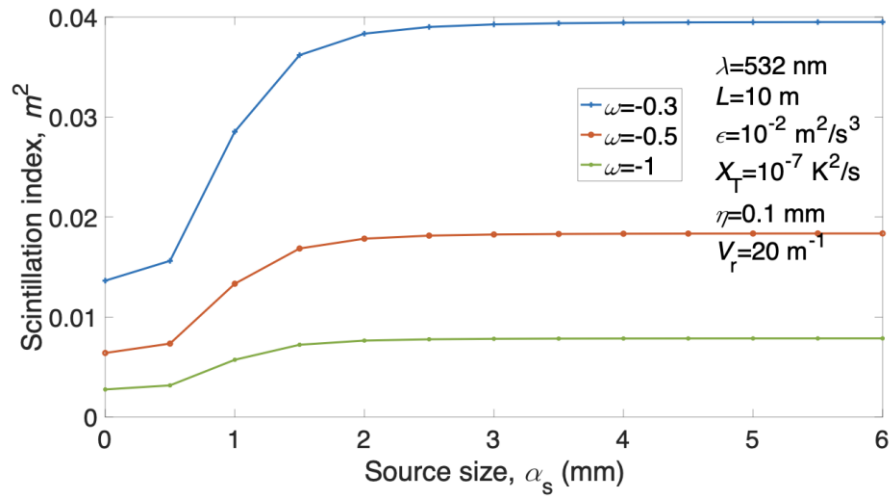


Figure 53 Scintillation index of cos-Gaussian beam versus the source size α_s for different ω .

In Figure 54, the scintillation index of cos-Gaussian beam versus source size values for different displacement parameters is shown. The results from Figure 54 indicate that when the displacement parameter increases, the scintillation index increases after the source size is larger than 2 mm. Figure 54 also shows that for any value of the displacement parameters, larger source size yields a larger scintillation index in the underwater medium.

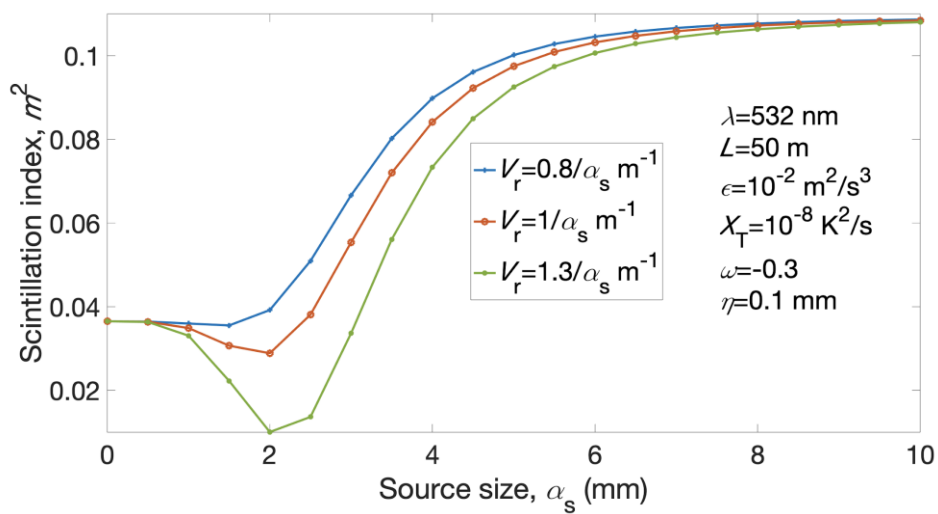


Figure 54 Scintillation index of cos-Gaussian beam versus the source size α_s for different V_r .

In Figure 55, we can understand that when the rate of dissipation of kinetic energy per unit mass of fluid ϵ increases, the intensity fluctuation decreases. This is because increasing ϵ results in decreasing oceanic turbulence strength. If we observe the scintillation index at a fixed ϵ value in Figure 55, increase in the displacement parameter is seen to cause the scintillation index to decrease because of the beam shape of cos-Gaussian. Increasing displacement parameter for cos-Gaussian means that cos-Gauss beam has more beamlets. To observe a change in the scintillations in this condition, we need to choose big differences in V_r .

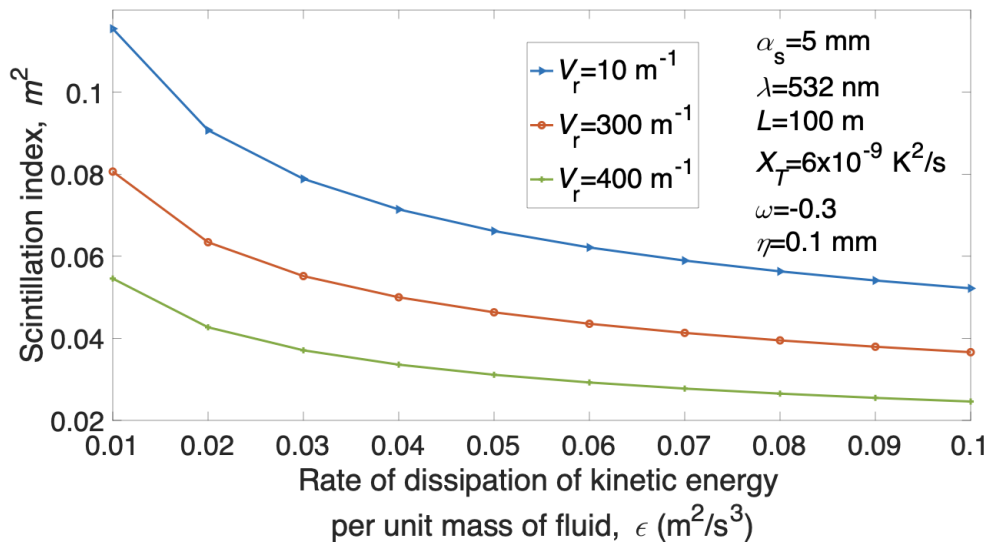


Figure 55 Scintillation index of cos-Gaussian beam versus the rate of dissipation of kinetic energy per unit mass of fluid ϵ for different V_r .

In Figure 56, the most effective range of ω (salinity induced turbulence effect) of oceanic turbulence is examined and we can observe the changes of intensity fluctuations clearly in this range. When ω increases, scintillation index increases. Figure 56 exhibits that at any value of ω , as ϵ becomes larger, the scintillation index becomes smaller.

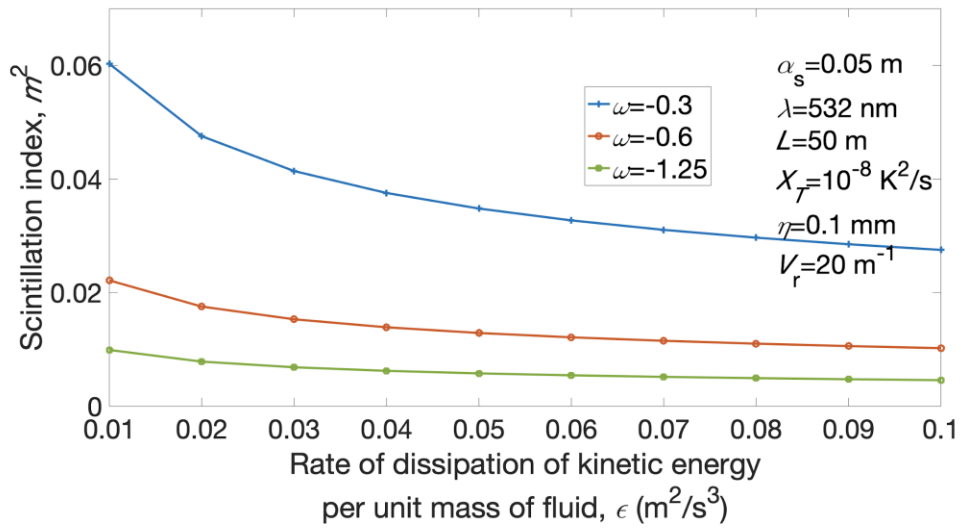


Figure 56 Scintillation index of cos-Gaussian beam versus the rate of dissipation of kinetic energy per unit mass of fluid ϵ for different ω .

In Figure 57, it is seen that the intensity fluctuations increase with increase in the propagation distance, as expected. At a fixed path length value, for larger wavelength, smaller scintillation index is observed.

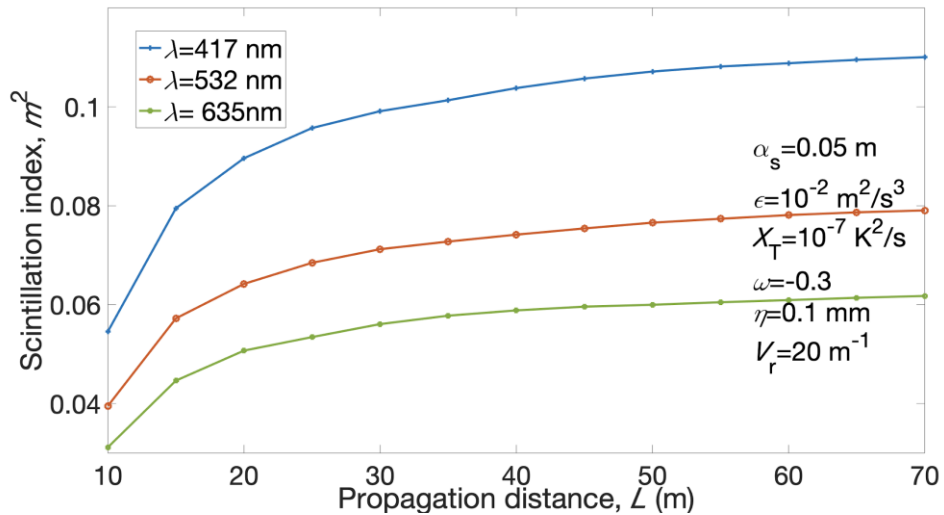


Figure 57 Scintillation index of cos-Gaussian beam versus the propagation distance L for different wavelengths λ .

In Figures 58 and Figure 59, the scintillation index is shown for the cos-Gaussian beam against the rate of dissipation of mean-square temperature χ_T , for different ε and ω . The lower values of χ_T indicates smaller strength of turbulence and the higher values of χ_T means strong turbulence. From Figures 58 and 59, it is seen that the scintillation index increases when χ_T becomes larger which is valid for all ε and ω values due to increasing turbulence effect. As seen in Fig. 58, being valid for all χ_T values, when ε becomes larger, the scintillation index becomes smaller. In Fig. 59, when χ_T is kept fixed, the scintillation index is larger for larger values of ω .

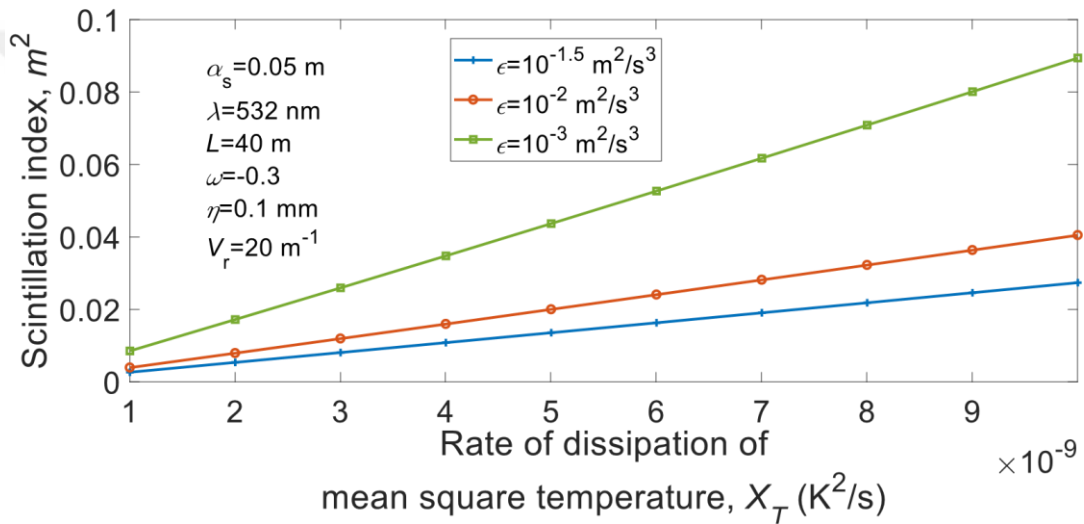


Figure 58 Scintillation index of cos-Gaussian beam versus the rate of dissipation of mean square temperature χ_T for different ε .

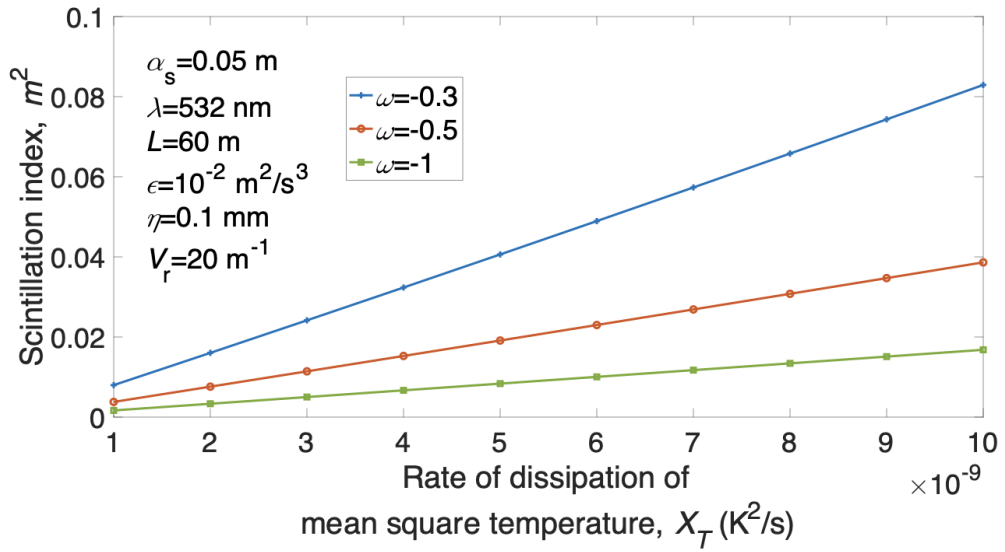


Figure 59 Scintillation index of cos-Gaussian beam versus the rate of dissipation of mean square temperature χ_T for different ω .

5.3 Results for Scintillation of Cosine-Hyperbolic Gaussian beam in Underwater

In Figure 60, in relation with the source size and the propagation distance, the scintillation index of the cosh-Gaussian beam is shown. We observe that as the propagation distance increases, the scintillation index increases for a fixed source size value. Naturally, this trend is similar to the cos-Gaussian beam. With an increase in the source size, the general trend of the scintillations for cosh-Gaussian beam is to increase.

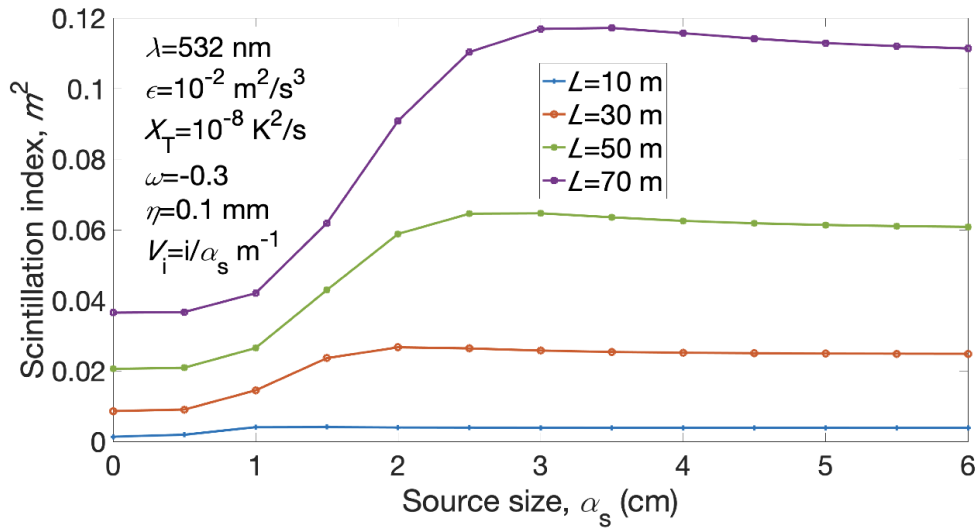


Figure 60 Scintillation index of cosh-Gaussian beam versus the source size α_s for different L .

Figure 61 is provided to observe the variations of the scintillation index of cosh-Gaussian versus the source size α_s for different values of V_i . Displacement parameters are chosen as source size dependent. For larger displacement parameter, scintillation index increases for the cosh-Gaussian beam unlike for the cos-Gaussian beam. In the chosen range of the source size (0.5 – 3 mm), increasing the source size increases the intensity fluctuations but source sizes larger than 3 mm cause a decrease in the intensity fluctuations or no change is observed depending on the displacement value. When ω is close to zero, turbulence effect increases and the scintillation index increases, which is valid for all α_s values in Figure 62. Examining Figures 62 and 63, it is seen that larger values of α_s make the scintillation index in general to increase for the cosh-Gaussian beam. In Figure 63, at fixed α_s , larger ε will give smaller scintillation index.

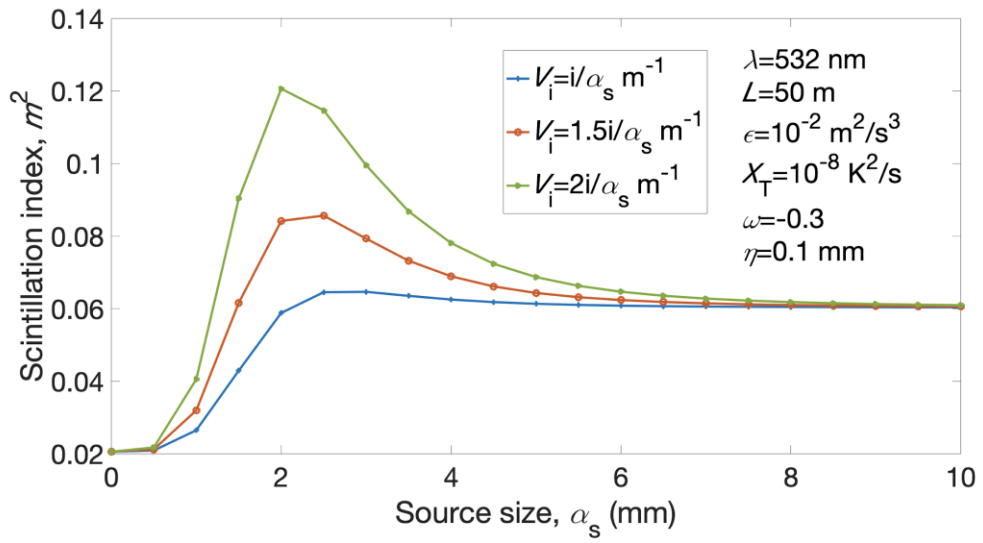


Figure 61 Scintillation index of cosh-Gaussian beam versus the source size α_s for different V .

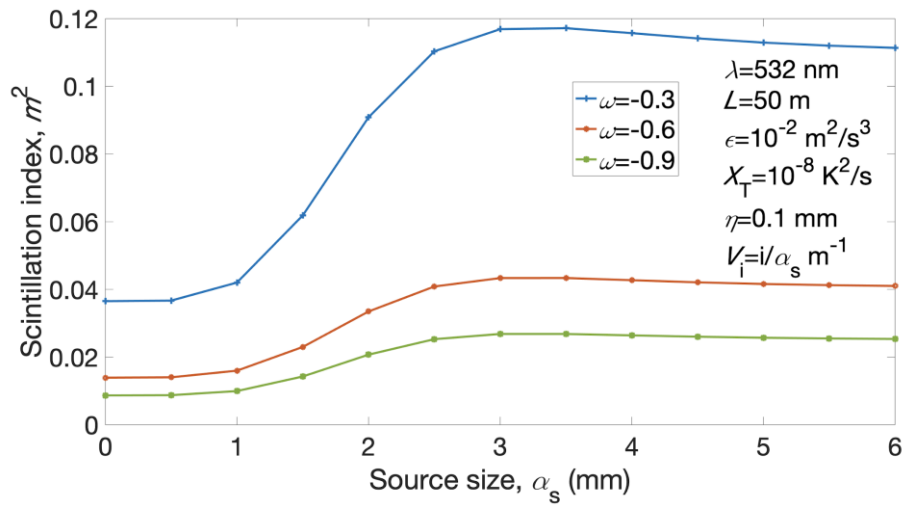


Figure 62 Scintillation index of cosh-Gaussian beam versus the source size α_s for different ω .

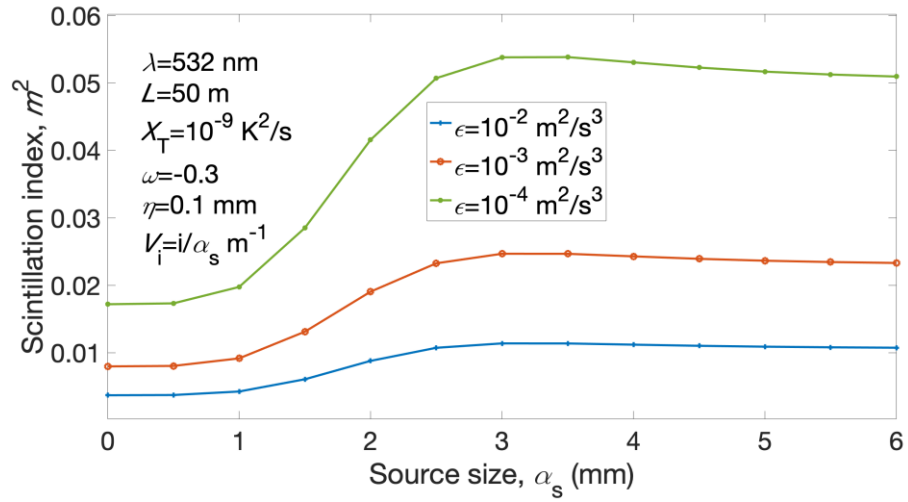


Figure 63 Scintillation index of cosh-Gaussian beam versus the source size α_s for different ε .

In Figure 64, the scintillation index versus the rate of dissipation of mean square temperature ε is examined for different displacement parameter V_i values. A decrease in the scintillation index is observed when ε becomes larger, which holds to be true for any V_i value. For the same ε , larger V_i for the cosh-Gaussian beam gives larger scintillation index.

Figure 65 indicates that for any value of the wavelength, larger χ_T yields larger scintillation index which can be explained physically by the fact that larger χ_T results in larger underwater turbulence strength. At the same χ_T , larger wavelength causes the scintillation index to reduce, as expected.

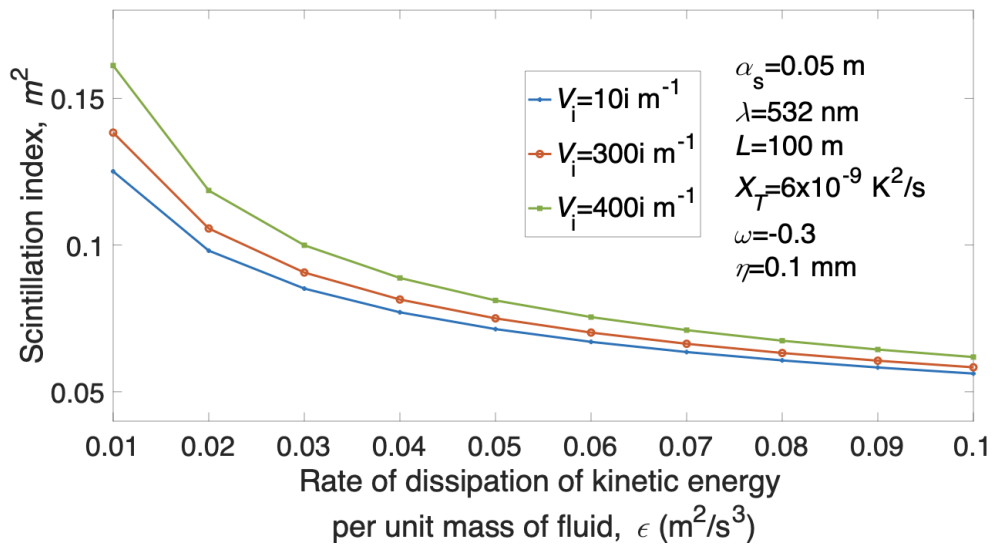


Figure 64 Scintillation index of cosh-Gaussian beam versus the rate of dissipation of kinetic energy per unit mass of fluid ϵ for different V .

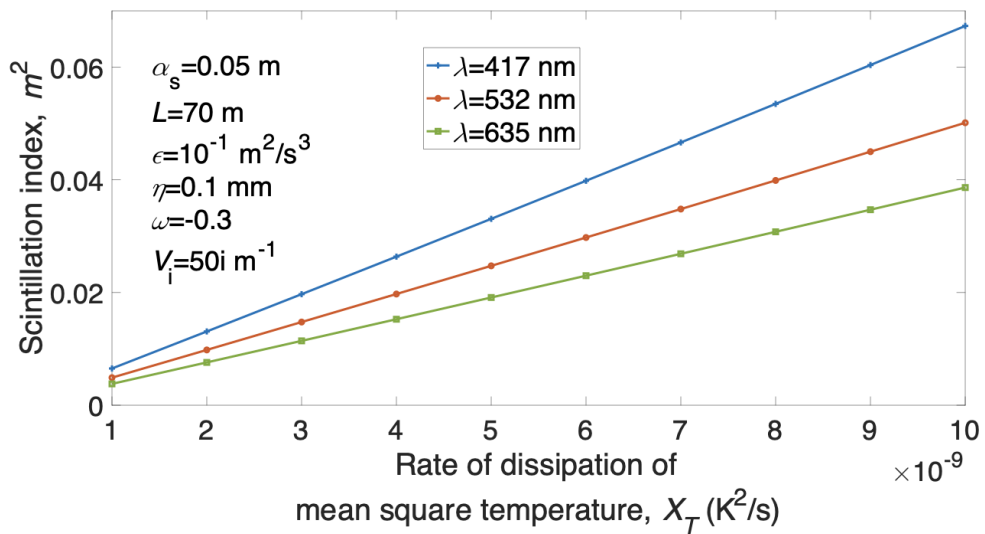


Figure 65 Scintillation index of cosh-Gaussian beam versus the rate of dissipation of kinetic energy per unit mass of fluid ϵ for different wavelengths.

5.4 Comparison of Cosine Gaussian Beam and Cosine-Hyperbolic Gaussian Beam Scintillation in Underwater Medium

Figure 66 is provided to compare the scintillations of cos-Gaussian and cosh-Gaussian beams in underwater turbulence. Figure 66 shows that the scintillation index decreases for increasing small values of source sizes for the cos-Gaussian beam but then increases when α_s increases for a small range of α_s and after that the scintillation index stays at almost constant value for all propagation distance values. Again, in Figure 66, it is seen that the cosh-Gaussian beam behaves in an opposite trend when compared with the cos-Gaussian beam. At the same time, we can say that cosh-Gaussian beams have larger scintillations than the cos-Gaussian beam at the same condition in underwater turbulence.

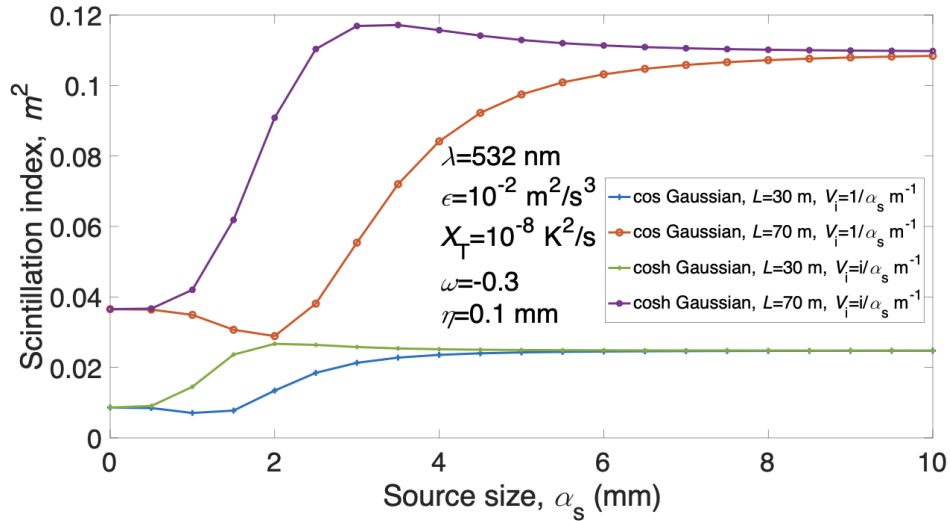


Figure 66 Comparison of the scintillation index of cos-Gaussian and cosh-Gaussian beam versus the source size α_s for different L .

To summarize the results in this section, the underwater turbulence effect increases the scintillation index when ω , χ_T increase and/or ϵ decreases for the cos and cosh-Gaussian beam as in the literature [77,80-81,84] for different beam types. The displacement parameter also has an effect on the intensity fluctuations for both cos-

Gaussian and cosh-Gaussian beams in turbulent ocean. Displacement parameter has opposite effects on the scintillations of cos-Gaussian and cosh-Gaussian beams. When the wavelength increases, the scintillation index of both cos and cosh Gaussian beam decreases. In the literature, the same results for multimode laser beam [80], plane and spherical beam [77] are seen.

To analyze the effect of the underwater turbulence on the scintillation index of cos-Gaussian and cosh-Gaussian beam waves propagating the underwater medium, we assume that the power spectrum of underwater turbulence is homogeneous and isotropic. In our analysis, we use the extended Huygens-Fresnel principle and the equivalent structure constant. Our results indicate that when the displacement parameter of the cos-Gaussian beam is small, the intensity fluctuation is larger in the underwater turbulent medium. This is in contrast with the scintillation index variations for the cosh-Gaussian beams in which an increase in the displacement parameter will increase the scintillation index. χ_T and ω have similar effects on the scintillation index, that is, for all the cos-Gaussian and cosh-Gaussian optical beams, increase in χ_T and/or ω will result in an increase in the scintillation index. However, for ε , this relation is just the opposite, i.e., for all the cos-Gaussian and cosh-Gaussian optical beams, an increase in ε will result in a decrease in the scintillation index. With the increase in the wavelength, decrease in the intensity fluctuations is observed for both cos and cosh Gaussian beam waves. As the propagation distance increases, scintillation index increases. Opposite source size effect is observed for cos and cosh Gaussian beam waves. While the scintillation index decreases for very small values of α_s for cos-Gaussian beam, it increases for cosh-Gaussian beam. Then as α_s gets larger, the scintillation index increases for the cos-Gaussian beam whereas it decreases or stays steady for the cosh-Gaussian beam.

CHAPTER 6

BIT ERROR RATE (BER)

6.1 Methodology of Bit Error Rate

In oceanic turbulence using on-off keying (OOK) modulation BER is formulated as given below [131-132]

$$BER = 0.5 \int_0^{\infty} p_I(u) \operatorname{erfc}\left(\frac{SNR}{2\sqrt{2}}u\right) du, \quad (6.1)$$

where $\operatorname{erfc}(\cdot)$ indicates the complementary error function, SNR is the average signal to noise ratio, u is the normalized signal with unity mean and $p_I(u)$ is the log-normal probability density function of intensity, which is given by [131-132]

$$p_I(u) = \frac{1}{um\sqrt{2\pi}} \exp\left\{-\frac{[\ln(u) + 0.5m^2]^2}{2m^2}\right\} \quad u > 0. \quad (6.2)$$

Here m^2 is the scintillation index. BER is calculated by the help of MATLAB program numerically and our results are checked with [131] for the symmetrical case.

6.2 Results for BER of Cosine Gaussian Beam

All the figures in this section show $\log(BER)$ versus SNR in dB (decibel) for important parameters of oceanic turbulence and displacement parameters of cos and

cosh-Gaussian beams. All the figures in this section reflect the analysis in the similar axis limit in the literature given in [128-132]. Feasible range of $\log(BER)$ and/or SNR limits the horizontal and the vertical axis. It is observed from all the figures in this section, as expected, when SNR increases, BER decreases. Figure 67 shows the relations of BER and SNR for different rate of dissipation of kinetic energy for unit mass of fluid ε . Larger ε gives smaller BER due to the fact that increasing ε causes smaller strength turbulent oceanic medium. Consequently, better BER performance is obtained for lower oceanic turbulence.

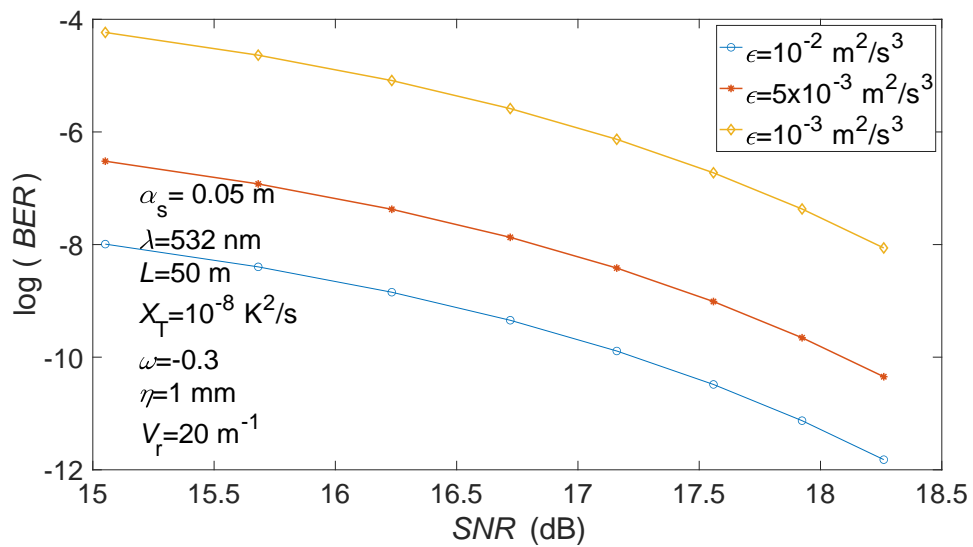


Figure 67 BER of cosine-Gaussian beam versus SNR in oceanic turbulence for various rates of dissipation of kinetic energy values.

In Figure 68, displacement parameter effect on the BER performance is analysed. It is observed that if the displacement parameter of cosine-Gaussian beam increases, better BER performance is observed for the cos-Gauss beam.

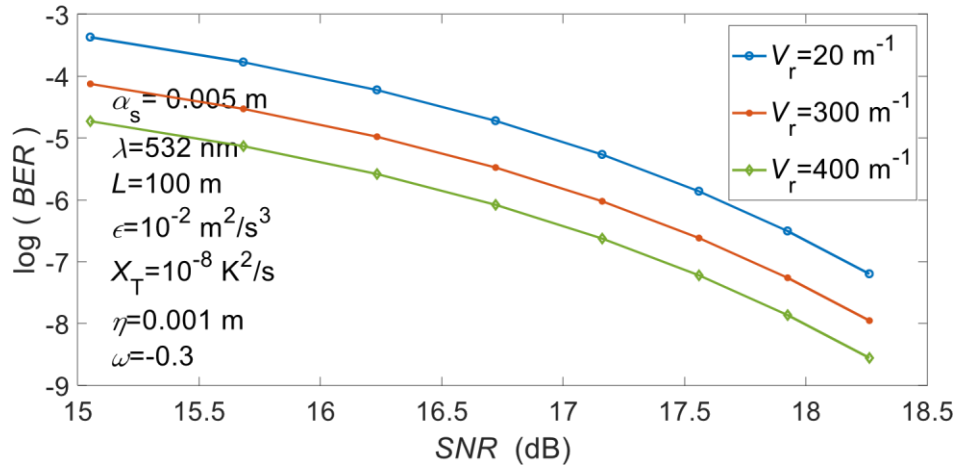


Figure 68 BER of cosine-Gaussian beam versus SNR in oceanic turbulence for various displacement parameters.

The result from Figure 69 is that larger ratio of temperature and salinity contributions ω exhibits larger BER because larger ω yields strong oceanic turbulence. In Figure 70, larger rate of dissipation of mean square temperature χ_T causes unfavourable BER performance since larger χ_T means larger oceanic turbulence.

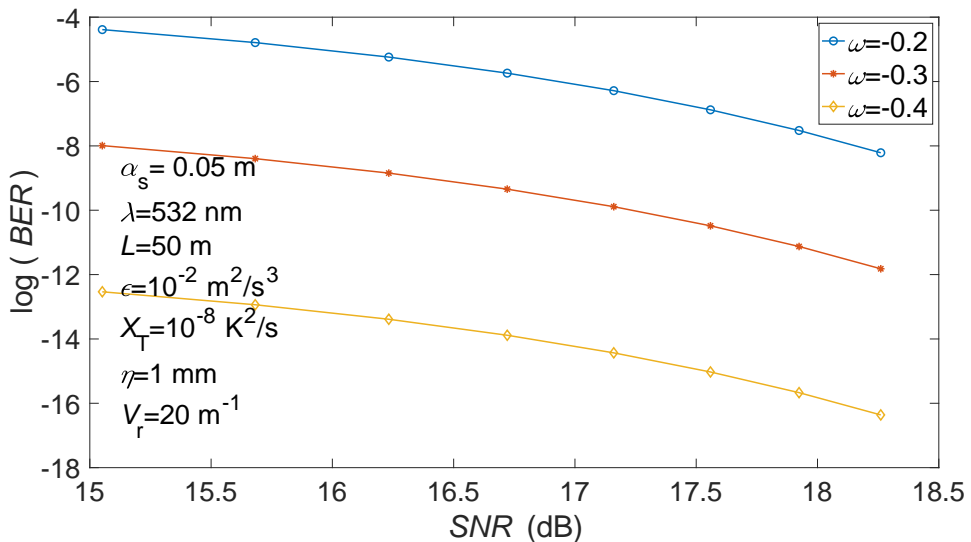


Figure 69 BER of cosine-Gaussian beam versus SNR in oceanic turbulence for various ratios of temperature and salinity contribution.

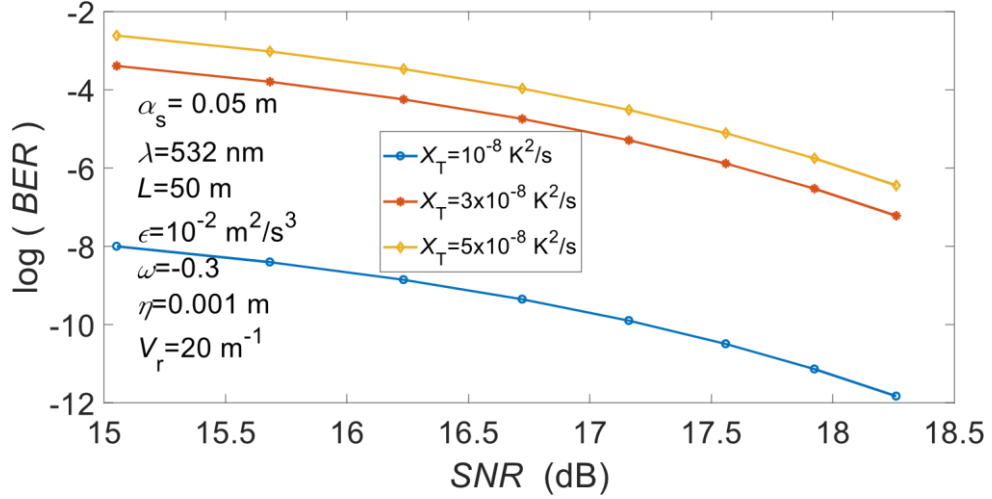


Figure 70 BER of cosine-Gaussian beam versus SNR in oceanic turbulence for various rates of dissipation of mean square temperature.

6.3 Results for BER of Cosine-Hyperbolic Gaussian Beam

Both Figure 71 and Figure 72 examine $\log(BER)$ versus SNR in dB for different rate of dissipation of kinetic energy ϵ . However, while in Figure 71 the complex displacement parameter of cosh-Gauss is a constant value, in Figure 72 displacement parameter is source dependent. These two figures show similar behavior on curves for all ϵ values. When the rate of dissipation of kinetic energy is larger, better BER performance is observed in Figures 71 and 72 for the cosh-Gauss beam as for the cos-Gauss beam.

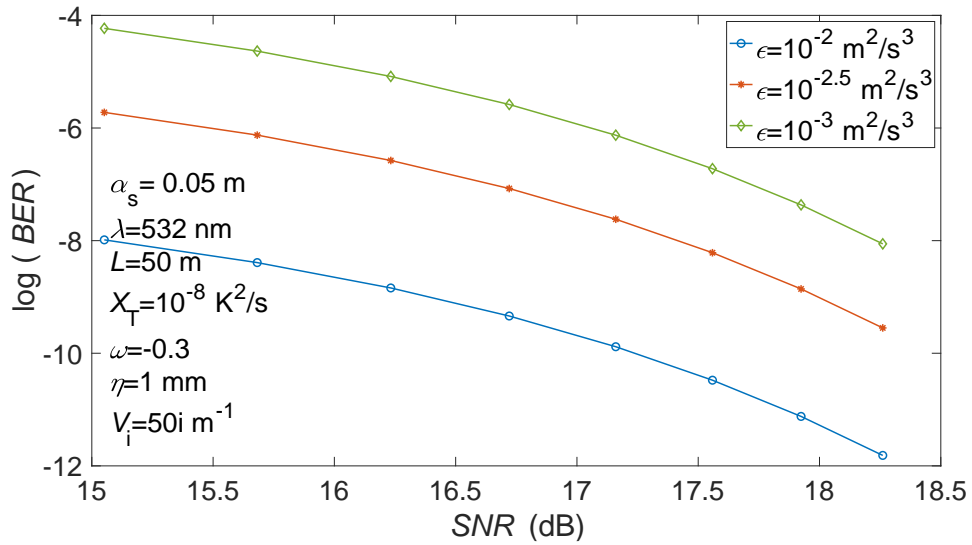


Figure 71 BER of cosine-hyperbolic Gaussian beam versus SNR in oceanic turbulence for various rates of dissipation of kinetic energy values.

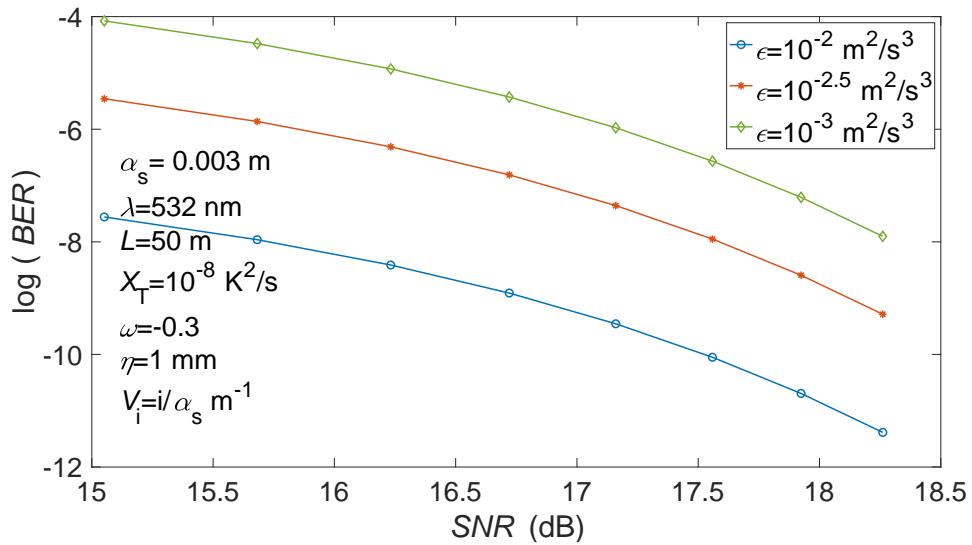


Figure 72 BER of cosine-hyperbolic Gaussian beam versus SNR in oceanic turbulence for various rates of dissipation of kinetic energy values.

In Figure 73, displacement parameters are chosen source size dependent to observe the BER clearly. When the displacement parameter increases, the beamlets of cosh-

Gauss beam move away from each other, so the beam is more influenced from underwater turbulence. Then, larger V_i yields larger BER values.

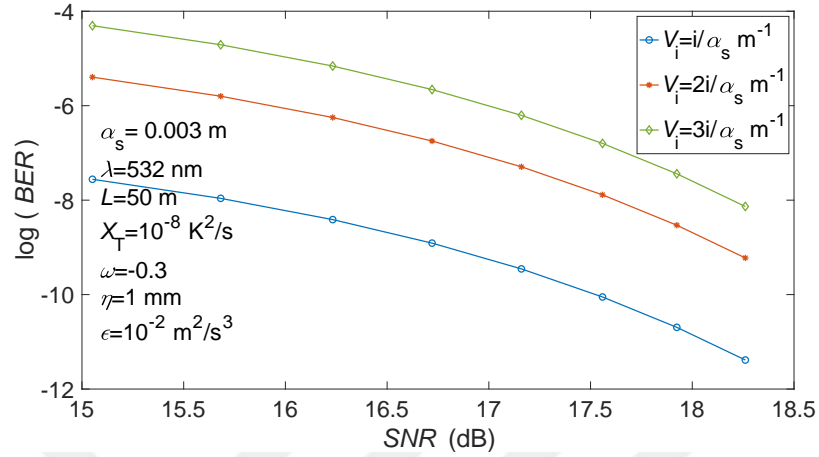


Figure 73 BER of cosine-hyperbolic Gaussian beam versus SNR in oceanic turbulence for various displacement parameters.

In Figures 74 and 75, BER versus SNR are observed with various ratio of temperature and salinity contributions ω and rate of dissipation of mean square temperature χ_T , respectively. Increasing both ω and χ_T cause stronger oceanic turbulence and stronger turbulence degrades BER substantially.

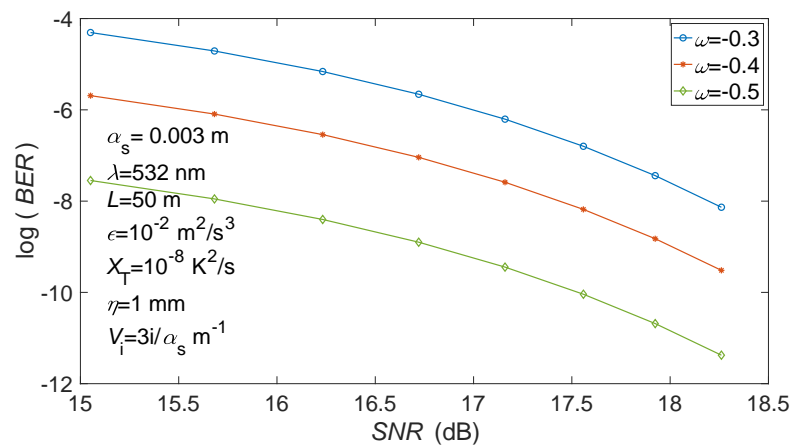


Figure 74 BER of cosine-hyperbolic Gaussian beam versus SNR in oceanic turbulence for various ratios of temperature and salinity contribution.

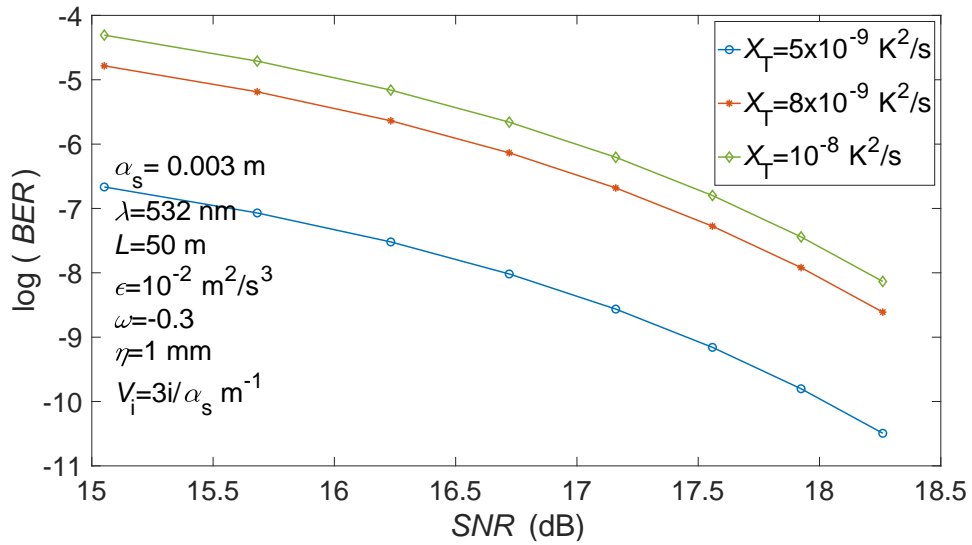


Figure 75 BER of cosine-hyperbolic Gaussian beam versus SNR in oceanic turbulence for various rates of dissipation of mean square temperature.

6.4 Comparison of Cosine & Cosine-Hyperbolic Gaussian Beams BER Performance

In section 6.2 and 6.3, BER performances of cos-Gaussian beam and cosh-Gaussian beam are given, respectively. We can understand from Figure 67 to Figure 75 that increasing ϵ exhibits decreasing BER while increasing ω and χ_T yields increasing BER. Again, this is because, decreasing ϵ and/or increasing ω and χ_T cause to increase the strength of oceanic turbulence. Stronger turbulence exhibits larger BER values. Displacement parameter shows opposite effects on the cos and cosh-Gaussian beams because of the beam shapes. If the displacement parameter increases, beamlets of cosh-Gaussian move away from each other and such beams are more affected from oceanic turbulence while the number of the beamlets of cos-Gaussian beam increases and are less affected from oceanic turbulence. Figure 76 shows the comparison of BER performance of cos and cosh-Gaussian beams at the same conditions for different propagation length. From Figure 76, it is seen that for all the

propagation distances, cosine Gaussian beam exhibits better *BER* performance than the cosine-hyperbolic Gaussian beam in weak oceanic turbulence.

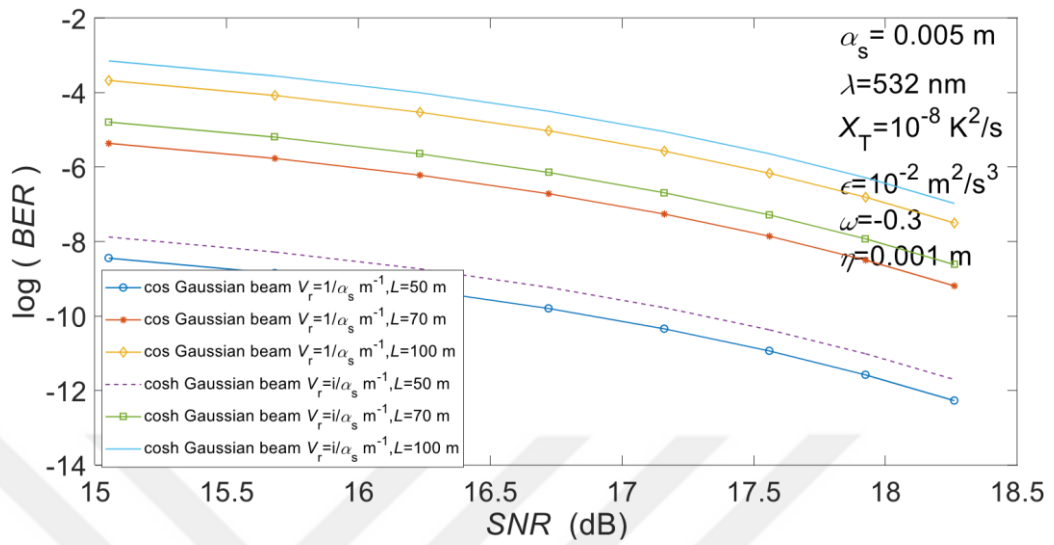


Figure 76 *BER* versus *SNR* in oceanic turbulence for comparison of the cosine and cosine-hyperbolic Gaussian beams.

CHAPTER 7

CONCLUSION

In this thesis, to improve the performance of UWOC system, the oceanic turbulence effect on the system performance parameters and different source beam types are analyzed. In turn, on-axis and off-axis average transmittance, beam spread, scintillation and BER have been examined for different beam types such as partially coherent flat topped, cos-Gaussian and cosh-Gaussian and partially coherent cos and cosh-Gaussian beams. In this study the extended Huygens-Fresnel principle has been used. Calculations were carried out by using the MATLAB program. We examine the effects of all the oceanic turbulent parameters, which are the rate of dissipation of mean square temperature χ_T , the ratio of the temperature and salinity contributions to the refractive index spectrum ω , the rate of dissipation of kinetic energy for the unit mass of fluid ε , and degree of partially coherence ρ_s , off-axis parameter r_x , complex displacement parameters V_r , V_i , number of Gaussian beams to produce the flat-topped beam N , source size α_s , propagation distance L and the wavelength λ .

It has been found that each oceanic turbulence parameters have similar effects on various performance entities. For instance, increase in χ_T and/or ω results in an increase in strength of oceanic turbulence and this trend is opposite for ε . For this reason, increasing χ_T and/or ω causes to decrease the average transmittance, to increase beam spread, scintillation index and BER while increasing ε results in increasing average transmittance, decreasing beam spread, decreasing scintillation index and BER.

In every situation we examine, larger λ gives larger average transmittance and smaller scintillation index. Moreover, propagation distance L decreases the average transmittance and increases the scintillation index. Besides, increase in source size yields larger transmittance for all beam types we examine. For the flat-topped beam, increasing N exhibits larger average transmittance and smaller beam spread. In addition, we examine the effects of the displacement parameters of cos and cosh-Gaussian beams for *BER* performance, scintillation index and average transmittance. It is found that if the displacement parameter increases, *BER* and scintillation index decreases for cos-Gaussian while increases for the cosh-Gaussian beam.

Other parameters studied are the degree of partially coherence and off-axis parameter. For all partially coherent beam types examined, which are partially coherent Gaussian, partially coherent flat-topped, partially coherent cos-Gaussian and partially coherent cosh-Gaussian, the average transmittance decreases with increasing ρ_s . However, an increase in ρ_s results in increasing the beam spread. If the beam is more coherent, it is more affected by oceanic turbulence. Off-axis average transmittance of Gaussian beam, flat-topped beam, cos and cosh-Gaussian beam and their partially coherent cases are studied. Obtained results show that the average transmittance of Gaussian, flat-topped and their partially coherent cases decrease with increasing r_x . However, the average transmittance of cos and cosh-Gaussian beams and their partially coherent forms increase with increasing r_x due to the beam shapes.

These results mentioned above are summarized in Table 1.

Table 1 Obtained results from figures.

	Transmittance			Beam Spread	Scintillation			BER	
	Flat-Topped	Cos-Gauss	Cosh-Gauss	Flat-Topped	Cos-Gauss	Cosh-Gauss	Cos-Gauss	Cosh-Gauss	
$\uparrow \varepsilon$	\uparrow	\uparrow	\uparrow	\downarrow	\downarrow	\downarrow	\downarrow	\downarrow	
$\uparrow \chi_T$	\downarrow	\downarrow	\downarrow	\uparrow	\uparrow	\uparrow	\uparrow	\uparrow	
$\uparrow \omega$	\downarrow	\downarrow	\downarrow	\uparrow	\uparrow	\uparrow	\uparrow	\uparrow	
$\uparrow \rho_s$	\downarrow	\downarrow	\downarrow	\uparrow	not examined	not examined	not examined	not examined	
$\uparrow r_x$	\downarrow	\uparrow	\uparrow	-	not examined	not examined	not examined	not examined	
$\uparrow V_l$	V=0	\downarrow	\uparrow	V=0	\downarrow	\uparrow	\downarrow	\uparrow	
$\uparrow N$	\uparrow	N=2	N=2	\downarrow	N=2	N=2	N=2	N=2	
$\uparrow L$	\downarrow	\downarrow	\downarrow	\uparrow	\uparrow	\uparrow	\uparrow	\uparrow	
$\uparrow \alpha_s$	\uparrow	\uparrow	\uparrow	\downarrow	\uparrow for small source sizes	\uparrow for small source sizes	\downarrow	\downarrow	
$\uparrow \lambda$	\uparrow	\uparrow	\uparrow	\downarrow	\downarrow	\downarrow	\downarrow	\downarrow	

When we compare the beam types according to the parameters examined, it is observed that the transmittance of partially coherent beams are larger than their coherent counterparts. In practical applications use of partially coherent sources is more general. Partially coherent flat-topped beam has the largest transmittance. The average transmittance of cosh-Gaussian beam is higher than cos-Gaussian beam. If the receiver can not be positioned at the center of the receiver plane for the designed link, cos and cosh-Gaussian beams are preferable for this type of applications. Off-axis parameter decreases the transmittance of flat-topped beam while it increases the transmittance of cosh and cos-Gaussian beam. Beam spread is analyzed only for the flat-topped beam in this thesis. Increasing and decreasing situations of the beam spread can be seen in Table 1. Additionally, we note that, increase in the beam spread is not always disadvantage. If the beam expands a lot at the receiver plane, the detector can catch the beam easily. Of course, more expanding beam has less power but if the application does not need much power, expanding beam can be more feasible. Normally, partially coherent beams expand more than the coherent beams.

However, in our study because of our definition, we observe that the coherent beam is expanding less due to oceanic turbulence. Actually, both statements are true. With our beam spread definition, which shows the differences between the beam sizes at the receiver plane after the propagation with turbulent medium and free space, we observe only oceanic turbulence effects on the beam spread. Coherent beams are less affected by turbulence and are less expanded. However, partially coherent beams have larger beam spread with the other propagation effects. Therefore, in power independent applications, partially coherent beams are more preferable in order not to miss the detector.

In our study, we have not examined the power dependent results for the transmittance. An increase and/or decrease on the power will result in an increase and/or decrease in the field amplitude, but there is no change on the transmittance because transmittance, which is a ratio, is defined as the normalized intensity.

Scintillation index and *BER* are examined for the cosine and cosine-hyperbolic Gaussian beams. Increasing (decreasing) scintillation index increases (decreases) *BER*. Scintillation index and *BER* of cosine-Gaussian beam are smaller than the scintillation index and *BER* of the cosine-hyperbolic Gaussian beam. Thus, cosine-Gaussian beam performs better in oceanic turbulence. Additionally, *BER* performance can be improved with increasing *SNR*.

In this thesis, it is aimed to make appropriate choices for the oceanic turbulent environment with examining the different beams and parameters. Obtained results can be used in the design of the underwater wireless optical communication links according to the needs. Expanding beams can be selected if it is intended to be easily captured by the detector. Alternatively, beams with increasing transmittance with the increase of off axis parameter can be selected. Depending on the application, in order to improve the performance of the designed underwater optical communication communication link, parameter values suitable for the medium can be obtained from our results.

REFERENCES

1. **Kaushal H., Kaddoum G., (2016)**, “*Underwater Optical Wireless Communication*”, IEEE Access, vol. 4, pp. 1518-1547.
2. **Spagnolo G. S., Cozzella L., Leccese F., (2020)**, “*Underwater Optical Wireless Communications: Overview*”, Sensors, vol. 20, 2261.
3. **Zhang Y., Wang Y., Huang A., Hu X., Han F., (2019)**, “*Influence of eddy diffusivity ratio on Gaussian beam under weak to strong oceanic turbulence*”, J. Mod. Opt., vol. 66, pp. 2063-2074.
4. **Brundage H., (2010)**, “*Designing a wireless underwater optical communication system*”, MSc. thesis, Massachusetts Institute of Technology, Cambridge, MA.
5. **Simson J., (2008)**, “*A 1Mb/s underwater communication system using LEDs and photodiodes with signal processing capability*”, MSc. thesis, North Carolina State University, Raleigh, NC.
6. **Duntley S. Q., (1963)**, “*Light in the Sea*”, J. Opt. Soc. Am. A, vol. 53, pp. 214-213.
7. **Doniec M., Xu A., Rus D., (2013)**, “*Robust Real-Time Underwater Digital Video Streaming using Optical Communication*”, In Proceedings of the IEEE Int. Conf. Robot (ICRA), Karlsruhe, Germany, pp. 5117-5124.
8. **Al-Halafi A., Oubei H.M., Ooi B.S., Shihada B., (2017)**, “*Real Time Video Transmission Over Different Underwater Wireless Optical Channels Using a Directly Modulated 520 nm Laser Diode*”, J. Opt. Commun. Netw., vol. 9, pp. 826-832.
9. **Ribas J., Sura D., Stojanovic M., (2010)**, “*Underwater wireless video transmission for supervisory control and inspection using acoustic OFDM*”, In Proceedings of the OCEANS-IEEE, Seattle, WA, USA.
10. **Han S., Chen R., Noh Y., Gerla M., (2014)**, “*Real-time video streaming from mobile underwater sensors*”, In Proceedings of the WUWTNET'14, the International Conference on Underwater Networks & Systems, Rome, Italy, pp. 1-8.

11. **Priyalakshmi B., Mahalakshmi K., (2020)**, “*Performance analysis of video transmission in vertical-UWOC link in mid-sea oil rig IoT systems*”, *J. Amb. Intel. Hum. Comp.*, doi: 10.1007/s12652-020-02081-0.
12. **Arnon S., Kedar D., (2009)**, “*Non-line-of-sight underwater optical wireless communication network*”, *J. Opt. Soc. Am. A*, vol. 26, pp. 530-539.
13. **Liu L., Zhou S., Cui J. H., (2008)**, “*Prospects and problems of wireless communication for underwater sensor networks*”, *Wirel. Commun. Mob. Com.*, vol. 8, pp. 977-994.
14. **Caiti A., Calabrò V., Munafò A., Dini G., Lo Duca A., (2013)**, “*Mobile Underwater Sensor Networks for Protection and Security: Field Experience at the UAN11 Experiment*”, *J. Field Robot.*, vol. 30, pp. 237-253.
15. **Arnon S., (2010)**, “*Underwater Optical Wireless Communication Network*”, *Opt. Eng.*, 49, 015001.
16. **Zeng Z., Fu S., Zang H., Dong Y., Cheng J., (2017)**, “*A survey of underwater optical wireless communications*”, *IEEE Comm. Surv. Tut.*, vol. 19, pp. 204-238.
17. **Johnson L. J., Jasman F., Green R. J., Leeson M. S., (2014)**, “*Recent advances in underwater optical wireless communications*”, *Underwater Technol.*, vol. 32, pp. 167-175.
18. **Saeed N.; Çelik A.; Al-Naffouri T. Y.; Alouini M. S.; (2019)**; “*Underwater optical wireless communications, networking, and localization: A survey*”; *Ad Hoc Netw.*, vol. 94, 101935.
19. **Jamali M. V., Mirani A., Parsay A., Abdolhassani B., Nabavi P., Chizari A., Khorramshahi P., Abdollahramezani S., Salehi J. A., (2018)**, “*Statistical Studies of Fading in Underwater Wireless Optical Channels in the Presence of Air Bubble, Temperature, and Salinity Random Variations*”, *IEEE T. Commun.*, vol. 66, pp 4706-4723.
20. **Keskin A., (2013)**, “*Wireless optical wave propagation in underwater medium*”, MSc. Thesis, Çankaya University, Ankara, Turkey.
21. **Oubei H. M., et. al., (2018)**, “*Light based underwater wireless communications*”, *Jpn. J. Appl. Phys.*, vol. 57, pp. 08PA06/1-18.
22. **Sharifzadeh M., Ahmadirad M., (2018)**, “*Performance analysis of underwater wireless optical communication systems over a wide range of optical turbulence*”, *Opt. Commun.*, vol. 427, pp. 609-616.
23. **Smart J. H. (2005)**, “*Underwater Optical Communications Systems Part 1: Variability of Water Optical Parameters*”, *IEEE Milit. Commun. C. (MILCOM 2005)*, Atlantic City, NJ.

24. **Conhenour B. M., Mullen L. J., Laux A. E. (2008)**, “*Characterization of the beam-spread function for underwater wireless communications links*”, IEEE J. Oceanic Eng., vol. 33, pp. 513-521.
25. **Hanson F., Radic S., (2008)**, “*High bandwidth underwater optical communication*”, Appl. Opt., vol. 47, pp. 277-283.
26. **Gabriel C., Khalighi M. A., Bourennane S., Leon P., Rigaud V, (2011)**, “*Channel Modeling for Underwater Optical Communication*”, IEEE GLOBECOM Workshops, Houston, TX.
27. **Mobley C., (1994)**, “*Light and Water*”, Academic Press/Elsevier Science, San Diego, CA.
28. **Vali Z., Gholami A., Ghasseemlooy Z., Michelson D. G., (2019)**, “*System Parameters Effect on the Turbulent Underwater Optical Wireless Communications Link*”, Optik, vol. 198, 163153.
29. **Wu Y., Zhang Y., Zhu Y., (2016)**, “*Average intensity and directionality of partially coherent model beams propagating in turbulent ocean*”, J. Opt. Soc. Am. A, vol. 33, pp. 1451-1458.
30. **Wang Z., Lu L., Zhang P., Qiao C., Zhang J., Fan C., Ji X., (2018)**, “*Laser Beam Propagation through Oceanic Turbulence*”, IntechOpen, <http://dx.doi.org/10.5772/intechopen.76894>.
31. **Nikishov V. V., Nikishov V. I., (2000)**, “*Spectrum of turbulent fluctuation of the sea water refractive index*”, Int. J. Fluid Mech. Res., vol. 27, pp. 82-98.
32. **Korotkova O., (2019)**, “*Light Propagation in a Turbulent Ocean*”, Prog. Optics, vol. 64, pp. 1-43.
33. **Farwell N., Korotkova O., (2012)**, “*Intensity and coherence properties of light in oceanic turbulence*”, Opt. Commun., vol. 285, pp. 872-875.
34. **Baykal Y. K., (2016)**, “*Optical Propagation in Unguided Media*”, Sig. Com. Tec., pp. 25-45.
35. **Liu D., Chen L., Wang Y., Wang G., Yin H., (2016)**, “*Average intensity properties of flat-topped vortex hollow beam propagating through oceanic turbulence*”, Optik, vol.127, pp. 6961-6969.
36. **Liu D., Wang Y., (2014)**, “*Evolution behavior of Gaussian-Shell model vortex beams propagating through oceanic turbulence*”, Opt. Express, vol. 22, pp. 17723-17734.
37. **Liu D., Wang Y., Zhong H., (2018)**, “*Average intensity of radial phase-locked partially coherent standard Hermite-Gaussian beam in oceanic turbulence*”, Opt. Laser Technol., vol. 106, pp. 495-505.

38. **Liu D., Wang Y., (2018)**, “Average intensity of partially coherent Lorentz beams in oceanic turbulence”, Prog. Electromagn. Res. M., vol. 68, pp. 181-191.
39. **Liu D., Wang G., Wang Y., (2017)**, “Average intensity and coherence properties of a partially coherent Lorentz-Gauss beam propagating through oceanic turbulence”, Opt. Laser Technol., vol. 98, pp. 309-317.
40. **Liu D., Wang Y., (2017)**, “Average intensity of a Lorentz beam in oceanic turbulence”, Optik, vol. 144, pp. 76-85.
41. **Liu D., Wang G., Wang Y., Yin H., Zhong H., (2019)**, “Radial phased-locked multi-Gaussian Schell-model beam array and its properties in oceanic turbulence”, Opt. Laser Technol., vol. 124, 106003.
42. **Liu D., Wang Y., (2018)**, “Properties of a random electromagnetic multi-Gaussian Schell-model vortex beam in oceanic turbulence”, Appl. Phys. B, vol. 124, no. 176.
43. **Liu D., Wang G., Yin H., Zhong H., Wang Y., (2019)**, “Propagation properties of a partially coherent anomalous hollow vortex beam in underwater oceanic turbulence”, Opt. Commun., vol. 437, pp.346-354.
44. **Liu D., et. al., (2019)**, “Average intensity of a partially coherent anomalous hollow beam propagating in underwater oceanic turbulence”, Opt. Appl., vol. 49, pp. 227-239.
45. **Liu D., Wang Y., Wang G. Yin H. M (2018)**, “Influences of oceanic turbulence on Lorentz Gaussian beam”, Optik, vol. 154, pp. 738-747.
46. **Yousefi M., (2017)**, “Analyzing the average intensity distribution and beam width evolution of phase-locked partially coherent radial flat-topped array laser beams in oceanic turbulence”, Laser Phys., vol. 27, pp. 1-14.
47. **Peng X. F., et. al., (2017)**, “Statistical properties of a radially polarized twisted Gaussian Schell-model beam in an underwater turbulent medium”, J. Opt. Soc. Am. A., vol. 34, pp. 133-139.
48. **Wu Y., Zhang Y., Hu Z.D., (2017)**, “Effects of oceanic turbulence on the propagation of four-petal Gaussian model beams”, Optik, vol. 129, pp. 93-99.
49. **Lu L., Wang Z., Zhang J., Zhang P., Qiao C., Fan C., Ji X., (2015)**, “Average intensity of $M \times N$ gaussian array beams in oceanic turbulence”, Appl. Opt., vol. 54, pp. 7500-7507.
50. **Zhang J., et. al., (2018)**, “Effects of the turbulent atmosphere and the oceanic turbulence on the propagation of a rotating elliptical Gaussian beam”, Appl. Phys. B, vol. 124, no. 168.

51. **Huang X., Deng Z., Shi X., Bai Y., Fu X., (2018)**, “Average intensity and beam quality of optical coherence lattices in oceanic turbulence with anisotropy”, *Opt. Express*, vol. 26, pp. 4786-4797.
52. **Zhi D., Chen Y. Z., Tao R. M., Ma Y. X., Zhou P., Si L., (2015)**, “Average spreading and beam quality evolution of Gaussian array beams propagating through oceanic turbulence”, *Laser Phys. Lett.*, vol. 12, 116001.
53. **Li Y., Han Y., Cui Z., (2019)**, “On-axis average intensity of a hollow Gaussian beam in turbulent ocean”, *Opt. Eng.*, vol. 58, 096115.
54. **Luo B., et. al., (2018)**, “Propagation of optical coherence lattices in oceanic turbulence”, *Opt. Commun.*, vol. 425, pp. 80-84.
55. **Chu X., Qiao C., Feng X., (2011)**, “Average intensity of flattened Gaussian beam in non-Kolmogorov turbulence”, *Opt. Laser Technol*, vol. 43, pp. 1150-1154.
56. **Eyyuboğlu H. T., Baykal Y., (2004)**, “Cosine-Gaussian laser beam intensity in turbulent atmosphere”, *Proc. SPIE*, vol.5743, pp. 131-141.
57. **Eyyuboğlu H. T., Baykal Y., (2005)**, “Average intensity and spreading of cosh-Gaussian laser beams in the turbulent atmosphere”, *App. Optics*, vol. 44, pp. 976-983.
58. **Wang F., Cai Y., (2008)**, “Experimental generation of a partially coherent flat-topped beam”, *Opt. Lett.*, vol. 33, no. 16.
59. **Keskin A., Baykal Y., Ata Y., (2014)**, “Optical transmittance in turbulent underwater medium”, *Proc. Çankaya Univ., Eng. Tech. Sym.*, vol. 7, pp. 137-141.
60. **Symth W. D., Moun J. N., (2001)**, “3D Turbulence”, College of Oceanic and Atmospheric Sciences Oregon State University, Academic Press, doi:10.1006/rwos.2001.0134.
61. **Keskin A., Baykal Y., (2019)**, “Off-axis average transmittance and beam spread of a partially coherent flat-topped beam in a turbulent underwater medium”, *J. Opt. Soc. Am. A.*, vol. 36, pp. 1287-1294.
62. **Keskin A., Baykal Y., (2020)**, “Effects of underwater turbulence on average transmittance of cos-Gaussian and cosh-Gaussian optical beams”, *Wave Random Complex*, doi. 10.1080/17455030.2020.1743894.
63. **Deng S., Yang D., Zheng Y., Hu L., Zhang, Y., (2014)**, “Transmittance of finite-energy frozen beams in oceanic turbulence”, *J. Opt. Soc. Am. A.*, vol. 31, pp. 1552-1556.

64. **Liang Q., Zhang Y., Yang D., (2020)**, “*Effects of Turbulence on the Vortex Modes Carried by Quasi-Diffracting Free Finite Energy Beam in Ocean*”, J. Mar. Sci. Eng., vol. 8, no. 458.
65. **Ata Y., Baykal Y., (2018)**, “*Anisotropy effect on multi-Gaussian beam propagation in turbulent ocean*”, Chin. Opt. Lett., vol. 16, 080102.
66. **Keskin A., Çatmakaş O. K., Genç F., Baykal Y., Arpali S. A., Arpali C., (2015)**, “*Effects of Focused and Collimated Laser Beams on the Performance of Underwater Wireless Optical Communications*”, International Workshop on Opt. Wireless Commun., Istanbul, Turkey, pp. 41-45.
67. **Ata Y., Baykal Y., (2017)**, “*Flat-topped beam transmittance in anisotropic non-Kolmogorov turbulent marine atmosphere*”, Opt. Eng., vol. 56, 104107.
68. **Ata Y., Baykal Y., (2015)**, “*Transmittance of multi Gaussian optical beams for uplink applications in atmospheric turbulence*”, IEEE J. Sel. Area Comm., vol. 33, pp. 1996-2001.
69. **Ata Y., Baykal Y., (2011)**, “*Turbulence effect on transmittance of atmospheric optics telecommunication system using dense wavelength division multiplexing*”, J. Mod. Opt., vol. 48, pp. 1644-1650.
70. **Ata Y., Baykal Y., (2013)**, “*Average transmittance in non-Kolmogorov turbulence*”, Opt. Commun., vol. 305, pp. 126-130.
71. **Eyyuboğlu H. T., Baykal H., (2007)**, “*Transmittance of partially coherent cosh-Gaussian, cos-Gaussian and annular beams in turbulence*”, Opt. Commun., vol. 278, pp. 17-22.
72. **Baykal Y., (2004)**, “*Average transmittance in turbulence for partially coherent sources*”, Opt. Commun., vol. 231, pp. 129-136.
73. **Korotkova O., Farwell N., Shchepakina E., (2012)**, “*Light scintillation in oceanic turbulence*”, Wave Random Complex, vol. 22, no. 22, pp. 260-266.
74. **Baykal Y., (2016)**, “*Fourth-order mutual coherence function in oceanic turbulence*”, Appl. Opt., vol. 55, pp. 2976-2979.
75. **Gökçe M. C., (2016)**, “*Beam shaping effects on MIMO free-space optical communication systems*”, Ph.D. dissertation, Çankaya University, Ankara, Turkey.
76. **Yi X., Li Z., Liu Z., (2015)**, “*Underwater optical communication performance for laser beam propagation through weak oceanic turbulence*”, Appl. Opt., vol. 54, pp. 1273-1278.
77. **Ata Y., Baykal Y., (2014)**, “*Scintillations of optical plane and spherical waves in underwater turbulence*”, J. Opt. Soc. Am. A, vol. 31, pp. 1552-1556.

78. **Li Y., Zhang Y., Zhu Y., (2019)**, “*Oceanic spectrum of unstable stratification turbulence with outer scale and scintillation index of Gaussian-beam wave*”, *Opt. Express*, vol. 27, pp. 7656-7672.
79. **Zou Z., et. al., (2019)**, “*Average capacity of a UWOC system with partially coherent Gaussian beams propagating in weak oceanic turbulence*”, *J. Opt. Soc. Am. A*, vol. 36, pp. 1462-1474.
80. **Baykal Y., (2015)**, “*Intensity fluctuations of multimode laser beams in underwater medium*”, *J. Opt. Soc. Am. A*, vol. 32, pp. 593-598.
81. **Baykal Y., (2016)**, “*Higher order mode laser beam scintillations in oceanic medium*”, *Wave Random Complex*, vol. 26, pp. 21-29.
82. **Baykal Y., (2017)**, “*Higher order mode laser beam intensity fluctuations in strong oceanic turbulence*”, *Opt. Commun.*, vol. 390, pp. 72-75.
83. **Baykal Y., (2016)**, “*Higher order laser beam scintillation in weakly turbulent marine atmospheric medium*”, *J. Opt. Soc. Am. A*, vol. 33, pp. 758-763.
84. **Baykal Y., (2016)**, “*Cross-beam scintillations in underwater medium*”, *Opt. Eng.*, vol. 55, 111612.
85. **Yousefi M., Golmohammady S., Mashal A., Kashani F. D., (2015)**, “*Analyzing the propagation behavior of scintillation index and bit error rate of partially coherent flat-topped laser beam in oceanic turbulence*”, *J. Opt. Soc. Am. A*, vol. 32, pp. 1982-1992.
86. **Yousefi M., Kashani F. D., Golmohammady S., Mashal A., (2017)**, “*Scintillation and bit error rate analysis of a phase-locked partially coherent flat-topped array laser beam in oceanic turbulence*”, *J. Opt. Soc. Am. A*, vol. 34, pp. 2126-2137.
87. **Gökçe M. C., Baykal Y., (2016)**, “*Scintillation analysis of multiple-input single output underwater optical links*”, *Appl. Opt.*, vol. 55, pp. 6130-6136.
88. **Baykal Y., (2016)**, “*Scintillations of LED sources in underwater medium*”, *Appl. Opt.*, vol. 55, pp. 8860-8863.
89. **Elamassie M., Uysal M., Baykal Y., Abdallah M., Qaraque K., (2017)**, “*Effect of eddy diffusivity ratio on underwater optical scintillation index*”, *J. Opt. Soc. Am. A*, vol. 34, pp. 1969-1973.
90. **Xu G., Lai J., (2020)**, “*Scintillation index and BER performance for optical wave propagation in anisotropic underwater turbulence under the effect of eddy diffusivity ratio*”, *Appl. Opt.*, vol. 59, pp. 2551-2558.

91. **Baykal Y., (2018)**, “*Effect of anisotropy on intensity fluctuations in oceanic turbulence*”, J. Mod. Opt., vol. 65, pp. 825-829.
92. **Cui Z., Yue P., Yi X., Li J., (2019)**, “*Scintillation of a partially coherent beam with pointing errors resulting from a slightly skewed underwater platform in oceanic turbulence*”, Appl. Opt., vol. 58, pp. 4443-4449.
93. **Luan X., Yue P., Yi X., (2019)**, “*Scintillation index of an optical wave propagating through moderate-to-strong oceanic turbulence*”, J. Opt. Soc. Am. A, vol. 36, pp. 2048-2059.
94. **Baykal Y., (2016)**, “*Scintillation index in strong oceanic turbulence*”, Opt. Commun., vol. 375, pp. 15–18.
95. **Baykal Y., (2020)**, “*Adaptive optics corrections of scintillations of Hermite-Gaussian modes in an oceanic medium*”, App. Optics, vol. 59, pp. 4826-4832.
96. **Chen D., et. al., (2019)**, “*Effect of air bubbles on underwater optical wireless communication*”, Chin. Opt. Let., vol. 17, 100008.
97. **Oubei H. M., et. al., (2018)**, “*Scintillations of RGB laser beams in weak temperature and salinity-induced oceanic turbulence*”, Fourth Underwater Communications and Networking Conference IEEE.
98. **Nelson C., Hyde M., Zamurovic S. A., (2019)**, “*Scintillation experiments with non-uniformly and uniformly correlated spatially partially coherent laser beams propagating underwater*”, J. Mod. Opt., vol. 66, pp. 1998-2007.
99. **Weng Y., Alkhazragi O., Guo J. H., (2019)**, “*Impact of Turbulent-Flow-Induced Scintillation on Deep Ocean Wireless Optical Communication*”, J. Lightwave Technol., vol. 37, pp. 5083-5090.
100. **Baykal Y., Eyyuboğlu H. T., Cai Y., (2010)**, “*Partially coherent off-axis Gaussian beam scintillations*”, J. Mod. Opt., vol. 57, pp. 1221-1227.
101. **Gerçekcioğlu H., Baykal Y., (2012)**, “*Intensity fluctuations of flat-topped beam in non-Kolmogorov weak turbulence*”, J. Opt. Soc. Am. A, vol. 29, pp. 169-173.
102. **Baykal Y., Plonus M. A., (1985)**, “*Intensity fluctuations due to a spatially partially coherent source in atmospheric turbulence as predicted by Rytov’s method*”, J. Opt. Soc. Am. A, vol. 2, pp. 2124-2132.
103. **Baykal Y., Eyyuboğlu H. T., (2005)**, “*Scintillation index of flat-topped Gaussian beams*”, J. Opt. Soc. Am. A, vol. 45, pp. 3793-3797.

104. **Baykal Y., Eyyuboğlu H. T., (2007),** “*Scintillations of incoherent flat-topped Gaussian source field in turbulence*”, Appl. Opt., vol. 46, pp. 5044-5050.
105. **Baykal Y., Eyyuboğlu H. T., Çil C. Z., Yangjian C., Korotkova O., (2011),** “*Intensity fluctuations of partially coherent cos Gaussian and cosh Gaussian beams in atmospheric turbulence*”, J. Opt., vol. 13, 055709.
106. **Gerçekcioglu H., Baykal Y., (2014)** “*Scintillation and BER for optimum sinusoidal Gaussian beams in weak non-Kolmogorov turbulence*”, Opt. Commun., vol. 320, pp. 1-5.
107. **Baykal Y., Eyyuboğlu H. T., Cai Y., (2010)** “*Scintillations in Weak Turbulence of Annular Beams Whose Individual Components are Incoherent*”, Prog. Electromagn. Res. Symposium Proceedings, Xi’an, China.
108. **Gökçe M. C., (2012),** “*Scintillation analysis and evaluation of Super Lorentz-Gaussian laser beams for optical wireless*”, MSc. Thesis, Ankara University, Ankara, Turkey.
109. **Baykal Y., Eyyuboğlu H. T., Cai Y., (2019),** “*Scintillations of partially coherent multiple Gaussian beams in turbulence*”, Appl. Opt., vol. 48, pp. 1943-1954.
110. **Eyyuboğlu H. T., Baykal Y., Cai Y., (2010),** “*Scintillation calculations for partially coherent general beams via extended Huygens-Fresnel integral and self-designed MATLAB function*”, Appl. Phys. B, vol. 100, pp. 597-609.
111. **Baykal Y., (2014),** “*Scintillations of higher-order laser beams in non-Kolmogorov medium*”, Opt. Lett., vol. 39, pp. 2160-2163.
112. **Wang S. J., Baykal Y., Plonus M. A., (1983),** “*Receiver-aperture averaging effects for the intensity fluctuation of a beam wave in the turbulent atmosphere*”, J. Opt. Soc. Am., vol 73, pp. 831-837.
113. **Lu L., Wang Z., Zhang P., Zhang J., Ji X., Fan C., (2017),** “*Beam wander of laser beam propagating through oceanic turbulence*”, Opt. Eng., vol. 56, 104107.
114. **Wu Y., Zhang Y., Li Y., Hu Z., (2016),** “*Beam wander of Gaussian-Schell model beams propagating through oceanic turbulence,*”, Opt. Commun., vol. 371, pp. 59-66.
115. **Yang Y., Yu L., Wang Q., Zhang Y., (2017),** “*Wander of the short-term spreading filter for partially coherent Gaussian beams through the anisotropic turbulent ocean*”, Appl. Opt., vol. 56, pp. 7046-7052.
116. **Jin Y., Hu M., Luo M., Luo Y., Mi X., Zou C., Zhou L., Shu C., Zhu X., He J., Ouyang S., Wen W., (2018),** “*Beam wander of a partially coherent*

Airy beam in oceanic turbulence”, J. Opt. Soc. Am. A, vol. 35, pp. 1457-1464.

117. **Niu C., Lu F., Han X., (2019)**, “*Approximate expression of beam wander of Gaussian array beams through oceanic turbulence*”, Optik, vol. 188, pp. 1-7.
118. **Wu Y., Zhang Y., Zhu Y., Hu Z., (2016)**, “*Spreading and wandering of Gaussian-Schell model laser beams in an anisotropic turbulent ocean*”, Laser Phys., vol. 26, no. 09001.
119. **Wu T., Ji X., Li X., Wang H., Deng Y., Ding Z., (2018)**, “*Characteristics parameters of optical wave and short-term beam spreading in oceanic turbulence*”, Acta Phys. Sin., vol. 67, 224206.
120. **Charnotskii M., (2015)**, “*Long and short-term beam spread by turbulence and optimization of the beam geometry*”, Oceans IEEE, Genova, ITALY.
121. **Cao P., (2019)**, “*Effect of anisotropy on the M^2 -factor and angular spreading of partially coherent Hermite-Gaussian beam propagating in anisotropic oceanic turbulence*”, Optik, vol. 178, pp. 1145-1153.
122. **Tang M., Zhao D., (2015)**, “*Regions of spreading of Gaussian array beams propagating through oceanic turbulence*”, Appl. Opt., vol 54, pp. 3407-6136.
123. **Liu D., Yin H., Wang G., Wang Y., (2017)**, “*Spreading of a Lorentz-Gauss Vortex Beam Propagating through Oceanic Turbulence*”, Curr. Opt. Photon., vol. 3, pp. 97-104.
124. **Fu W., Zheng X., (2019)**, “*Influence of anisotropic turbulence on the Second-order statistics of a general-type partially coherent beam in the ocean*”, Opt. Commun., vol. 438, pp. 46-53.
125. **Yura H. T., (1971)**, “*Atmospheric turbulence induced laser beam spread*”, Appl. Opt., vol. 10, pp. 2771-2773.
126. **Shirai T., Dogariu A., Wolf E., (2003)**, “*Mode analysis of spreading of partially coherent beams propagating through atmospheric turbulence*”, J. Opt. Soc. Am. A, vol. 20, pp. 1094-1102.
127. **Carter W. H., (1980)**, “*Spot size and divergence for Hermite Gaussian beams of any order*”, App. Opt., vol. 19, pp. 1027-1029.
128. **Gökçe M. C., Baykal Y., (2018)**, “*Aperture averaging and BER for Gaussian beam in underwater oceanic turbulence*”, Opt. Commun., vol. 410, pp. 830-835.
129. **Gerçekcioğlu H., (2014)**, “*Bit error rate of focused Gaussian beams in weak oceanic turbulence*”, J. Opt. Soc. Am. A, vol. 31, pp. 1963-1968.

130. **Ata Y., Baykal Y., (2018)**, “*Effect of anisotropy on bit-error-rate for an asymmetrical Gaussian beam in a turbulent ocean*”, Appl. Opt., vol. 57, pp. 2258-2262.
131. **Baykal Y., (2017)**, “*BER of asymmetrical optical beams in oceanic and marine atmospheric media*”, Opt. Commun., vol. 393, pp. 29-33.
132. **Arpali S. A., Baykal Y., Arpali Ç., (2016)**, “*BER evaluations for multimode beams in underwater turbulence*”, J. Mod. Opt., vol. 63, pp. 1297-1300.
133. **Baykal Y., (2018)**, “*Bit error rate of pulse position modulated optical wireless communication links in oceanic turbulence*”, J. Opt. Soc. Am. A, vol. 35, pp. 1627-1632.
134. **Gökçe M. C., Baykal Y., Ata Y., (2018)**, “*Performance analysis of M-ary pulse position modulation in strong oceanic turbulence*”, Opt. Commun., vol. 427, pp. 573-577.
135. **Baykal Y., Gökçe M. C., Ata Y., (2020)**, “*Application of adaptive optics on bit error rate of M-ary pulse-position-modulated oceanic optical wireless communication systems*”, Laser Phys., vol. 30, 076202.
136. **Baykal Y., (2019)**, “*Anisotropy effect on performance of PPM optical wireless oceanic communication links*”, J. Quant. Spectrosc. Ra., vol. 228, pp. 73-78.
137. **Jurado N. A., et. al., (2018)**, “*Error probability analysis of OOK and variable weight MPPM coding schemes for underwater optical communication systems affected by salinity turbulence*”, OSA Continuum, vol. 1, pp. 1131-1143.
138. **Gökçe M. C., Baykal Y., Ata Y., (2019)**, “*Binary phase shift keying-subcarrier intensity modulation performance in weak oceanic turbulence*”, Phys. Commun., vol. 37, 100904.
139. **Baykal Y., Gökçe M. C., Ata Y., (2019)**, “*Anisotropy effect of performance of subcarrier intensity modulated binary phase shift keying optical wireless communication links in weak turbulent underwater channel*”, J. Mod. Opt., vol. 66, pp. 1871-1875.
140. **Gökçe M. C., Baykal Y., Ata Y., (2020)**, “*Effect of anisotropy on performance of M-ary phase shift keying subcarrier intensity-modulated optical wireless communication links operating in strong oceanic turbulence*”, Laser Phys. Lett., vol. 17, 056002.
141. **Gökçe M. C., Baykal Y., Ata Y., (2020)**, “*M-ary phase shift keying-subcarrier intensity modulation performance in strong oceanic turbulence*”, Opt. Eng., vol. 58, 056105.

142. **He F. T., et. al., (2019)**, “*Bit error rate of pulse position modulation wireless optical communication in gamma-gamma oceanic anisotropic turbulence*”, *Acta Phys. Sin.*, vol. 68, 164206.
143. **Jiang H. Y., et. al., (2020)**, “*Performance of Spatial Diversity DCO-OFDM in a Weak Turbulence Underwater Visible Light Communication Channel*”, *J. Lightwave Technol.*, vol. 38, pp. 2271-2277.
144. **Chen W., et. al., (2020)**, “*Impact of temperature gradients on average bit error rate performance of low-density parity-check-coded multihop underwater wireless optical communication systems over the generalized gamma distribution*”, *Opt. Eng.*, vol. 59, 016114.
145. **Fu Y., Huang C., Du Y., (2019)**, “*Effect of aperture averaging on mean bit error rate for UWOC system over moderate to strong oceanic turbulence*”, *Opt. Commun.*, vol. 451, pp. 6-12.
146. **Pang W., et. al., (2019)**, “*Performance investigation of UWOC system with multiuser diversity scheduling schemes in oceanic turbulence channels*”, *Opt. Commun.*, vol. 441, pp. 138-148.
147. **Peppas K., Boucouvalas A., Ghassemloy Z., (2017)**, “*Performance of underwater optical wireless communication with multi-pulse pulse-position modulation receivers and spatial diversity*”, *IET Optoelectron.*, vol. 11, pp. 180-185.
148. **Wu T., et. al., (2019)**, “*Rytov variance of spherical wave and performance indicators of laser radar systems in oceanic turbulence*”, *Opt. Commun.*, vol. 434, pp. 36-43.
149. **Yin X., et. al., (2018)**, “*Performance of Oceanic Wireless Optical Communication Systems Based on Orbital Angular Momentum Multiplexing with Spatial Diversity*”, *Acta Photon. Sin.*, vol. 47, 1106003.
150. **Arpali S., Baykal Y., Arpali C., (2016)**, “*BER for Higher Order Laser Modes in Optical Wireless Underwater Communications*”, *IEEE 22nd International Conference on Applied Electromagnetics and Communications (ICECOM)*.
151. **Charnotskii M., (2015)**, “*Bit error rate of focused Gaussian beams in weak oceanic turbulence: comment*”, *J. Opt. Soc. Am. A*, vol. 32, pp. 1247-1250.
152. **Arpali S. A., Baykal Y., (2009)**, “*Bit Error Rates for Focused General-type Beams*”, *PIERS Online*, vol. 5, pp. 633-636.
153. **Arpali S. A., Eyyuboğlu H. T., Baykal Y., (2008)**, “*Bit Error Rates for General Beams*”, *Appl. Opt.*, vol. 47, pp. 5971-5975.

154. **Baykal Y., (2016)**, “*Expressing oceanic turbulence parameters by atmospheric turbulence structure constant*”, *Appl. Opt.*, vol. 55, pp. 1228-1231.
155. **Baykal Y., Ata Y., Gökçe M. C., (2019)**, “*Structure parameter of anisotropic atmospheric turbulence expressed in terms of anisotropic factors and oceanic turbulence parameters*”, *Appl. Opt.*, vol. 58, pp. 454-460.
156. **Ata Y., Baykal Y., (2014)**, “*Structure functions for optical wave propagation in underwater medium*”, *Wave Random Complex*, vol. 24, pp. 164-173.
157. **Ata Y., Baykal Y., (2014)**, “*Field correlation of spherical wave in underwater turbulent medium*”, *Appl. Opt.*, vol. 53, pp. 7968-7971.
158. **Baykal Y., (2020)**, “*Intensity correlations of flat-topped beams in oceanic turbulence*”, *J. Mod. Opt.*, vol. 67, pp. 799-804.
159. **Huang X., Bai Y., Fu X., (2017)**, “*Propagation Factors of Partially Coherent Model Beams in Oceanic Turbulence*”, *IEEE Photonics J.*, vol. 9, 6101911.
160. **Yue P., Xu D. L., Yi X., (2019)**, “*Propagation of the Bessel-Gaussian beams generated by coherent beam combining in oceanic turbulence*”, *J. Comm. Inf. Netw.*, vol. 4(3), 25-37.
161. **Sun C., Lv X., Ma B., Zhang J., Deng D., Hong W., (2019)**, “*Statistical properties of partially coherent radially and azimuthally polarized rotating elliptical Gaussian beams in oceanic turbulence with anisotropy*”, *Opt. Express*, vol. 27, no. 28, pp. A245-A256.
162. **Zhou Y., Zhao D., (2018)**, “*Propagation properties of a twisted rectangular multi-Gaussian Schell-model beam in free space and oceanic turbulence*”, *Appl. Opt.*, vol. 57, pp. 8978-8983.
163. **Yousefi M., Kashani F., Golmohammady S., Kazemian E., Ghafary B., (2014)**, “*Analysing the behaviour of partially coherent divergent Gaussian beams propagating through oceanic turbulence*”, *J. Mod. Opt.*, vol. 61, pp. 1430-1441.
164. **Tang M., Zhao D., (2013)**, “*Propagation of radially polarized beams in the oceanic turbulence*”, *Appl. Phys. B*, vol. 111, pp. 665-670.
165. **Ye F., et. al., (2019)**, “*Propagation properties of a controllable rotating elliptical Gaussian optical coherence lattice in oceanic turbulence*”, *Res. Phys.*, vol. 13, 102249.

166. **Liu D., Wang Y., Yin H., (2015)**, “*Evolution properties of partially coherent flat-topped vortex hollow beam in oceanic turbulence*”, *App. Opt.*, vol. 54, pp. 10510-10516.
167. **Kashani F. D., Yousefi M., (2016)**, “*Analyzing the propagation behavior of coherence and polarization degrees of a phase-locked partially coherent radial flat-topped array laser beam in underwater turbulence*”, *App. Opt.*, vol. 55, pp. 6311-6320.
168. **Zhang H., Fu W., (2014)**, “*Changes in polarization properties of partially polarized, partially coherent vectorial cosh-Gaussian beams propagating in oceanic turbulence*”, *Wave Random Complex*, vol. 24, pp. 376-392.
169. **Cheng M., Guo L., Li J., Huang Q., Cheng Q., Zhnag D., (2016)**, “*Propagation of an optical vortex carried by a partially coherent Laguerre-Gaussian beam in turbulent ocean*”, *Appl. Opt.*, vol. 55, pp. 4642-4648.
170. **Liu D., Wang G., Yin H., Wang Y., (2017)**, “*Propagation of partially coherent Lorentz-Gauss vortex beam through oceanic turbulence*”, *Appl. Opt.*, vol. 56, pp. 8785-8792.
171. **Ding C., Liao L., Wang H., Zhang Y., Pan L., (2015)**, “*Effect of oceanic turbulence on the propagation of cosine-Gaussian-correlated Schell-model beams*”, *J. Opt.*, vol. 17, 035615.
172. **Zheng X., Fu W., (2020)**, “*Effect of anisotropy on the radius of curvature and Rayleigh range of a general-type partially coherent beam in oceanic turbulence*”, *Second Target Recognition Artificial Intelligence Summit Forum*, vol. 11427, 114271P.
173. **Liu D., Wang Y., (2016)**, “*Evolution properties of a radial phased-locked partially coherent Lorentz-Gauss array beam in oceanic turbulence*”, *Opt. Laser Technol.*, vol. 103, pp. 33-41.
174. **Liu D. J., et. al., (2019)**, “*Properties of multi-Gaussian Schell-model beams carrying an edge dislocation propagating in oceanic turbulence*”, *Chinese Phys. B*, vol. 28, 104207.
175. **Liu Y., et. al., (2020)**, “*Statistical Characteristics of a Twisted Anisotropic Gaussian Schell-Model Beam in Turbulent Ocean*”, *Photonics*, vol. 7, no. 37.
176. **Lu L., Ji X., Baykal Y., (2014)**, “*Wave structure function and spatial coherence radius of plane and spherical waves propagating through oceanic turbulence*”, *Opt. Express*, vol. 22, pp. 27112-27122.
177. **Gökçe M. C., Baykal Y., (2018)**, “*Aperture averaging in strong oceanic turbulence*”, *Opt. Commun.*, vol. 413, pp. 196-199.

178. **Wang Z., Lu L., Zhang P., Fan C., Ji X., (2016)**, “*Broadening of ultra-short pulses propagating through weak-to-strong oceanic turbulence*”, *Opt. Commun.*, vol. 367, pp. 95-101.
179. **Golmohammady S., Gafary B., (2016)**, “*Generalized Stokes parameters and polarization behavior of flat-topped array laser beam propagating through oceanic turbulence*”, *Waves Random Complex*, vol. 27, pp. 403-419.
180. **Shchepakina E., Farwell N., Korotkova O., (2011)**, “*Spectral changes in stochastic light beams propagating in turbulent ocean*”, *Appl. Phys. B.*, vol. 105, pp. 415-420.
181. **Zamurovic S. A., Nelson C., (2018)**, “*Experimental study: underwater propagation of polarized flat top partially coherent laser beams with a varying degree of spatial coherence*”, *Opt. Commun.*, vol. 424, pp. 54-62.
182. **Zhou Y., Huang K., Zhao D., (2012)**, “*Changes in statistical properties of stochastic anisotropic electromagnetic beams propagating through the oceanic turbulence*”, *App. Phys. B*, vol. 109, pp. 289-294.
183. **Lu L., et. al., (2014)**, “*Influence of oceanic turbulence on propagation characteristics of Gaussian array beams*”, *Optik*, vol. 125, pp. 7154-7161.
184. **Baykal Y., (2018)**, “*Signal-to-noise ratio reduction due to oceanic turbulence in oceanic wireless optical communication links*”, *Opt. Commun.*, vol. 427, pp. 44-47.
185. **Baykal Y., (2019)**, “*SNR advantage of anisotropy in oceanic optical wireless communications links*”, *J. Opt. Soc. Am. A.*, vol. 36, pp. 1991-1996.
186. **Wang M., et. al., (2018)**, “*Propagation of laser beams through air-sea turbulence channels*”, *Laser Communication and Propagation Through The Atmosphere and Oceans VII*, vol. 10770, UNSP 1077003.
187. **Gökçe M. C., (2019)**, “*Average capacity analysis of underwater optical wireless communication links over anisotropic strong oceanic turbulence channels*”, *J. Opt. Soc. Am. A.*, vol. 36, pp. 2040-2047.
188. **Aliyu M., et. al., (2018)**, “*Characteristics of bubble-induced liquid flows in a rectangular tank*”, *Exp. Therm. Fluid. Sci.*, vol. 97, pp. 21-35.
189. **Han B., et. al., (2019)**, “*Experimental demonstration of quasi-omni-directional transmitter for underwater wireless optical communication based on blue LED array and freeform lens*”, *Opt. Commun.*, vol. 434, pp. 184-190.
190. **Li J., et. al., (2020)**, “*Centroid drift of laser beam propagation through a water surface with wave turbulence*”, *App. Opt.*, vol. 59, pp. 6210-6217.

191. **Keskin A., Baykal Y., (2020)**, “*Off-axis transmittance of partially coherent cos&cosh-Gaussian beams in underwater turbulence medium*”, (accepted as a poster presentation) SIU 2020 28th IEEE Conf. Sign. Process. And Comm. Appl., Turkey.
192. **Eyyuboğlu H. T., Baykal Y., Cai Y., (2007)**, “*Complex degree of coherence for partially coherent beams*”, J. Opt. Soc. Am. A, vol. 24, pp. 2891-2901.
193. **Wang S. C. H., Plonus M. A., (1979)**, “*Optical beam propagation for a partially coherent source in the turbulent atmosphere*”, J. Opt. Soc. Am., vol. 69, pp. 1297-1304.
194. **Alevinajad M., Ghafary B., (2018)**, “*Turbulence-induced degradation properties of partially coherent flat-topped beams*”, Opt. Lasers Eng., vol. 46, pp. 357-362.
195. **Oubei H. M., Zedini E., Elafandy R. T., Kammoun A., Abdallah M., Ng T. K., Hamdi Mounir, Alouini M. S., Ooi B. S., (2017)**, “*Simple statistical channel model for weak temperature-induced turbulence in underwater wireless optical communication systems*”, Opt. Lett., vol. 42, pp. 2455-2458.
196. **Zamurovic S. A., Nelson C., Hyde M., (2019)**, “*Experimental study: underwater propagation of super-Gaussian and multi-Gaussian Schell-model partially coherent beams with varying degrees of spatial coherence*”, OSA Continuum, vol. 2, pp. 450-459.
197. **Thorpe S. A., (2007)**, “*An Introduction to Ocean Turbulence*”, Cambridge University Press, Cambridge.
198. **Thorpe S. A., (2005)** “*The Turbulent Ocean*”, Cambridge University Press, Cambridge.
199. **Lu W., Liu L., Sun J., (2006)**, “*Influence of temperature and salinity fluctuations on propagation behaviour of partially coherent beams in oceanic turbulence*”, J. Opt. A, vol. 8, pp. 1052-1058.
200. **Saleh B. E. A., Teich M. C., (2007)**, “*Fundamentals of Photonics*”, John Willey, Sons, Inc, Hoboken, New Jersey, Canada.
201. **Andrews L. C., Phillips R. L., (2005)**, “*Laser beam propagation through random media*”, SPIE, Washington.
202. **Andrews L. C., (2004)**, “*Field guide to atmospheric optics*”, SPIE.
203. **Baykal Y., (2006)**, “*Formulation of correlations for general-type beams in atmospheric turbulence*”, J. Opt. Soc. Am. A, vol. 23, pp. 889-893.

204. **Gradshteyn I. S., Ryzhik M. I., (2007)**, “*Table of Integrals, Series, and Products*”, Academic.
205. **Gökçe M. C., Baykal Y., Uysal M., (2016)**, “*Aperture averaging in multiple input single-output free space optical systems using partially coherent radial array beams*”, J. Opt. Soc. Am. A, vol. 33, pp. 1041-1048.
206. **Gökçe M. C., Baykal Y., Uysal M., (2016)**, “*Performance analysis of multiple-input multiple-output free-space optical systems with partially coherent Gaussian beams and finite-sized detectors*”, Opt. Eng., vol. 55, 111607.
207. **Keskin A, Baykal Y. (2018)**, “*On-axis transmittance for partially coherent flat-topped beams in underwater turbulence*”, 1st International Eurasian Conf. on Sci. Eng. and Tech., Ankara, Turkey.
208. **Gökçe M. C., Baykal Y., (2018)**, “*Effects of liver tissue turbulence on propagation of annular beam*”, Optik, vol. 171, pp. 313-318.

APPENDICES

APPENDIX A

CURRICULUM VITAE

PERSONAL INFORMATION

Surname, Name: Keskin, Aysan

Date and Place of Birth: 4 February 1986, Ankara

Phone: +90 532 157 41 48

Email: aysankeskin@gmail.com

EDUCATION

Degree	Institution	Year of Graduation
M.Sc.	Çankaya Univ., Electronic and Communication Engineering	2013
B.Sc.	Çankaya Univ., Electronic and Communication Engineering	2010

FOREIGN LANGUAGES

Advanced English, Beginner Spanish

PUBLICATIONS (produced from the thesis study)

1. Keskin A., Baykal Y., (2019), “*Off-axis average transmittance and beam spread of a partially coherent flat-topped beam in a turbulent underwater medium*”, J. Opt. Soc. Am. A., vol. 36, pp. 1287-1294.
2. Keskin A., Baykal Y., (2020), “*Effects of underwater turbulence on average transmittance of cos-Gaussian and cosh-Gaussian optical beams*”, Waves in Random and Complex Media, doi. 10.1080/17455030.2020.1743894.

CONFERENCES (produced from the thesis study)

1. Keskin A., Baykal Y., Ata Y., (2014), “*Optical transmittance in turbulent underwater medium*”, Proc. Çankaya Univ., Eng. Tech. Symp., vol. 7, pp. 137-141.
2. Keskin A., Catmakas O. K., Genc F., Baykal Y., Arpali S. A., Arpali C., (2015), “*Effects of Focused and Collimated Laser Beams on the Performance of Underwater Wireless Optical Communications*”, International Workshop on Optical Wireless Communications, Istanbul, Turkey, pp. 41-45.
3. Keskin A, Baykal Y. (2018), “*On-axis transmittance for partially coherent flat-topped beams in underwater turbulence*”, 1st International Eurasian Conf. on Sci. Eng. and Tech., Ankara, Turkey.
4. Keskin A., Baykal Y., (2020), “*Off-axis transmittance of partially coherent cos&cosh-Gaussian beams in underwater turbulence medium*”, (accepted as a poster presentation) SIU 2020 28th IEEE Conf. Sign. Process. and Comm. Appl., Turkey.

